Computational Studies of Penetration and Mixing for Complex Jet Injectors to Aid in Design of Hypersonic Systems

Theresa Lynn Campioli

Dissertation submitted to the faculty of the Virginia Polytechnic Institute and State University in partial fulfillment of the requirements for the degree of

Doctor of Philosophy
In
Aerospace & Ocean Engineering Department

Dr. Joseph Schetz, Chair

Dr. Robert Walters

Dr. Richard Barnwell

Dr. William Devenport

Dr. John Sparks

Dr. Fred Billig

June 21, 2007
Blacksburg, VA

Keywords: Scramjet, CFD, numerical modeling, injection, shock-jet interaction, mixing, combustion

Computational Studies of Penetration and Mixing for Complex Jet Injectors to Aid in Design of Hypersonic Systems

Theresa Lynn Campioli

ABSTRACT

A computational study of sonic light-gas jet injection into a supersonic cross flow was conducted. The scope of the numerical analysis encompassed many studies that affect how the flow-field is numerically modeled and the behavior, specifically mixing, of the flow-field itself. A single, round injector was used for the Baseline design. Simulated conditions involved sonic injection of helium heated to 313 K into a Mach 4 air cross-stream with average Reynolds number 5.77 e+7 per meter and a freestream momentum flux ratio of 2.1. Experiments at these conditions were available for comparison. The primary numerical flow solver employed was GASP v. 4.2. The Menter Shear Stress Transport (SST) turbulence model was used, since the algorithm has good capability of solving both wall-bounded and free-shear flows. The SST model was able to capture the mixing behavior of the complex flow-field. Important numerical parameters that affect the capabilities of the numerical solver were studied for the Baseline injector. These sensitivity studies varied the choice of turbulent Prandtl number, Schmidt number, freestream turbulence intensity, boundary layer size, steady and unsteady approaches and computational software packages. A decrease in the turbulent Prandtl number resulted in better mixing behavior of the prediction and better agreement with the experiment. An increase in the turbulent Schmidt number had a small adverse effect on the predictions. The mixing characteristics remained constant with an increase in freestream turbulence intensity. The best Baseline prediction was then compared to three different injector configurations: an aerodynamic ramp consisting of four injectors in an array, a diamond injector both aligned and yawed 15º to the oncoming flow. The Computational Fluid Dynamics (CFD) tools were more accurate compared to experiment in the prediction of the aeroramp injector than the diamond-shaped injectors. The aeroramp injector slightly improved mixing efficiency over the Baseline injector at these conditions. Both of the diamond-shaped injectors had similar mixing as the Baseline injector but did not predict significant improvement in penetration for the analyzed conditions. Additional studies involving the interaction of transverse injection with impinging oblique shock waves were performed. The impingement of a shock upon light gas jet injection increased mixing. The closer the shock is to the injection point, the larger the effect on mixing and vorticity. The last analyses involved a numerical comparison of a non-reacting model to a reacting hydrogen-air model. The reacting analysis prediction had an improved spreading rate and larger counter-rotating vortex pair with downstream distance over the non-reacting analysis. The mixing was not significantly altered by the addition of hydrogen-air reactions to the numerical equations. The numerical tools used are capable of reasonable accuracy in predicting the complex flow-field of jet injection into a supersonic freestream with proper choice of models and parameters. Numerical modeling offers a way to study the entire flow-field thoroughly in a cost and time efficient manner.

Acknowledgements

The past several years of research and writing was made possible by the personal and practical support from numerous people who I cannot thank enough. I would like to first and foremost thank my advisor, Dr. Joseph Schetz. Not only did you give me the opportunity to achieve advance degrees, expand my knowledge and travel to other countries to present our work, your daily support, knowledge and encouragement was vital to the completion of this research. Over the past four years, you have taught me much about aerospace engineering, but also about life and being an engineer.

I would like also to thank my committee, Dr. Walters, Dr. Devenport, Dr Barnwell, Dr. Sparks, and the late Dr. Billig for playing active roles in my research development and for always being available for advice and questions.

Much deserved thanks goes to my research partner, Luca Maddalena. You are a great person to work with and great friend. I'm glad to have been able to share research efforts and time with you. I wish you the best of luck with your research, in your career and any future endeavors. I would also like to thank the research group at Virginia Tech that I was a part of. You always made the days more enjoyable.

I would like to thank Aerojet for all of the help along the way both academically and financially which made my research efforts possible. A special thanks to Mark Friedlander for helping me to prioritize and giving me encouragement and direction when I needed it most. Thanks to everyone at Aerojet especially, Dave Polen and Kent Hennessey, who has contributed to my growth, knowledge and to this research.

On a personal note, I would like to thank my family for everything you have done for me, without you I would not have made it this far. Dad, Mom, Mary, Jenn and Jason, thank you for always being there for me. You have inspired me to work hard and to enjoy and appreciate each and every day. Your love, encouragement, advice and support have been large part of my success. You have kept me balanced. I am truly blessed to have such an incredible and loving family, you make it all worth while. I would like also to thank my new family, Shaf, Angela and Jenn for all of your help and encouragement along the way.

I would like to thank Cathy Sybert for all of your support and the many long hours spent listening to me. Your friendship has been very important to me and it has help me to grow as a person. I am so lucky to have you as a friend and inspiration.

I would lastly like to thank, Dan Shafer, my soon-to-be husband. You have been so wonderful and supportive. Thanks for being there for me through it all, the good and the bad. Thanks for staying positive and giving me perspective. Thanks for keeping me grounded and always giving me something to laugh about, even if it was about me. This would not have been possible without your love and encouragement. I am so lucky to have such an amazing person in my life. I love you and thank you.

Table of Contents

List of Figures

List of Tables

Nomenclature

A_j	=	injector area	[m^2]
C_d	=	discharge coefficient	
C_v	=	specific heat	[J kg/K]
d	=	jet diameter	[mm]
d_{eq}	=	equivalent jet diameter	[mm]
d_{eff}	=	effective diameter	[mm]
D	=	diffusion coefficient	
E	=	total internal energy, activation energy	
f	=	stoichiometric hydrogen-air ratio	
h	=	enthalpy	
K	=	turbulent kinetic energy (or TKE)	[m^2/s^2]
K	=	equilibrium constant, source Jacobian	
k_b	=	backward reaction rate constant	
k_f	=	forward reaction rate constant	
l_t	=	turbulent length scale	
M	=	Mach number	
M	=	molecular weight	
Ns	=	number of species	
p_c	=	cone-static pressure	
p_t	=	total pressure	
$p_{t,Pitot}$	=	Pitot pressure	[Pa or PSI]
P	=	static Pressure	[Pa or PSI]
P_t	=	total Pressure	[Pa or PSI]
P_{t2}	=	Pitot Pressure	
P_{rt}	=	turbulent Prandtl number	
$\bar{q}$	=	jet-to-free-stream momentum flux ratio	
R	=	gas constant	
R	=	resistance	
Re	=	Reynolds number	
S_{ct}	=	turbulent Schmidt number	
t	=	time	
T	=	temperature	[K]
T_t	=	total temperature	[K]
TI	=	turbulence intensity	
u	=	free stream velocity	[m/s]
V	=	voltage	
$\dot{w}$	=	species production rate	
X	=	mole fraciton	
x	=	axial distance downstream of injector center	[m]
y	=	lateral distance from the injector centerline	[m]
z	=	vertical distance from the wall	[m]
$y^{\pm}$	=	plume width	[m]
z_{max}	=	maximum plume penetration	[m]
z^+	=	vertical location of plume center of mass	[m]

α = mass fraction
γ = ratio of specific heats
σ = stoichiometric coefficient
σ = mass concentration
ε = turbulence dissipation rate $[m^2/s^2]$
δ = Kronecker delta
η_m = mixing efficiency
μ = laminar (molecular) viscosity $[Ns/m^2]$
μ_T = turbulent (eddy) viscosity $[Ns/m^2]$
ν = kinematic viscosity $[m^2/s]$
ν_T = turbulent viscosity $[m^2/s]$
ρ = density $[kg/m^3]$
τ = shear stress $[N/m^2]$
ω = turbulent frequency $[m^3/s^3]$
ω = vorticity
$\omega_{in\text{-}plane}$ = in-plane vorticity
Ω = mean vorticity
Π = total pressure loss parameter
Θ = characteristic temperature of vibration

Subscripts

j = jet-exit property
n = normal component
rot = rotational equilibrium
s = system
trans = translation equilibrium
t = thermal
t = total condition
t = tangential component when used with ω
vib = vibrational equilibrium
w = hot film
x = streamwise component
y = cross-stream component
z = vertical component
∞ = freestream property

Superscripts

- = Time-averaged values
$\rightarrow$ = vector

Acronyms

CVP = Counter-rotating vortex pair

CFD = Computational Fluid Dynamics

Chapter 1: Introduction

1.1. Background

A supersonic combustion ramjet, commonly referred to as a scramjet, is an air-breathing engine where the flow of air and the combustion of the fuel-air mixture through the engine occur at supersonic speeds. Supersonic combustion can allow the vehicle to fly efficiently at hypersonic speeds ranging from Mach 5 to excess of Mach 12. Scramjets are simple in the sense that they do not contain large moving parts like turbines or fans. Figure 1.1 is a representative schematic of a scramjet engine. The vehicle operates by using the geometric design of the vehicle and inlet (diffuser) to compress air as it passes over the body. Then, within the combustion chamber, the injected fuel is mixed and combusted into the supersonic air stream, and lastly the fuel-air mixture is expanded through the nozzle. Even with this relatively uncomplicated ideology of a design, there are many areas of interest for technological improvements needed for scramjet engines. A few of the areas of technological improvements that will lead to future successes are material improvements, a better understanding of the behavior of supersonic combustion flames, the chemical reaction processes of fuels such as hydrogen or hydrocarbons with air, the fuel-air mixing process and suitable numerical modeling of these areas. The last two areas are the focus of the present research.

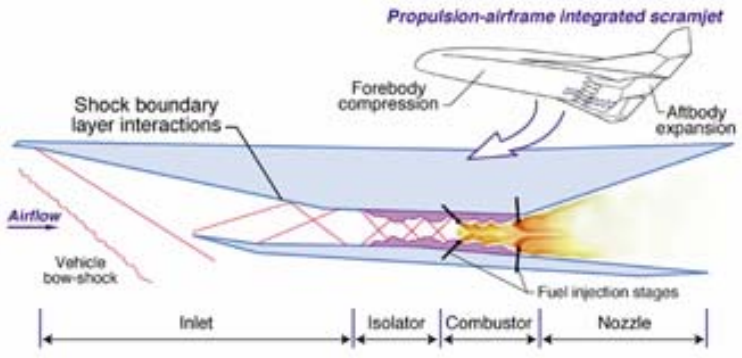

Figure 1.1 Schematic of Scramjet engine[9]

A brief discussion of past scramjet work is presented to give background and purpose to the current work. Scramjet engine research has been on-going internationally

since the 1960's. The leading contributor to the development of hydrogen fueled scramjet engines in the United States was Antonio Ferri. Some of his works are reviewed in Ref 1 and Ref 2. He studied areas such as fuel-air chemistry, turbulent mixing, thermal compression and 3-D engine designs to help maximizing engine performance throughout a broad flight envelope. In the mid to late 1960's, The U.S Air Force, U.S. Navy and NASA funded several scramjet research, ground tests and flight tests programs; however, most of the programs were cancelled before any testing occurred. One NASA program that did complete some ground testing was the Hypersonic Research Engine(HRE) which tested the Aerothermodynamic Integration Model (AIM)[3]. The ground testing at NASA Glenn Research Center demonstrated high internal thrust performance, dual mode combustion, fuel autoignition and torch ignition. In the 1970's the U.S. Navy funded Johns Hopkins University Applied Physics Laboratory (APL) for the Supersonic Ramjet Missile Program (SCRAM)[4]. The program designed and tested an air-breathing weapon system with 3-D Busemann inlets and hydrocarbon fuels. An extensive database of combustor geometries, injection techniques and reactive fuels were studied. In the 1980's, DARPA sponsored the National Aerospace Plane (NASP)[5] program, which produced many advancements in hypersonic technologies and test facilities including high-fidelity databases and CFD methods to name a few. The goal of NASP was to create two X-30 single-stage-to-orbit (SSTO) hydrogen fueled scramjets that could accelerate a vehicle to Mach 3. Unfortunately, the program was cancelled before a vehicle was flown. The NASP program did, however, generate a multitude of research that has been useful in modern day scramjet successes. The current successful flights of scramjet engines have been short duration and limited flights. The typical flight tests of successful scramjet engines begin with launch from a booster rocket to accelerate the vehicle to the necessary Mach number. Upon release from the rocket, the air-breathing engine takes over and powers the vehicle. The first flight test of a hypersonic vehicle at Mach 5.35 was conducted in Russia in late 1991. The vehicle operated as a dual-mode scramjet engine demonstrating both subsonic and supersonic combustion. A joint venture between Russia and France produced three more flight tests. The second held in 1995 reportedly achieved supersonic combustion conditions at Mach 5.6 and the third test failed[6]. The first verified demonstration of scramjet flight occurred on July 30, 2002. The Australian program,

HyShot, was engineered by the University of Queensland[7]. Hyshot flew at Mach 7.6 for 6 seconds. The flight tests achieved supersonic combustion data at a single Mach number for a range of dynamic pressures. NASA's X-43A (Hyper-X program)[8] maintained flight at Mach 7 for 10 seconds in March of 2004 and at Mach 10 for 11 seconds in November of 2004. Both flights were launched from a B-52 and used a booster rocket to accelerate the vehicle to the necessary take-over Mach number. The trajectory of the flight can be seen in Figure 1.2. Figure 1.3 shows a schematic of the X-43A vehicle. Both these flights are short duration, but they prove that hypersonic air-breathing flight is achievable and also that continuous progress and advancement is necessary.

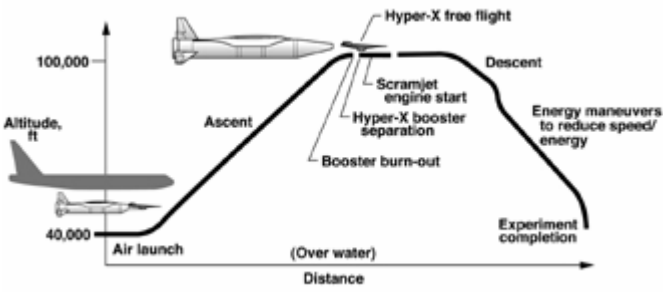

Figure 1.2 Hyper-X first flight Trajectory[9]

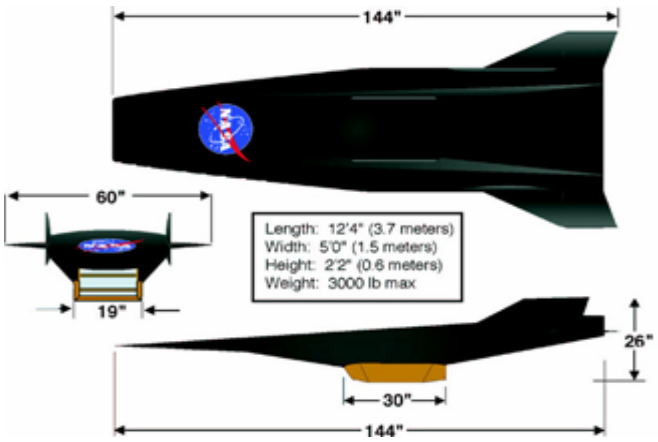

Figure 1.3 NASA's Hyper-X, X-43A Scramjet Engine[9]

To improve upon these short duration flights towards the goal of sustained hypersonic flight, combustion with efficient mixing capabilities is essential. Anderson[10] defined mixing as an empirical, one-dimensional measure of the degree of mixing completeness that accounted for both near-field and far-field mixing while accounting for stoichiometry. Efficient mixing is directly related to the behavior of the combustion

process, so better mixing leads to more efficient combustion. A few important concepts involved in fuel-air mixing are fuel penetration, fuel residence times, turbulent mixing of the fuel and air and distance to complete mixing. A successful design for a scramjet engine will depend upon enhancing the fuel-air mixing in supersonic flows. For this reason the fuel delivery system, specifically, jets in a high-speed cross-flow has been a topic of scientific interest for scramjet technologies and continues to be a significant topic for scramjets and other areas such as jet interaction for controls.

There are several ways to introduce fuel into the supersonic cross stream in a scramjet engine. Fuel can be injected into the combustion chamber by means of ramp, cantilever, and transverse jets. Ramp injectors[11,12,13,14,15,16] with parallel injection have lower total pressure losses than normal injection but poor penetration into the cross stream. The loss of mixing capabilities for the physical ramp can be attributed to the protrusion of the ramp into the flow which causes momentum losses and consequently loss in thrust and performance. In addition, the fuel now requires a longer time and distance to mix with the supersonic freestream air because of the reduction in shear layer growth from reduced turbulent mixing. The reduced turbulent mixing leads to reductions in molecular mixing of the two species and delays the rate of combustion energy release. A longer distance to mix correlates to a heavier vehicle, which is not desired. Sunami[17] showed through experiments that improvements in mixing distance for parallel injection can be accomplish through the use of an alternating wedge strut. The generation of streamwise vortices from the strut enhanced mixing. Parent[12] studied the same strut numerically using the Wilcox model with a dissipation correction. The mixing capabilities of the ramp and the physics of the flow were accurately modeled.

To improve upon the penetration of the fuel by ramp injectors, normal injection has been used. Normal injection has been shown to have good penetration and can reduce the required mixing distance, but is accompanied by shocks created from injection. The shocks can reduce the total pressure which can reduce engine efficiency. Transverse, or normal, injection have been studied for the past 40 years by Billig[18], Heiser[15], Tomioka[19], Schetz[20], Fuller[21], Barber[22], Murugappan[23], Beresh[24] and Rogers[25] to name a few. A relatively recent review can be found in Schetz and Billig[26]. The supersonic cross flow is displaced by the fuel jet and the accompanying shocks. The flush wall injectors produce a

flow-field similar to that of flow around a bluff body. The flow-field will be described in detail later in this chapter. The separation regions and turbulent flow aid in the mixing of the fuel and air. Mixing produced by normal injection occurs more quickly than parallel injection and reduces mixing distance which is critical to making scramjets light and efficient. Curran[27] found that "the overall effect of the normal jet on the flow-field is to anchor the mixing layer firmly to the jet core, reducing the mixing distance to not only zero, but actually to a small negative distance." Hollo et al[28] studied mixing and found that through normal injection in a Mach 2 cross flow, it took approximately 20 diameters to transition from near-field to far-field mixing. The gains of transverse injection are produced by the near-field mixing which is dominated by the stirring or macromixing of the jet-freestream interaction. The far-field mixing is dominated by the molecular mixing from the fuel-air shear layer. The tradeoff of enhanced mixing is the total pressure losses associated with separation and flow across strong shocks formed from the jet injection. One way to reduce the severity of shock losses from normal jet injection, while still maintaining good near-field mixing is through downstream angled fuel injection. This will give the fuel a component of velocity in the downstream direction and weakens the bow shock caused by injection. A drawback to angled injection is slight losses in penetration.

The shape of the normal injector orifice has been modified in the past to change the behavior of the fuel plume and flow-field. A diamond-shaped sonic injector orifice offers a way to increase the fuel jet penetration over an angled circular injector. Tomioka et al[29] experimentally tested a diamond-shaped injector in a Mach 3 cross flow. The jet to freestream dynamic pressure ratio was set to 2.0. With 15 degrees of yaw angle, the induced vortices lifted further off the surface to increase the penetration height. With 30 degrees yaw angle, the penetration was reduced but the mixing improved. Barber et al[30] injected helium into a Mach 3 air stream through both a circular and wedge-shaped orifice. The wedge-shaped injection scheme demonstrated more rapid penetration into the freestream and increased mixing when compared to the circular jet injection. The wedge configuration was also assumed to have reduced heat transfer in an actual combustor because of the lack of an upstream separation zone.

Another way to affect mixing in a flow is through the combination of several single transverse injectors to create a multiple injector array. The injector array has been used to increase mixing even further over single injectors. The array can trap and entrain freestream air between the injectors which can lead to larger fuel-air interfaces and enhanced mixing. Multiple injector arrays have been studied by Schetz[31], Fuller[32], Jacobsen[33] and Cox[34]. The array of transverse injectors acts as an aerodynamic ramp to enhance mixing. Jacobsen[33] showed that for a Mach 2.4 cross flow the aeroramp produced fuel-air mixing that was in line with mixing produced by physical ramps but with less pressure losses. The aeroramp varies the injection and toe-in angles among the orifices. The initial aeroramp was designed with nine injectors arranged in three rows of three injectors. The outside injectors were toed-in toward the centerline. Jacobsen[35] found increasing the toe-in angle of the exterior jets greatly increased the mixing efficiency and core penetration. Jacobsen[33] changed the nine-hole configuration to a four-hole configuration. According to Jacobesen[33], this resulted from the need for simplification of the fabrication intensive nine-hole design. The goal was to take advantage of the axial jet induced vorticity. Results showed that for a Mach 2.4 cross flow and a high molecular weight injectant, the aeroramp mixed better than the single circular orifice but incurred higher local total pressure losses. The aeroramp was first numerically analyzed in a scramjet combustor by Eklund and Gruber[36] and experimentally in a scramjet combustor by Gruber et al[37]. Two hydrocarbon fueled aeroramps were compared to a single row of four 15 degree angled holes. The aeroramp experiment showed improved mixing over the single row of injectors.

The typical fuels used in these injector designs for scramjet engines are hydrogen or hydrocarbon fuels. Hydrocarbon fuels are typically used for airbreathing systems operating below Mach 6 because of volumetric loading constraints. This research focuses on hydrogen fuels for a Mach 10 flight vehicle with Mach 4 flow in the combustor. Hydrogen is desirable as a fuel for hypersonic flight, because of its high energy content, fast reactions and high specific impulse. In addition, hydrogen fuels have a short ignition time which is extremely important for combustion at supersonic speeds. Lee[38] analyzed mixing characteristics of reacting and non-reacting flows using the three-dimensional k-ω turbulence model. He found little difference between reacting and non-reacting cases in

circulation, penetration distance and mixing rate. According to that reference, the similarities between the two runs is a result of the chemical reaction or heat release having little influence on the generation of vorticity.

1.2. Flow-Field Description

Fuel injection systems in scramjet engines can be described by the flow-field of jets in a cross flow. The physics of this flow are described below. The flow-field of jets in a cross flow will change if shocks are impinged on the jet. Shocks are naturally present in the inlet and combustion chamber of scramjet engines. To gain a better understanding of how the shocks affect fuel injection and performance, the physics of the interaction of shocks and jets is also discussed.

1.2.1. Transverse Jet Injection into Supersonic Cross flow

The flow-field of interest in this research is sonic jet injection into a supersonic cross-flow. A schematic of the three-dimensional flow-field formed by jet injection into a supersonic cross flow is shown in Figure 1.4. Also, a two-dimensional schematic of three-dimensional normal injection into a supersonic cross-flow over a flat plate with labeled recirculation regions can be found in Figure 1.5. The injected gas enters through a sonic nozzle at a higher static pressure than the freestream. The pressure difference causes the injected gas to expand by means of a Prandtl-Meyer expansion fan to be turned downstream by the incoming cross flow. The under-expanded gas is recompressed through a barrel shock wave and a Mach disk.

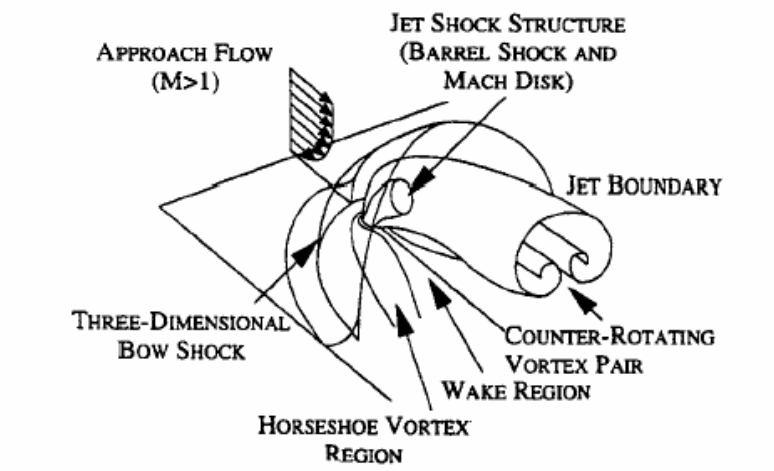

Figure 1.4. 3D Flow-field of normal injection into a supersonic cross flow[39]

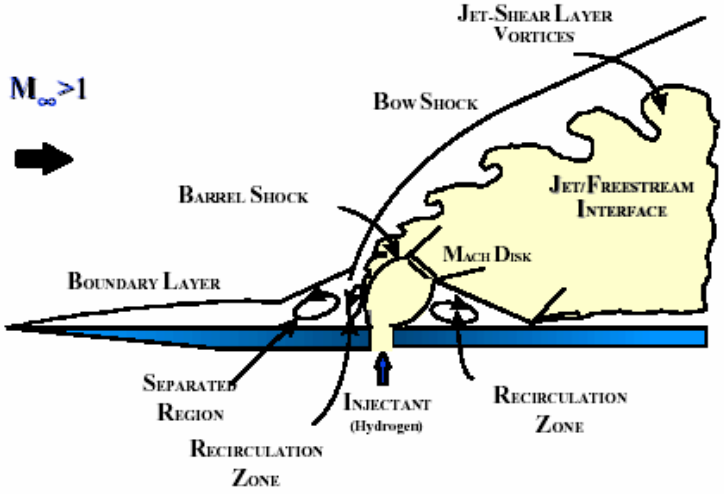

Figure 1.5. 2D Schematic of a 3D flow-field for normal injection into a supersonic cross flow [40]

Similar to flow around a blunt body on a surface, a recirculation region is formed both ahead of and behind injection. The oncoming flow is retarded by the impingement of the jet and separates immediately ahead of the bow shock created by the jet. The bow shock acts as a body in the flow creating a region of high pressure gradients. The size of the recirculation region and separation zone is determined by the size of the oncoming boundary layer and the pressure gradients. The trapped fluid in the recirculation region is forced around the jet creating a horseshoe vortex. The horseshoe vortex can be coupled with periodic vortices which form in the wake of the jet[41].

The recompression of the flow by the Mach disk in the plume along with pressure and viscous forces acting on the periphery of the jet forms a counter rotating vortex pair (CVP). Tam et al[42] performed experiments which showed that the Mach disk becomes more important as the jet injection-to-cross flow momentum flux ratio increases. This CVP is the primary mechanism for fuel-air mixing and is the most dominant vortex pair in the far-field of the interaction. As the vortex rotates, it entrains more air creating a larger fuel-air shear layer. It is through this shear layer that molecular mixing and diffusion occurs.

Vortex roll-up and vortex breakdown result from the vortex dynamics created by the interaction of the jet and cross flow. Coherent structures entraining fluid can increase the spreading of the interface between the fuel and air and increase turbulent mixing. Increases in molecular mixing can be accomplished by increasing turbulent mixing at the fuel-air interface with increasing size of the shear layer. Transverse injection combines both the near-field macromixing and the far-field, molecular mixing downstream. Martens et al[43] experimentally showed that a 50% improvement in shear layer growth enhanced the mean mixing rate of the shear layer.

Angled transverse injection reduces the strength and size of the initial bow shock as well as the Mach disk and barrel shock from expansion. The basic physics of the flow field remains the same.

1.2.2. Shock Impingement on Jet Injection

One mixing mechanism for hypersonic flows is the shock-enhancement mixing mechanism, in which the interaction between the mixing layer and an oblique shock creates strong axial vortices that stretch the fuel-air interface. The transfer of vorticity through the shock is the fundamental concept behind mixing enhancement. The interaction of a mixing layer composed of a light fluid accelerating in a heavy fluid with an oblique shock wave induces a misalignment between the density gradient in the mixing layer and the pressure gradient of the shock wave[44]. This misalignment creates instability in the fluid interface and then results in turbulent mixing.

Figure 1.6 is a model of the flow gradients in a jet and across a shock. A shock passage through the density gradient of a shear layer of heavy and light gases (red lines)

provides a pressure gradient (blue lines) which creates a distribution of vorticity over the boundary. The non-alignment of the density and the pressure gradients creates vorticity through the baroclinic effect. The baroclinic torque term in the vorticity equation, Equation [1-1], has been used to describe the creation of vorticity in compressible flows. To focus on this term, the flow is assumed to be inviscid with no body forces and no initial vorticity in the flow, which reduces the equation to Equation [1-2].

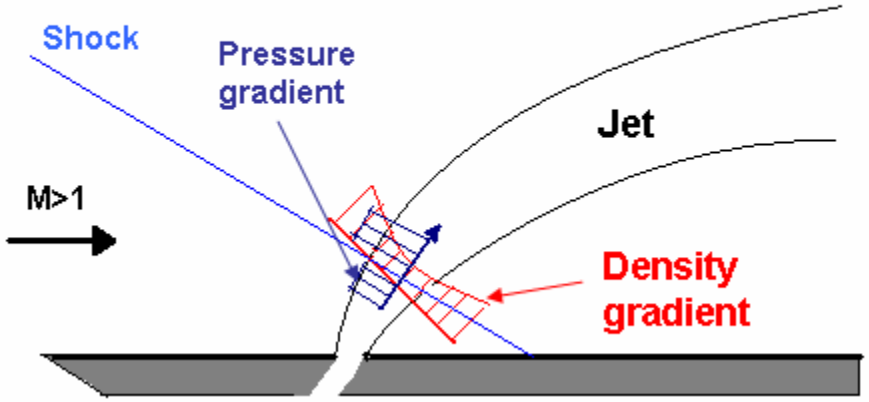

Figure 1.6 Normal jet streamline model.

$$\frac{D(\vec{\omega})}{Dt} = -\vec{\omega}\left(\nabla \cdot \vec{V}\right) + \left(\vec{\omega} \cdot \nabla \vec{V}\right) + \frac{1}{\rho^2}(\nabla\rho \times \nabla\vec{p}) + \nu\nabla\vec{\omega} \qquad \textbf{1-1}$$

$$\rho\frac{D(\omega/\rho)}{Dt} = \frac{1}{\rho^2}\left(\nabla\rho \times \nabla p\right) \qquad \textbf{1-2}$$

The baroclinic torque term contains a cross product which is nonzero when the gradients are non-parallel. Therefore to generate vorticity, the pressure and the density must have significant variations that are not collinear with each other; the largest misalignment will create the largest change in vorticity. Additional terms in Equation [1-1] are defined as the reduction in vorticity from expansion of the fluid (first term on the right hand side), vortex stretching which increases vorticity by stretching of vortex lines (second term on right hand side) and the viscous influence (last term on right hand side) which diffuses vorticity by viscosity. The first two terms on the right hand side distort vorticity already present in the flow. The term on the left hand side of Equations [1-1]

and [1-2] is the time rate of change of vorticity in a volume of fluid. The convective transport of vorticity is incorporated in the substantial derivative.

Moments in the fluid particles are created by the gradient misalignment. The moments cause the particles to rotate and change angular momentum. The resultant change in vorticity is a function of the shock strength, density jump and tangential velocity. The vorticity change is attributed to the tangential vorticity component. The normal vorticity is expected to be transferred unchanged through an oblique shock which can be explained by the Rankine-Hugoniot relations. The velocity component parallel to the surface (tangential) remains unchanged through a shock and since vorticity is the curl of the velocity vector, the normal vorticity remains unchanged through the discontinuity. Experiments performed by Agui[45] found that the longitudinal vorticity and lateral velocity signals were only slightly affected by the interaction of a shock and jet (Mach 3) (2-5% change which is within experimental uncertainty). However, it was also determined that the longitudinal velocity and lateral vorticity fluctuations were substantially amplified through the interaction (gains of 140%). Lee[46] confirmed Agui's findings numerically using DNS (Direct Numerical Simulation).

Andreopolulos[47] studied shock-wave turbulence interactions and suggested that amplification of velocity and vorticity fluctuations and substantial changes in length scales are the most important outcomes of the interaction of shock waves with turbulence of a shear layer. This may greatly affect mixing. Additionally, Lele[48] demonstrated that shock strength and the state of the incoming flow greatly affects the interaction of shock waves and turbulence and consequently mixing. Brassulis[49] proved that as the Mach number of the flow increases, the amplification across a discontinuity increases.

Lee[50] using DNS and Hannappel and Fredrich[51] using RANS simulations showed that all characteristic length scales decrease through shock interactions (longitudinal, lateral velocity, integral-length, longitudinal velocity microscales, dissipation length, integral-length and microscales of density fluctuations). Experiments performed by Briassulis[49] demonstrated that all scales are reduced considerably after interaction. Both experiments and numerical simulations found that the stronger the shock, the greater the change of the longitudinal length scales.

Jacquin and Geffroy[52] performed experiments of a heated jet impinged by a shock, where the density gradient was achieved by the difference in temperature of the jet and freestream. Turbulent amplification was measured in the middle of the jet wake, whereas the turbulent kinetic energy was decreased in the mixing layer region of the flow. The baroclinic vorticity effects contribute to the change in turbulent kinetic energy. Hermanson and Cetegen[53] also conducted experiments on non-uniform jets that interacted with traveling shocks. They concluded that there were considerable gains in vorticity after the shock through the generation of baroclinic torques. Hermening[54] performed similar experiments on jets which showed increases in mixing for the jets that where heavier than air. The change in vorticity was affected by the density of the gaseous jet. Hunt[55] performed experiments at Mach 2.8 on unswept compression ramps with a turbulent boundary layer. A direct correlation between the shock motion and the incoming velocity fluctuations was found. He also found that the size of the separation bubble correlates strongly with the shock wave position. Huh et al[56] demonstrated that shock waves enhanced the fuel-air mixing such that the flame lengths decreased by 30%. A wedge was used to create the shock in a Mach 3 cross flow.

Barakos[57] conducted numerical modeling of shock impingement on jets using several two-equation, linear and nonlinear models. Improved numerical prediction was achieved using the Menter SST k-ω model. In many cases, the model predictions were comparable to the ones obtained by the nonlinear models and experiments. Obata[58] performed a numerical study using the Wilcox k-ω model of the interaction of turbulent, planar jets with weak normal shock. The injected gas was varied between air, helium and carbon dioxide. The helium jets exhibited changes not apparent in air-CO_2 mix. The helium jet generated a vortex-like region and mixing was increased 30% at 30 diameters. The largest mixing occurred with the lightest injected gas.

1.3. Motivation for the Current Study

Hypersonic air-breathing flight vehicles are characterized by small flow residence times (milliseconds) in the engine. The short residence time of the flow particularly handicaps the fuel-air mixing process, which needs to be enhanced if the fuel is to be

mixed with the incoming air[59]. Enhanced mixing and rapid combustion are desirable because it implies an increase in combustion efficiency. The combustion efficiency is directly related to the engine performance, so increasing the efficiency will also enhance performance. Mixing improvement in high-speed flows can also be applied to a number of other fields such as thermal protection systems and vehicle control by jet thrusters. Understanding the complex interaction between the jet and the freestream air is an important part of the research necessary to turn scramjet engines into useable vehicles. Numerical modeling of these complex, turbulent flows can be advantageous in providing an important complement to experiment because of reduced turn around times of predictions when compared to experimental set-up and run-time and reduced cost over experimental testing. Also, numerical solutions can provide small-scale details that are difficult to obtain from experiments in hot flows. Understanding the influential parameters in modeling these flows will help contribute to the knowledge base of computational modeling of complex 3-D supersonic, turbulent, mixing flows.

1.4 Overview of Dissertation

The aim of the present work is to numerically examine the behavior of transverse injection of a light gas (hydrogen or helium) in a Mach 4 crossflow to simulate the flow in a scramjet combustor at Mach 10. The equations and methods used in the numerical analysis are discussed in Chapter 2. The computational domain and grid boundary conditions are explained in Chapter 3. The experimental setup and results used to validate the numerical analysis can be found in Chapter 4. Chapter 5 contains the numerical predictions for the simple, round-hole Baseline injector as well as the turbulent model sensitivity studies. Chapter 6 contains the remainder of the numerical predictions. First, an aeroramp injector consisting of four orifices and a diamond or wedge-shaped injector that is both aligned and yawed to the incoming flow are examined and compared to the Baseline injector. Next, shocks are impinged upon the jet at three locations downstream of injection. Lastly, comparisons of non-reacting and reacting simulations were performed. The conclusions from the presented work are summarized in Chapter 7.

Chapter 2: Governing Equations and Software

This chapter will discuss the equations used in numerical simulations of fluid flows. These equations include the compressible and incompressible forms of the governing Navier-Stokes equations and how they are manipulated into more useful forms. The equations that comprise the turbulence model and combustion model will also be discussed. The primary commercial numerical solver used in this research was AeroSoft's General Aerodynamics Simulation Program (GASP). A brief description of the features of GASP is provided below. For comparison, some calculations were made using FLUENT.

2.1 GASP

The GASP[60] Version 4.2.2 flow solver is a time-dependent, three-dimensional Reynolds averaged Navier-Stokes (RANS) solver. It solves the integral form of the governing equations using an upwind-based, finite-volume formulation. The solver is also capable of solving subsets of RANS which include thin-layer Navier-Stokes, parabolized Navier-Stokes (PNS), the Euler equations and the incompressible Navier-Stokes equations. GASP also uses Favre averaging for variable density flows.

GASP supports multi-block, structured grid topologies. Steady state solutions are marched in time using local time stepping, while time-accurate flows are solved using a dual-time stepping procedure.

In this study, the implicit Gauss-Seidel scheme was used. The inviscid fluxes were computed in two dimensions, i-direction (downstream) and j-direction (lateral), using third-order Roe flux difference splitting (FDS) with Min-Mod limiting. The Roe algorithm was chosen because the algorithm produces good resolution of shock discontinuities and it shows efficiency. For the case with four injectors, the Roe flux algorithm was unable to maintain stability in the vertical direction, therefore the Van Leer Flux algorithm was chosen instead. The Van Leer flux-vector splitting is robust and is

able to handle flows where other schemes cannot maintain stability, but it lacks the accuracy of the Roe FDS. The K-ω Menter Shear Stress Transport (SST) turbulence model was used. Of the viable options for two-equation turbulence models within GASP, the Menters SST model has been successfully used to model supersonic flows.

2.2 FLUENT

FLUENT Version 6.3.26[61] is a versatile flow solver. It solves the three-dimensional Reynolds averaged Navier-Stokes (RANS) equations using Favre averaging for variable density flows. Similar to GASP, FLUENT uses a control-volume based technique to solve for the integral form of the governing equations. Two numerical methods are available in FLUENT for flow solvers, a pressure-based solver or a density-based solver. The pressure-based segregated solution method solves the governing equations sequentially using an implicit formulation. The density-based coupled solver solves the governing equations simultaneously using either an implicit or explicit formulation. FLUENT supports structured and unstructured grids, as well as hybrid grids involving both structured and unstructured meshes.

For consistency with the models run using GASP, an implicit Gauss-Seidel scheme was used with the inviscid fluxes calculated using the Roe FDS algorithm in all three dimensions. The Van Leer flux was not an available option for use in FLUENT. The K-ω Menter SST turbulence model with compressibility effects was used to mimic the set-up of the GASP model. The numerical methods used for the analyses with GASP were closely replicated for the analysis with FLUENT.

2.3 Governing Equations

This section will introduce the compressible Navier-Stokes equations and then modify the equations into a vector and an integral form. GASP employs a time averaging technique (Reynolds averaging) to the integral form of the Navier-Stokes equations, which will also be discussed in this section.

2.3.1Compressible Navier-Stokes Equations

The governing equations used in computational fluid dynamics are the Navier-Stokes equations. Without assumptions, they apply to Newtonian fluids, compressible, viscous, unsteady and heat-conducting flows. The Navier-Stokes equations consist of the continuity equation, the momentum equation and the energy equation. The continuity equation is the conservation of mass, the momentum equation is Newton's second law of motion and the energy equation is the first law of thermodynamics. These equations in Cartesian coordinates are generally in the form of[60]:

Continuity Equation:

$$\frac{\partial \rho}{\partial t} + \frac{\partial (\rho U_i)}{\partial x_i} = 0 \qquad \textbf{2-1}$$

Momentum Equation:

$$\frac{\partial (\rho U_i)}{\partial t} + \frac{\partial}{\partial x}(\rho U_i U_j - \tau_{ij}) = -\frac{\partial P}{\partial x_i} \qquad \textbf{2-2}$$

Energy Equation:

$$\frac{\partial}{\partial t}[\rho E_t] + \frac{\partial}{\partial x_j}[\rho U_j (h + \frac{1}{2} U_i U_i)] = \frac{\partial}{\partial x_j}(U_i \tau_{ij}) - \frac{\partial q_j}{\partial x_j} \qquad \textbf{2-3}$$

Where

$$E_t = (e + \frac{1}{2} U_i U_i) \qquad \textbf{2-4}$$

$$\tau_{ij} = \mu[(\frac{\partial U_i}{\partial x_j} + \frac{\partial U_j}{\partial x_i}) - \frac{2}{3}\frac{\partial U_k}{\partial x_k}\delta_{ij}] \qquad \textbf{2-5}$$

$$q_j = -k\frac{\partial T}{\partial x_j} \qquad \textbf{2-6}$$

The term U_i is a vector representing the three velocity components. The term τ_{ij} is the viscous stress tensor. The Kronecker delta, δ_{ij}, takes the value of one if i=j and zero if i≠j. The momentum equation is comprised of three equations; one in each spatial direction.

Therefore, there are five equations. There are more unknowns than there are equations; as a result, it is necessary to add an additional equation to close the system. The additional equation is usually an equation of state that relates the thermodynamic variables (p,ρ,T, e,h). If e and ρ are assumed to be the independent variables then we have the relations:

$$p = p(e, \rho) \qquad \text{and} \qquad T = T(e, \rho) \tag{2-7}$$

If a thermally perfect gas is assumed, then the perfect gas equation of state can be used for the first relation,

$$p = \rho RT \tag{2-8}$$

where R is the gas constant. If the gas is calorically perfect, a perfect gas with constant specific heats, we can use the linear relation:

$$e = c_v T \tag{2-9}$$

For fluids that are not calorically perfect, the coefficients of viscosity and thermal conductivity can be related using kinetic theory[60].

2.3.2 Vector Form of the Compressible Navier-Stokes Equations

GASP solves the integral, vector form of the RANS equations; the vector form will be discussed here. The continuity equation, three momentum equations and the energy equation are combined into a vector equation with vectors $\vec{U}, \vec{E}, \vec{F}, \vec{G}$ and $\vec{J}$. The vector $\vec{U}$ is a column vector of the conserved variables, the vectors $\vec{E}, \vec{F}$ and $\vec{G}$ are column vectors which contain the flux terms and $\vec{J}$ is the source term vector. The vector form of the compressible Navier-Stokes equations in cartesian coordinates without body forces or external heat addition can be written as:

$$\frac{\partial \vec{U}}{\partial t} + \frac{\partial \vec{E}}{\partial x} + \frac{\partial \vec{F}}{\partial y} + \frac{\partial \vec{G}}{\partial z} = \vec{J} \tag{2-10}$$

Equation [2.10] can be simplified by separating the terms $\vec{E}, \vec{F}$ and $\vec{G}$ into the viscous fluxes and inviscid fluxes. Equation [2.10] now becomes:

$$\frac{\partial \vec{U}}{\partial t} + \left(\frac{\partial \vec{E}}{\partial x} + \frac{\partial \vec{F}}{\partial y} + \frac{\partial \vec{G}}{\partial z} \right) = \left(\frac{\partial \vec{E}_v}{\partial x} + \frac{\partial \vec{F}_v}{\partial y} + \frac{\partial \vec{G}_v}{\partial z} \right) + \vec{J} \qquad \textbf{2-11}$$

The $\vec{U}$ vector contains the following variables:

$$\vec{U} = \begin{bmatrix} \rho \\ \rho u \\ \rho v \\ \rho w \\ \rho E_t \end{bmatrix} \qquad \textbf{2-12}$$

The inviscid flux vectors, $\vec{E}, \vec{F}$ and $\vec{G}$ are:

$$\vec{E} = \begin{bmatrix} \rho u \\ \rho u^2 + p \\ \rho uv \\ \rho uw \\ (E_t + p)u \end{bmatrix}$$

$$\vec{F} = \begin{bmatrix} \rho v \\ \rho uv \\ \rho v^2 + p \\ \rho vw \\ (E_t + p)v \end{bmatrix}$$

$$\vec{G} = \begin{bmatrix} \rho w \\ \rho uw \\ \rho vw \\ \rho w^2 + p \\ (E_t + p)w \end{bmatrix} \qquad \textbf{2-13}$$

The viscous flux vectors, $\vec{E}_v, \vec{F}_v$ and $\vec{G}_v$ are:

$$\vec{E}_v = \begin{bmatrix} 0 \\ \tau_{xx} \\ \tau_{xy} \\ \tau_{xz} \\ u\tau_{xx} + v\tau_{xy} + w\tau_{xz} - q_x \end{bmatrix}$$

$$\vec{F}_v = \begin{bmatrix} 0 \\ \tau_{xy} \\ \tau_{yy} \\ \tau_{yz} \\ u\tau_{xy} + v\tau_{yy} + w\tau_{yz} - q_y \end{bmatrix}$$

$$\vec{G}_v = \begin{bmatrix} 0 \\ \tau_{xz} \\ \tau_{yz} \\ \tau_{zz} \\ u\tau_{xz} + v\tau_{yz} + w\tau_{zz} - q_z \end{bmatrix} \qquad \textbf{2-14}$$

The inviscid fluxes, $\vec{E}, \vec{F}$ and $\vec{G}$, and the viscous fluxes, $\vec{E}_v, \vec{F}_v$ and $\vec{G}_v$ can be combined into matrices, $F(\vec{U})$ and $F(\vec{U}_v)$. Simplifying equation [2.11], the vector form of the compressible Navier-Stokes equations can be obtained.

$$\frac{\partial \vec{U}}{\partial t} + \nabla \vec{F}(\vec{U}) - \nabla \vec{F}_v(\vec{U}) = \vec{J} \qquad \textbf{2-15}$$

2.3.3 Integral Form of the Compressible Navier-Stokes Equations

The integral form is obtained by integrating Equation 2.15 over the volume.

$$\iiint \left(\frac{\partial \vec{U}}{\partial t} + \nabla \vec{F}(\vec{U}) - \nabla \vec{F}_v(\vec{U}) \right) dV = \iiint \vec{J} dV \qquad \textbf{2-16}$$

Gauss' theorem, equation [2.17], is used to simplify the integral by transforming the volume integral into a surface integral.

$$\iiint \nabla \vec{F} dV = \iint \vec{F} \cdot \vec{n} dS \qquad \textbf{2-17}$$

Applying equation [2.17] to equation [2.16], the integral form of the (vector) Navier-Stokes equation can be obtained:

$$\frac{\partial}{\partial t} \iiint \vec{U} dV + \iint \left(\vec{F}(\vec{U}) - \vec{F}_v(\vec{U}) \right) \cdot \vec{n} dA = \iiint \vec{J} dV \qquad \textbf{2-18}$$

2.3.4 Reynolds-Averaged Navier-Stokes Equations

GASP solves the Reynolds averaged (RANS) or time-averaged Navier-Stokes. The RANS equations are derived by decomposing the dependent variables into time-mean and fluctuating components. This is called Reynolds decomposition. For example, the following equation time averages the u component of velocity,

$$u = \overline{U} + u' \qquad \textbf{2-19}$$

where $\overline{U}$ is the Reynolds averaged or mean velocity and u' is the fluctuating component about that average; $\overline{U}$ is obtained from the following:

$$\overline{U} \equiv \int_{t_o}^{t_o + \Delta t} u dt \qquad \textbf{2-20}$$

Note: the time-average of the fluctuating term, $\overline{u'}$ is defined to be zero.

Decomposing the Navier-Stokes equations and applying the note from above, equations [2.1, 2.2 and 2.3] become:

$$\frac{\partial \rho}{\partial t} + \frac{\partial}{\partial x_i}\left(\rho u_j\right) = 0$$

$$\frac{\partial}{\partial t}\left(\rho u_i\right) + \frac{\partial}{\partial x_j}\left(\rho u_i u_j\right) = -\frac{\partial \overline{p}}{\partial x_i} + \frac{\partial}{\partial x_j}\left(\tau_{ij} - \rho\overline{u'_i\, u'_j}\right)$$

$$\frac{\partial}{\partial t}\left(\rho c_p T\right) + \frac{\partial}{\partial x_j}\left(\rho c_p T u_j\right) = \frac{\partial p}{\partial t} + u_j \frac{\partial p}{\partial x_j} + \overline{u''_j \frac{\partial p}{\partial x_j}} + \frac{\partial}{\partial x_j}\left(k\frac{\partial T}{\partial x_j} + k\frac{\partial T''}{\partial x_j} - c_p\overline{\rho T'' u''_j}\right) + \overline{\Phi}$$

2-21

Where:

$$\tau_{ij} = \mu\left(\frac{\partial u_i}{\partial x_j} + \frac{\partial u_j}{\partial x_i}\right) \qquad \textbf{2-22}$$

$$\overline{\Phi} = \overline{\tau_{ij}\frac{\partial u_i}{\partial x_j}} \qquad \textbf{2-23}$$

Note: the over-bar has been dropped and it is now assumed that the terms are time averaged.

Time averaging the equations of motion creates new terms that need to be modeled. Looking at the Reynolds momentum equations, the new terms to be modeled are the turbulent stresses, $-\rho\overline{u'_i\, u'_j}$. This is called the Reynolds stress tensor and has six components, six more unknowns. The Reynolds stress tensor contains all of the influence of turbulence but the fluctuating velocity components are unknown and a simple method does not exist to solve for them. In an attempt to complete the system of equations, turbulence models have been created to replace the Reynolds stress terms with a model of the mean-flow variables. This is the basis for turbulence modeling.

2.3.5 Favre-Averaged Navier-Stokes Equations

For variable density flows, Favre-averages or mass-weight averages can be taken of the governing equations following the same procedures as the Reynolds decomposition. Any variable can be decomposed into a mean part, $\widetilde{a}$, and a fluctuating part, a'':

$$a = \widetilde{a} + a'' \qquad \textbf{2-24}$$

Favre averages are defined as

$$\widetilde{a} \equiv \frac{\overline{\rho a}}{\overline{\rho}} \qquad \textbf{2-25}$$

With the following important auxiliary equation:

$$\overline{a''} \neq 0 \qquad \textbf{2-26}$$

Using the above approach, the Favre-Averaged Navier Stokes equations can be obtained:

$$\frac{\partial \overline{\rho}}{\partial t} + \frac{\partial (\overline{\rho}\widetilde{U}_i)}{\partial x_i} = 0 \qquad \textbf{2-27}$$

$$\frac{\partial (\overline{\rho}\widetilde{U}_i)}{\partial t} + \frac{\partial}{\partial x_j}\left[\overline{\rho}\widetilde{U}_i\widetilde{U}_j + \overline{p}\delta_{ij} + \overline{\rho U_i'' U_j''} - \overline{\tau_{ji}}\right] = 0 \qquad \textbf{2-28}$$

$$\frac{\partial}{\partial t}\left[\overline{\rho}\widetilde{E}_t\right] + \frac{\partial}{\partial x_j}\left[\rho\widetilde{U}_j\widetilde{E}_t + \widetilde{U}_j p + \overline{U_j'' p} + \overline{\rho U_j'' E_t''}\right] = \frac{\partial}{\partial x_j}\left[\overline{U_i \tau_{ij}} - \overline{q_j}\right] \qquad \textbf{2-29}$$

2.4 Turbulence Models

In the study of turbulent flows the ultimate objective is to obtain a tractable quantitative model that can be used to calculate quantities of interest and practical relevance[62]. According to Aerosoft's technical manual[60], any credible turbulence model must at a minimum reproduce the law of the wall and the skin-friction distribution within engineering accuracy for a simple flat-plate flow. Leaders in the field of turbulence-modeling research also investigate other more subtle turbulence features such as proper near-wall asymptotic behavior in the turbulence kinetic energy, apparent viscosity, and

Reynolds stress. Additional important features include capturing the sharp peak in turbulent kinetic energy, K, near the wall, acceptable accuracy for strong favorable and adverse pressure gradients, computational ease, and accurate prediction of the transition point (where turbulent production catches up with the dissipation of turbulence).

The problem of modeling the unknown Reynolds stress terms is very difficult. Some models work better than others for solving specific flows. Various models and simulations create a hierarchy of accuracy and efficiency. The simplest model and less broadly applicable is a zero-equation model and currently, the most complex simulation is direct numerical simulation (DNS). The RANS equations-based models are the most widely used because of their versatility, efficiency and cost. However, as technologies improve the simulations of LES, DES and even DNS become more feasible and in some cases practical to obtain an accurate solution.

DNS is an accurate numerical solver that resolves all spatial and temporal scales of turbulence, however it is extremely computationally intensive. DNS involves generating meshes that are fine enough to resolve the smallest dissipative scales, the Kolmogorov scales and also capture the large-scale motions. The cost and computational power necessary to complete even the simplest of analyses is extremely high. The computational power required for DNS increases rapidly with Reynolds number of the simulated flow, for example, a $Re_L = 94$ would take 20 min CPU-time to resolve using DNS, a $Re_L = 96{,}000$ would take 5,000 years CPU-time to resolve[63]! For high Reynolds number flows, DNS is not a viable option and will not be discussed further in this research. For specific simulation details see Reference 64.

A step down in complexity from DNS is the large eddy simulation, LES. LES uses a model for the small-scale motions instead of directly resolving them as in DNS. The large, 3D, unsteady turbulent motions are still directly represented. By modeling the small-scale turbulent eddies (and not solving directly for them), a coarser grid refinement and larger time-steps than DNS can be used. This alleviates some of the computational cost. However, the mesh required and the computational time are still substantially larger than those required for RANS calculations. LES involves a filtering process of the time-dependent Navier-Stokes equations into a residual (subgrid-scale, SGS) component and a filtered component. A low-pass filtering operation results in a filtered velocity field that

directly represents the velocities of the large-scale eddies. Usually, the filter width is taken to be proportional to the local grid spacing. The subgrid-scale components, the residual-stresses, are modeled using an eddy-viscosity model. For free-shear flows, LES is more practical (in a computational sense) than DNS but is two orders of magnitude in each spatial direction more expensive than a Reynold's stress model[63]. The computational demands increase significantly for wall-bounded flows because the near-wall motions scale with the viscous length-scales and this requires a very fine grid near the wall. For wall-bounded flows, LES cost increases as $Re^{1.8,\ 63}$. This research involves near-wall resolution of a high Re number flow, therefore, LES will not be used. For specific equations please see References 63 and 65.

A practical and more numerically feasible variation of LES is direct eddy simulation, DES, proposed by Spalart et al in 1997[66]. DES uses RANS (Spalart and Allmaras one-equation model or Menter SST two-equation model) formulations in the near-wall regions and blends to a LES formulation for resolution of the unsteady three-dimensional, large-scale, turbulent motions in the free-shear region. Using DES maintains the increased level of detail of LES while reducing cost and time for resolution by the incorporation of RANS modeling. DES uses the distance between cell centers of the computational grid and distance from the wall to determine when to act as a RANS model or LES. The applications of DES today have been predominately for highly unsteady flows with large separation regions, for example, flow over a sphere[67,68] and around an aircraft forebody[69,70]. The main advantage of DES is the application to high Reynolds number flows (which is not practical in either DNS or LES). Two of the disadvantages of DES over complete RANS modeling are an increase in computational needs and for attached flows, there is a larger variation of the prediction in the "grey" area between strictly RANS and strictly LES approaches[71]. DES is a relatively young approach in the computational world and still requires validation for attached or mildly separated flows.

A practical and most widely used approach to modeling of turbulent flows is that of turbulent viscosity models. The accuracy and applicability to the broadest range of flow-fields increases with the number of equations modeled. The zero, one and two-equation turbulence models used with the RANS equations, including the model used in

this research, are turbulent viscosity models. These models are based on the Boussinesq approximation and provide closure to the RANS equations with expressions for the turbulent viscosity and turbulent length scale.

A zero-equation model represents the turbulence velocity scale as a function of the mixing length, l_t, and distance away from the wall. The mixing length varies depending on the local y value for the inner-region of the boundary layer and is constant for the outer region of the boundary layer. The downside to a zero-equation model is the lack of turbulence viscosity, μ_t, in regions where the mean flow gradient is zero.

One-equation models add a level of complexity by assuming that the turbulent velocity scale is a function of the turbulent kinetic energy, K. The turbulent viscosity for a one-equation model is a function of the local density, ρ, turbulent length scale, l_t and turbulent kinetic energy, K. It is represented by the equation:

$$\mu_t \approx \rho\sqrt{K}l_t \qquad \textbf{2-30}$$

Two-equation models expand upon the one-equation model by modeling the length scale as a convecting flow property[60]. The model used in this research is a two-equation model. New unknown variables are introduced in the shear stress equations and they are the turbulent eddy viscosity, μ_t and the turbulent kinetic energy, K. The viscous shear stresses that are found in the momentum terms of the viscous fluxes (equation [2.14]) are defined for the two equation models as:

$$\begin{aligned}
\tau_{xx} &= \frac{2}{3}(\mu+\mu_t)\left(2\frac{\partial u}{\partial x}-\frac{dv}{\partial y}-\frac{\partial w}{\partial z}\right)-\frac{2}{3}\rho K \\
\tau_{yy} &= \frac{2}{3}(\mu+\mu_t)\left(2\frac{\partial v}{\partial y}-\frac{du}{\partial x}-\frac{\partial w}{\partial z}\right)-\frac{2}{3}\rho K \qquad \textbf{2-31} \\
\tau_{zz} &= \frac{2}{3}(\mu+\mu_t)\left(2\frac{\partial w}{\partial z}-\frac{dv}{\partial y}-\frac{\partial u}{\partial x}\right)-\frac{2}{3}\rho K
\end{aligned}$$

$$\tau_{xy} = \tau_{yx} = \frac{2}{3}(\mu + \mu_t)\left(\frac{\partial u}{\partial y} + \frac{\partial v}{\partial x}\right)$$
$$\tau_{xz} = \tau_{zx} = \frac{2}{3}(\mu + \mu_t)\left(\frac{\partial u}{\partial z} + \frac{\partial w}{\partial x}\right) \quad \textbf{2-32}$$
$$\tau_{yw} = \tau_{wy} = \frac{2}{3}(\mu + \mu_t)\left(\frac{\partial w}{\partial y} + \frac{\partial v}{\partial z}\right)$$

The two-equation model provides closure by developing methods for solving for the unknown quantities found in these equations. The turbulent kinetic energy, K, and an additional turbulent parameter such as turbulent dissipation rate, ε, or turbulent frequency, ω, is used to calculate the turbulent length scale and turbulent viscosity. The turbulent length scales for the K-ε and the K-ω models are defined as:

$$l_t = K^{3/2} / \varepsilon \quad \text{[K- ε]} \quad \textbf{2-33}$$

$$l_t = \frac{\sqrt{K}}{\omega} \quad \text{[K-ω]} \quad \textbf{2-34}$$

The eddy viscosity is determined from the turbulence parameters, a modeling constant, C_u, a wall-damping function, *f*, that approaches zero at the wall, and the state variables through[63]

$$\mu_t = C_\mu f \rho K^2 / \varepsilon \quad \text{[K- ε]} \quad \textbf{2-35}$$

$$\mu_t = C_\mu \rho K / \omega \quad \text{[K- ω]} \quad \textbf{2-36}$$

Since this research uses variants of the K-ε and K-ω models, only equations representative of those models will be discussed in detail.

Additional equations that produce unknown variables arise from the energy equation, the heat fluxes, q_x, q_y and q_z. They are defined for two-equation models[60]:

$$q_x = -(k + k_t)\frac{\partial T}{\partial x} - \left(\mu + \frac{\mu_t}{\mathrm{Pr}_k}\right)\frac{\partial K}{\partial x}$$
$$q_y = -(k + k_t)\frac{\partial T}{\partial y} - \left(\mu + \frac{\mu_t}{\mathrm{Pr}_k}\right)\frac{\partial K}{\partial y} \qquad \textbf{2-37}$$
$$q_z = -(k + k_t)\frac{\partial T}{\partial z} - \left(\mu + \frac{\mu_t}{\mathrm{Pr}_k}\right)\frac{\partial K}{\partial z}$$

Two more new terms come out of the heat fluxes, the turbulent thermal conductivity, k_t and the turbulent kinetic energy closure coefficient, or turbulent Prandtl number, Pr_K. The ratio of diffusion of momentum to the diffusion of heat is the Prandtl number,

$$\mathrm{Pr} = \frac{C_p \mu}{K} \qquad \textbf{2-38}$$

The turbulent Prandtl number is defined using the turbulent viscosity and turbulent conductivity. Supersonic numerical solutions are highly dependent on the value of the turbulent Prandtl number. The closure coefficients can be determined empirically.

The turbulence model selected here for jet injection into a supersonic cross flow is the Menter Shear Stress Transport (SST) model. The Menter SST model is a blend of the Wilcox (1988) K-ω turbulence model in the near wall region and the K-ε turbulence model in the outer boundary layer and free-shear regions. Typically, the Wilcox K-ω has been successful in predicting wall-bounded flows, while K-ε is the preferred model for free shear flows. Therefore, the Menter SST model captures the best qualities of the most used two-equation turbulence models. Each of these models will be discussed in more detail.

2.4.1 The K-ε Turbulence Model

The first turbulence model to be discussed is the most widely used two-equation model. Closure to the transport equations is sought by modeling of the turbulent velocity and length using the terms, K, turbulent kinetic energy and ε, dissipation of turbulent kinetic energy. These two quantities are used to solve for the turbulent length scale, a timescale, and the turbulent viscosity as shown earlier. A damping function can be used

with this model to help accurately integrate through the viscous sublayer which can otherwise cause significant stiffness. The K-ε model used in the Menter SST turbulence model is a high Reynolds number model that has been transformed into a K-ω formulation. This changes the modeling constants and the cross-diffusion term. The turbulent dissipation, ε, is replaced by the turbulent frequency, ω. The transformed K-ε model defines the following closure equations: the eddy viscosity, Equation [2-33], turbulence kinetic energy and specific dissipation rate:

Turbulence Kinetic Energy

$$\rho\frac{\partial k}{\partial t}+\frac{\partial(\rho U_j k)}{\partial x_j}=\tau_{ij}\frac{\partial u_i}{\partial x_j}-C_{D_K}\rho k\omega+\frac{\partial}{\partial x_j}\left[\left(\mu\ +\sigma_{K2}\mu_t\right)\frac{\partial k}{\partial x_j}\right] \qquad \textbf{2-39}$$

Specific Dissipation Rate (transformed and defined for use with the K-ω model)

$$\rho\frac{\partial \omega}{\partial t}+\frac{\partial(pU_j\omega)}{\partial x_j}=\frac{\gamma_2}{\upsilon_2}\tau_{ij}\frac{\partial u_i}{\partial x_j}-\beta_2\rho\omega^2+\frac{\partial}{\partial x_j}\left[\left(\mu+\sigma_{\omega2}\mu_T\right)\frac{\partial \omega}{\partial x_j}\right]+2\rho\sigma_{\omega2}\frac{1}{\omega}\frac{\partial k}{\partial x_j}\frac{\partial \omega}{\partial x_j} \qquad \textbf{2-40}$$

Constants are:

$$\sigma_{k2}=1.0,\qquad \sigma_{\omega2}=0.856,\quad \beta_2=0.0828$$

$$C_{DK}=0.09,\quad K=0.41,\qquad \gamma_2=\beta_2/\,C_{DK}-\sigma_{\omega2}\kappa^2/\sqrt{C_{DK}}$$

2.4.2 The Wilcox K-ω (1998) Model

The second turbulence model used to generate the Menter SST model is the two-equation Wilcox K-ω (1998) model. This robust model is the model of choice in the sublayer of the boundary layer[63]. The Wilcox K-ω model handles adverse pressure gradients well and is integrated through the laminar sublayer without a damping function. The model is consistent with the defect-layer structure for all pressure gradients and can be integrated through the sublayer without damping functions. This model does require a fine boundary layer grid with initial wall spacing small enough to produce a y+ less than one,

$$y^+\equiv\frac{yu_*}{v} \qquad \textbf{2-41}$$

Where u_* is called the friction velocity which is defined as the square root of the wall shear divided by density, $u_* = \sqrt{\frac{\tau_w}{\rho}}$.

The Wilcox model tends to be very numerically stable. The k-ω model solves for the turbulent kinetic energy, K and the turbulent frequency, ω. The turbulent frequency can be referred to as the ratio of the rate of dissipation, ε, per unit of turbulence kinetic energy, K. The Wilcox K-ω model equations use the following closure equations: the eddy viscosity, Equation [2-34], turbulence kinetic energy and specific dissipation rate.

Turbulence Kinetic Energy

$$\rho\frac{\partial k}{\partial t}+\frac{\partial(\rho U_j k)}{\partial x_j}=\frac{\partial \tau_{ij}^{K}}{\partial x_j}-C_{D_K}\rho k\omega+\frac{\partial}{\partial x_j}\left[\left(\mu+\sigma_{k1}\mu_t\right)\frac{\partial k}{\partial x_j}\right] \qquad \textbf{2-42}$$

Specific Dissipation Rate

$$\rho\frac{\partial \omega}{\partial t}+\frac{\partial(pU_j\omega)}{\partial x_j}=\frac{\gamma_1}{\upsilon_t}\tau_{ij}\frac{\partial u_i}{\partial x_j}-\beta_1\rho\omega^2+\frac{\partial}{\partial x_j}\left[\left(\mu+\sigma_{\omega 1}\mu_T\right)\frac{\partial \omega}{\partial x_j}\right] \qquad \textbf{2-43}$$

Constants are:

$$\sigma_{k1}=0.5, \qquad \sigma_{\omega 1}=0.5, \qquad \beta_1=0.0750$$

$$C_{DK}=0.09, \qquad \kappa=0.41, \qquad \gamma_2=\beta_1/C_{DK}-\sigma_{\omega 1}\kappa^2/\sqrt{C_{DK}}$$

2.3.3 Menter Shear Stress Transport Model

The Menter SST model blends the robust Wilcox K-ω model in the near-wall region with the freestream accuracy of the K-ε model. A blending function, F_1, is used to transition between the two turbulence formulations. The model performs similarly to the Wilcox model, but avoids the strong freestream sensitivity of the model[72].

The Menter model uses the K-ω formulation in the logarithmic region of the boundary layer, because its performance is superior to the K-ε model there. In the wake region of the boundary layer, the K-ω model is abandoned in favor of the K-ε model. The switch occurs because the k-ω model has a very strong sensitivity to the freestream value,

$\omega_{f,}$ specified for ω outside the boundary layer. The K-ε model does not vary as widely in this region with changes to ω_f.

The turbulent kinetic and specific dissipation equations for the high-Reynolds number K-ε model above are multiplied by the quantity 1.0 minus the blending function, F_1, while the turbulent kinetic and specific dissipation equations of the K-ω model above are multiplied by F_1. F_1 takes on a value of unity in the sublayer and log region of the boundary layer and gradually switches to zero in the wake region. The resultant equations are:

Turbulence Kinetic Energy

$$\rho\frac{\partial k}{\partial t}+\frac{\partial(\rho U_j k)}{\partial x_j}=\tau_{ij}\frac{\partial u_i}{\partial x_j}-C_{D_K}\rho k\omega+\frac{\partial}{\partial x_j}\left[\left(\mu\ +\sigma_K\mu_t\right)\frac{\partial k}{\partial x_j}\right] \qquad \textbf{2-44}$$

Specific Dissipation Rate

$$\rho\frac{\partial \omega}{\partial t}+\frac{\partial(pU_j\omega)}{\partial x_j}=\frac{\gamma}{\upsilon_t}\tau_{ij}\frac{\partial u_i}{\partial x_j}-\beta\rho\omega^2+\frac{\partial}{\partial x_j}\left[\left(\mu+\sigma_\omega\mu_T\right)\frac{\partial \omega}{\partial x_j}\right]+2\rho\left(1-F_1\right)\sigma_{\omega 2}\frac{1}{\omega}\frac{\partial k}{\partial x_j}\frac{\partial \omega}{\partial x_j} \qquad \textbf{2-45}$$

Letting Φ_1 represent any constant in the original model (σ_{k1}, …), Φ_2 any constant in the transformed k-ε model (σ_{k2}, …) and Φ the corresponding constant of the new model, then the relation between them is:

$$\Phi=F_1\Phi_1+\left(1-F_1\right)\Phi_2 \qquad \textbf{2-46}$$

Constants are[72]:

$$\sigma_{k1}=0.85,\qquad \sigma_{\omega 1}=0.5,\qquad \beta_1=0.0750$$
$$C_{DK}=0.09,\qquad \kappa=0.41,\qquad \gamma_2=\beta_1/\,C_{DK}-\sigma_{\omega 1}\kappa^2/\sqrt{\ }C_{DK}$$

The definition of eddy viscosity is also modified to account for the transport of the principal turbulent shear stress. This is the Shear Stress Transport model (SST). The eddy viscosity is now defined as:

$$\nu_t=\frac{a_1 k}{\max\left(a_1\omega,\Omega F_2\right)} \qquad \textbf{2-47}$$

Where Ω is the absolute value of the vorticity. F_2 is given by

$$F_2 = \tanh\left(\arg_2^2\right) \quad \textbf{2-48}$$

$$\arg_2 = \max\left(2\frac{\sqrt{k}}{0.09\omega y}, \frac{500\upsilon}{y^2\omega}\right) \quad \textbf{2-49}$$

F2 is a function that is 1 for boundary layer flows and zero for free-shear flows. In an adverse pressure gradient boundary layer, production of k is larger than its dissipation (or $\Omega > a_1\omega$).

2.4 Combustion Modeling

The majority of analysis conducted in this document was done with the assumption of a frozen flow, non-reacting analysis. Thermally perfect gases assumes the range of intermolecular forces is much smaller than the average molecular spacing which is, in turn, much smaller than the average distance a molecule travels between collisions[60]. The particles are weakly interacting. By assuming perfect gases, the internal energy becomes a function of temperature only and the thermodynamic equations are simplified. For reacting flows the internal energy includes contributions from translational, rotational and vibrational energies as well as internal energy due to the presence of chemical bonds (heat of formation of a molecule). The equations used to model the reacting analysis in this research will now be discussed.

Species Navier Stokes

The Navier Stokes equations [2-1], [2-2] and [2-3] above are modified for multiple species, reacting flows. The term f_1 denotes the mass fraction of species i. The $\vec{U}$ vector now has an additional term, ρf_i:

$$\vec{U} = \begin{bmatrix} \rho \\ \rho u \\ \rho v \\ \rho w \\ \rho E_t \\ \rho f_i \end{bmatrix} \qquad \textbf{2-50}$$

The inviscid flux vectors, $\vec{E}, \vec{F}$ and $\vec{G}$ are modified to contain an additional term, ρf_i:

$$\vec{E} = \begin{bmatrix} \rho u \\ \rho u^2 + p \\ \rho uv \\ \rho uw \\ (E_t + p)u \\ \rho u f_i \end{bmatrix}$$

$$\vec{F} = \begin{bmatrix} \rho v \\ \rho uv \\ \rho v^2 + p \\ \rho vw \\ (E_t + p)v \\ \rho v f_i \end{bmatrix}$$

$$\vec{G} = \begin{bmatrix} \rho w \\ \rho uw \\ \rho vw \\ \rho w^2 + p \\ (E_t + p)w \\ \rho w f_i \end{bmatrix} \qquad \textbf{2-51}$$

The viscous flux vectors, $\vec{E}_v, \vec{F}_v$ and $\vec{G}_v$ with the directional diffusion velocities, $\tilde{u}, \tilde{v}, \tilde{w}$ are now:

$$\vec{E}_v = \begin{bmatrix} 0 \\ \tau_{xx} \\ \tau_{xy} \\ \tau_{xz} \\ u\tau_{xx} + v\tau_{xy} + w\tau_{xz} - q_x \\ \rho\tilde{u}_i f_i \end{bmatrix} \quad \vec{F}_v = \begin{bmatrix} 0 \\ \tau_{xy} \\ \tau_{yy} \\ \tau_{yz} \\ u\tau_{xy} + v\tau_{yy} + w\tau_{yz} - q_y \\ \rho\tilde{v}_i f_i \end{bmatrix} \quad \vec{G}_v = \begin{bmatrix} 0 \\ \tau_{xz} \\ \tau_{yz} \\ \tau_{zz} \\ u\tau_{xz} + v\tau_{yz} + w\tau_{zz} - q_z \\ \rho\tilde{w}_i f_i \end{bmatrix} \qquad \textbf{2-52}$$

The heat fluxes are also modified:

$$q_x = -(k + k_t)\frac{\partial T}{\partial x} + \rho\sum_{i=1}^{N_s} h_i f_i \tilde{u}_i + RT\sum_{i=1}^{N_s}\sum_{j=1}^{N_s}\left(\frac{X_j D_{Ti}}{M_i D_{ij}}\right)(\tilde{u}_i - \tilde{u}_j)$$

$$q_y = -(k + k_t)\frac{\partial T}{\partial y} + \rho\sum_{i=1}^{N_s} h_i f_i \tilde{v}_i + RT\sum_{i=1}^{N_s}\sum_{j=1}^{N_s}\left(\frac{X_j D_{Ti}}{M_i D_{ij}}\right)(\tilde{v}_i - \tilde{v}_j)$$

$$q_z = -(k + k_t)\frac{\partial T}{\partial z} + \rho\sum_{i=1}^{N_s} h_i f_i \tilde{w}_i + RT\sum_{i=1}^{N_s}\sum_{j=1}^{N_s}\left(\frac{X_j D_{Ti}}{M_i D_{ij}}\right)(\tilde{w}_i - \tilde{w}_j) \qquad \textbf{2-53}$$

Where D_{ij} is the binary diffusion coefficient, D_T is the thermal diffusion coefficient, X_i is the mole fraction of species i and M_i is the molecular weight of species i. There are N_s

chemical species and therefore (N_s-1) chemical equations must be solved for the species f_i[73]. The species enthalpy in Equation [2-49] is defined by the base enthalpy:

$$h_i = h_i^o + \int_{T_R}^{T} C_{P_i} dT \qquad \textbf{2-54}$$

The equation of state must be modified to include multiple species:

$$P = \rho RT \sum_{i=1}^{N_s} \frac{f_i}{M_i} \qquad \textbf{2-55}$$

In order to solve Equation [2-54], the thermodynamic quantity, C_{Pi}, the specific heat for each species, must be known. For the reacting flow in the model used in this paper, the specific heat is defined by a fourth-order polynomial in temperature. The coefficients are determined by curve fitting tabulated data.

$$C_{P_i} = R\left(A_i + B_i T + C_i T^2 + D_i T^3 + E_i T^4\right) \qquad \textbf{2-56}$$

Using the species enthalpy, the species vibrational, rotational and translational energies and Equation [2-53], the total internal energy can then be found. If a perfect gas model is assumed then the vibrational energy is not present. The energies for translation, rotation and vibration used to calculate the species internal energies are found through the following equations. The equilibrium value for translational energy is given by

$$\widetilde{e}_{tr_i} = \widetilde{c}_{v_{tr_i}} T \qquad \textbf{2-57}$$

Where $\widetilde{c}_{v_{tr_i}} = 3/2R_i$. The equilibrium value for rotational energy is given by

$$\widetilde{e}_{rot_i} = \widetilde{c}_{v_{rot_i}} T \qquad \textbf{2-58}$$

Where $c_{v_{rot_i}} = \begin{cases} 0, for \cdot monatomic \cdot species \\ R_i, for \cdot diatomic \cdot and \cdot linear \cdot polyatomic \cdot moleclues \\ 3/2R_i, for \cdot non-linear \cdot polyatomic \cdot molecules \end{cases}$

Vibrational equilibrium can be assumed if the vibrational temperatures of the calculations are relatively lowed compared to the species vibrational temperatures. The equilibrium value for vibrational energy is given by

$$e^*_{vib_i} = \sum_{n=1}^{N_{\Theta,i}} \frac{R_i \Theta^{(n)}_{v,i}}{e^{\Theta^{(n)}_{v,i}/T} - 1} \qquad \textbf{2-59}$$

Where $N_{\Theta,i}$ is the number of characteristic temperatures of vibration, $\Theta_{v,i}$ for species i.

Chemistry Model

The reaction of gaseous hydrogen fuel with air is modeled using 9 species (H_2, O_2, H_2O, OH, H, O, HO_2, H_2O_2 and N_2) and 18 reactions[73] found in Table 2-1. The species N_2 is assumed to be inert in this model. The model was constructed by Drummond[73] and was chosen because it was already integrated into the CFD software. The model considers the multi-component diffusion and convection of important species, the finite-rate reaction of these species, and the resulting interaction between the fluid mechanics and chemistry[73]. The Drummond model has shown to be a viable model for mixing layers in a scramjet combustor and thus a good model choice for this research[74].

Table 2-1 Finite-Rate Chemistry Model and Arrhenius Rate Coefficients for Each Reaction[73]

Reaction Number	Reaction	Reaction Rate Variables		
		A	N	Activation Energy
1	H2 + O2 = OH + OH	0.1700E+14	0.00	48150
2	H + O2 = OH + O	0.1420E+15	0.00	16400
3	OH + H2 = H20 + H	0.3160E+08	1.80	3030
4	O + H2 = OH + H	0.2070E+15	0.00	13750
5	OH + OH = H2O + O	0.5500E+14	0.00	7000
6	H + OH = H2O + M	0.2210E+23	-2.00	0
7	H + H = H2 + M	0.6530E+18	-1.00	0
8	H + O2 = HO2 + M	0.3200E+19	-1.00	0
9	HO2 + OH = H2O + O2	0.5000E+14	0.00	1000
10	HO2 + H = H2 + O2	0.2530E+14	0.00	700
11	HO2 + H = OH + OH	0.1990E+15	0.00	1800
12	HO2 + O = OH + O2	0.5000E+14	0.00	1000
13	HO2 + HO2 = H2O2 + O2	0.1990E+13	0.00	0
14	HO2 + H2 = H2O2 + H	0.3010E+12	0.00	18700
15	H2O2 + OH = HO2 + H2O	0.1020E+14	0.00	1900
16	H2O2 + H = OH + H2O	0.5000E+15	0.00	10000
17	H2O2 + O = OH + HO2	0.1990E+14	0.00	5900
18	M + H2O2 = OH +OH	0.1210E+18	0.00	45500

The forward rate of each reaction j is a function of temperature given by the Arrhenius law using the values in Table 2-1.

$$k_{f_j} = A_j T^{N_j} \exp\left(\frac{-E_j}{RT}\right) \quad \textbf{2-60}$$

The production rates of each species can be determined using the law of mass action, Equation [2-57]. This requires the knowledge of the forward reaction rate, Equation [2-56], and the reverse reaction rate rate[73], $k_{bj} = k_{fj}/K_j$.

$$\sum_{i=1}^{N_s} \sigma'_{ji} C_i \frac{k_{f_j}}{k_{b_j}} \sum_{i=1}^{N_s} \sigma''_{ji} C_i \quad j=1,2,\ldots,N_R \quad \textbf{2-61}$$

Where the rate of change of concentration of species i by reaction j, C_i, is defined by[75]

$$\left(\dot{C}_i\right)_j = \left(\sigma''_{ji} - \sigma'_{ji}\right)\left[k_{f_j} \prod_{i=1}^{N_s} C_i^{\sigma'_{ji}} - k_{b_j} \prod_{i=1}^{N_s} C_i^{\sigma''_{ji}}\right] \quad \textbf{2-62}$$

The net range of change in concentration of species i by reaction j is then found by summing the contributions from each reaction,

$$\dot{C}_i = \sum_{j=1}^{N_R} \left(\dot{C}_i\right)_j \quad \textbf{2-63}$$

Now, the production of species i can be found using,

$$\dot{w}_i = \dot{C}_i (M)_i \quad \textbf{2-64}$$

Diffusion Models:

The Drummond model[73] includes models for coefficients governing the diffusion of momentum, energy and mass. The individual species viscosities are computed from Sutherland's law, and the mixture viscosity is determined from Wilke's law[73]. The thermal conductivities are also computed using Sutherland's law. The mixture thermal conductivity is computed using conductivity values for individual species and Wassilew's formula[76]. The diffusion velocities are found using the above parameters by solving[73]:

$$\vec{\nabla} X_i = \sum_{j=1}^{N_s} \left(\frac{X_i X_j}{D_{ij}} \right) \left(\vec{\tilde{V}}_j - \vec{\tilde{V}}_i \right) + \left(\alpha_i - x_i \right) \left(\frac{\vec{\nabla} P}{P} \right) + \left(\frac{\rho}{P} \right) \sum_{j=1}^{N_s} \alpha_i \alpha_j \left(\vec{b}_i - \vec{b}_j \right) + \sum_{j=1}^{N_s} \left(\frac{X_i X_j}{\rho D_{ij}} \right) \left(\frac{D_{Tj}}{\alpha_j} - \frac{D_{Ti}}{\alpha_i} \right) \left(\frac{\vec{\nabla} T}{T} \right)$$

2-65

If there are N_s chemical species, then i = 1, 2, . . .,(N_s-1) and (N_s-1) equations must be solved for the species f_i.

Chapter 3: Computational Domain and Boundary Conditions

Choosing the appropriate boundary condition for a surface is an important part in CFD modeling. The boundary conditions influence how the governing equations are solved and make each problem unique. The boundary conditions are applied to each surface of the computation grid.

The paradox involved in creating a computational grid is using discretized volumes small enough to resolve the flow physics while maintaining an overall number of cells that use time, memory and CPU efficiently. Large volume cells will be unable to accurately predict flow behavior on both large and small scales because of the distance with which information is passed. On the other hand, while small volumes are desirable, the computation time will be greatly increased as well as the CPU needed for calculations. Therefore, for the most effective computation grid, a balance between size and efficiency must be found.

This chapter describes the computational domain used to conduct the analysis of jets in a supersonic cross flow. The grids and associated boundary conditions for the different cases will be discussed. All grids were created using Gridgen v.15.2[77].

3.1 Boundary Conditions

3.1.1 Baseline Case Set-up

The computational domain for the Baseline, round-hole injector consists of a rectangular grid with an injector feed tube extending out of the bottom surface. Boundary conditions are applied to the inflow plane, outflow plane, far-field plane, bottom surface of the grid (representative of the tunnel floor), injector inflow plane and the injector walls. A schematic of the domain can be found in Figure 3.1.

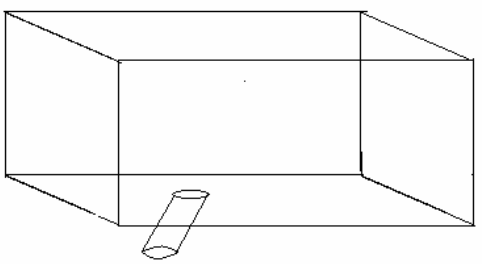

Figure 3.1 Baseline injector domain schematic.

Inflow Boundary Condition

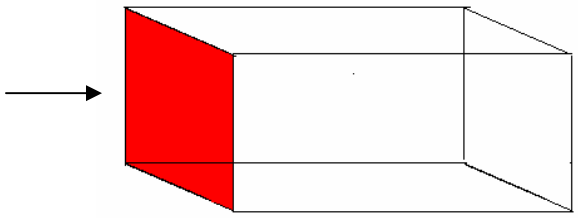

Figure 3.2 Inflow Boundary Condition

The CFD model mimics the Virginia Tech supersonic tunnel experimental setup. On the inflow boundary face, the boundary values are set according to the known air freestream conditions: a total pressure of 150 PSI and total temperature of 295 K. The tunnel approach flow creates a weak shock at a joint on the tunnel surface before the injectors are reached. The shock slows the approach flow from a nominal Mach 4 to Mach 3.7. As a result, Mach 3.7 is used in computing the inflow boundary conditions for the CFD model. The jet-to-freestream momentum flux ratio, $\overline{q}$, was set to 2.1. Note that $\overline{q}$ is defined by:

$$\overline{q} = \frac{(\rho u^2)_j}{(\rho u^2)_\infty} = \frac{(p\gamma M^2)_j}{(p\gamma M^2)_\infty} \qquad \textbf{3-1}$$

The remaining freestream quantities can be derived from the Mach number, temperature and pressure using the isentropic relations for perfect gas with γ=1.40 and the specific heat at constant volume, C_v, equal to 717.25 J Kg/K.

The inflow boundary is 12 jet diameters upstream of injection. At the point of injection, the boundary layer, $\delta_{o,}$ was measured to be 20 mm in the Virginia Tech tunnel which corresponds to a boundary layer height of 19.8 at the inflow boundary. The boundary layer height is measured from the Schlieren photograph taken during experimental testing. The turbulent velocity boundary layer profile was then calculated using the simple relationship:

$$\frac{U}{U_e} = \left(\frac{y}{\delta}\right)^{\frac{1}{7}} \qquad \textbf{3-2}$$

where U_e is the edge, or freestream, velocity. The boundary layer was added to the CFD software using a pointwise boundary. This sets values for velocity, density, pressure and turbulence quantities at each individual grid point in the inflow plane.

Outflow and Far-Field Boundaries

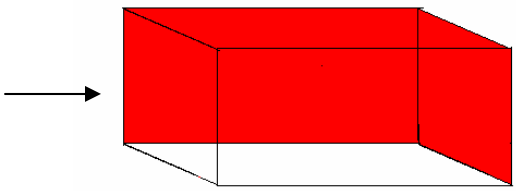

Figure 3.3 Outflow and Side Walls Boundary Condition

The outflow, sides and top surface of the computational domain do not represent physical surfaces. The side and top boundaries are each 12 effective jet diameters from the centerline and domain surface. This was assumed to be far enough from the jet as to not influence the physics of the jet plume interaction with the freestream flow. First-order extrapolation is applied to the outflow and side surfaces of the grid. Data are extrapolated from the conditions set at the boundary cells to the ghost cells. This results in a zero gradient at the boundary. The flow in the interior of the domain is supersonic, therefore no back pressure is necessary even though one is set. The outflow is 33 effective jet diameters downstream.

No-Slip, Adiabatic Wall Surface

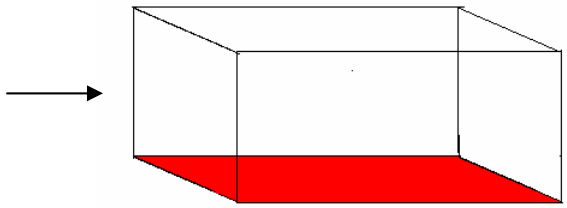

Figure 3.4 No-Slip Adiabatic Surface Boundary Condition, Tunnel Wall

The boundary condition applied to the surface of the domain to simulate the tunnel floor is a no-slip ($u=v=w=0$), adiabatic wall ($\delta T/\delta n=0$) condition. The no-slip, adiabatic condition is used for viscous flows on a solid wall boundary. The temperature gradient at the surface is set to zero by extrapolating the pressure and densities. The surface is assumed to be smooth. The no-slip, adiabatic wall boundary condition is applied to both the bottom surface of the domain and the injector feed-tube walls (Figure 3.5).

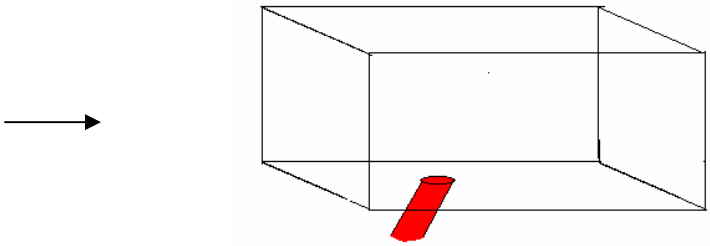

Figure 3.5 Injector Wall Boundary Conditions

Injector Inflow Conditions

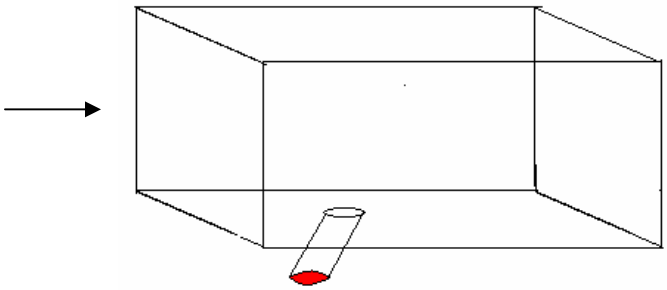

Figure 3.6 Injector Inflow Boundary Condition

The inflow of the injector was set to the known helium flow conditions: total pressure of 83 PSI and total temperature of 313 K. Helium was injected through the round orifice at Mach 1 and at a constant mass flow rate of 3.4 g/s and the entire flow at the fuel inflow boundary is assumed to be parallel to the walls of the injector. The Baseline injector is oriented 30° from the horizontal and therefore the flow-direction is also 30° from the horizontal.

The Baseline injector consists of a 3.226 mm diameter round-hole oriented at 30° to the horizontal. Figure 3.7 is the Baseline injector insert used in the experiments carried out in the Virginia Tech supersonic wind tunnel.

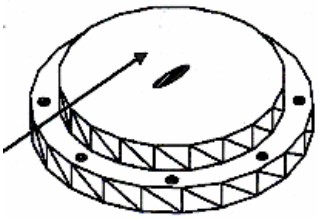

Figure 3.7 Baseline, single, circular injector insert.

3.1.2 Aeroramp Injector Set-up

The boundary conditions remain the same as for the Baseline case with the exception of the fuel inflow conditions. The four fuel injectors have separate boundary conditions. The pressure, temperature and Mach number are the same but the flow direction varied among the four injectors, details will be given below. The flow direction is calculated based on the toe-in angle and the injection angle of each injector. The combined mass flow rate through the four injector orifices totals the overall mass flow rate through the Baseline injector. For initial studies, the mass flow rate is assumed to be constant and equally divided through all four orifices. Sensitivity studies to variations in mass flow through the injectors are conducted by varying the mass flow through the front and rear sets of injectors. The total mass flow was kept constant through the studies. For the first mass flow variation study, twice as much mass flow was injected through the front injectors than the rear injectors. The opposite was performed for the second study.

Figure 3.8 is the aeroramp injector insert used in the experiments carried out in the Virginia Tech supersonic wind tunnel. The aeroramp consisted of four injectors arranged in a two-two configuration. The front two injectors were angled 15° towards the centerline and injection occurred at 20° (Figure 3.9) to the horizontal. The rear set of injectors were toed-in 30° towards the centerline and had a 40° injection angle. The injectors were spaced 2 equivalent diameters apart laterally and 4 equivalent diameters apart in the streamwise direction. The equivalent diameter of the aeroramp injector is defined by

$$d_{eq} = \left(\frac{4A_j}{\pi} \right)^{1/2} \qquad \textbf{3-3}$$

Where Aj is the area of each injector orifice. The equivalent diameter is equal to the diameter of the Baseline injector, 3.23 mm. The four injector aeroramp configuration was created by Jacobsen[33] for a Mach 2.4 flow with a hydrocarbon fuel.

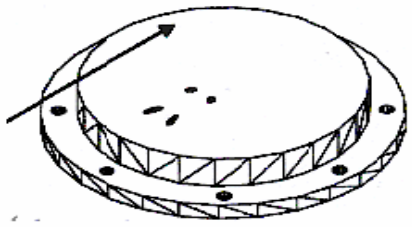

Figure 3.8 Aeroramp configuration and wind tunnel model insert

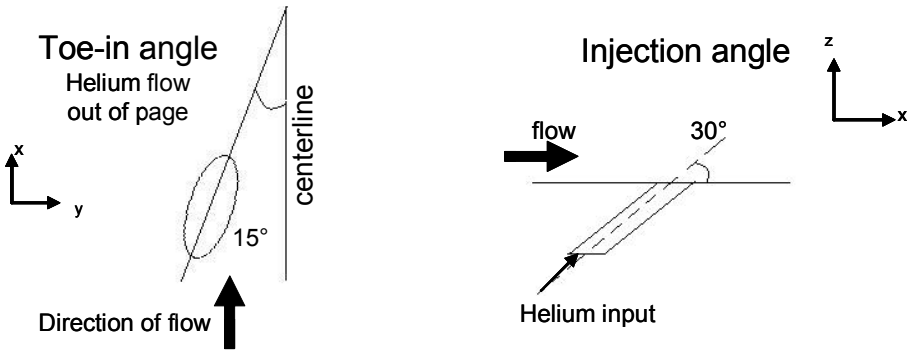

Figure 3.9 Defined angles of injectors

3.1.3 Aligned Diamond Injector Set-up

The boundary conditions remain the same as for the Baseline case with the exception of the fuel inflow boundary condition. The diamond injector is angled 60° to the horizontal so that the fuel is injected at 60° to the horizontal. The fuel inflow pressure of the diamond injector is lower than the fuel inflow pressure of the Baseline injector. The inflow boundary of the injector is set to the known helium conditions: total pressure of 45 PSI and total temperature of 313 K. Helium is injected at Mach 1 and a mass flow rate of 3.4 g/s. The mass flow rate was consistent with the Baseline injector mass flow rate. To achieve this mass flow, the jet to freestream total pressure ratio was 0.30 resulting in an effective radius of R_b = 3.87 mm and a jet-to-free stream momentum flux ratio of q= 1.2. A lower q is desirable for the diamond because if q becomes too high, the jet can rapidly plume outward losing the diamond shape and its benefits[78].

Figure 3.10 pictures the injector wind tunnel model insert. The diamond injector had a long dimension of 12.7 mm and a short dimension of 2.25 mm. The overall area of the diamond shaped injector is larger than the area of the Baseline injector and the effective area of the aeroramp injector. The larger area compensates for the lower pressure produced by the diamond shaped orifice. The injector was oriented 60° from the horizontal (tunnel test section floor). The 60° angle was chosen in an attempt to maximize penetration[79].

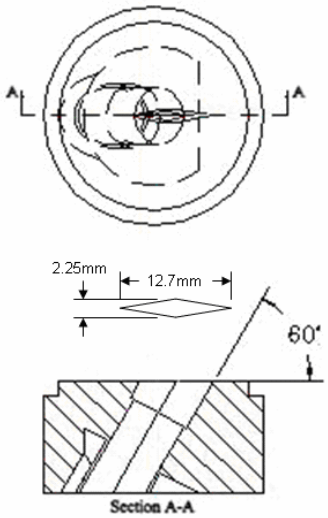

Figure 3.10 Diamond injector tunnel inserts

3.1.4 Yawed Diamond Injector Set-up

The boundary conditions for the yawed diamond injector are the same as for the Baseline case with the exception of the fuel inflow. The fuel is injected at 60° to the horizontal and at a 15° yaw angle. The yawed diamond is similar to the aligned diamond with the exception of the yaw angle. The yawed diamond had the same dimensions as the aligned diamond, 12.7 mm long and 2.25 mm wide with the long side at a 15° yaw. The fuel inflow conditions are the same as the fuel inflow for the aligned diamond injector above. The yawed diamond configuration used in the experiments at Virginia Tech in the supersonic wind tunnel can be found in Figure 3.11.

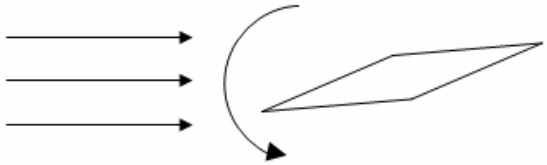

Figure 3.11 Schematic of the 15 degree yawed diamond configuration[79]

3.1.5 Shock Impingement Set-up

To simulate the oblique shock, the inflow boundary condition on the Baseline injector grid was modified. The shock generator used in the experiment created a shock of 20°. Figure 3.12 is a pictorial description of the changes to the Baseline grid to generate an oblique shock wave. The shock is designed to impact the grid at three locations: 2 effective diameters, 8 effective diameters and 16 effective diameters downstream of the injection point. From this, a vertical location is determined where the shock passes through the inflow plane. The flow properties calculated behind the shock of 20° with Mach 3.7 flow upstream were used as the boundary condition at the inflow plane above the point where the shock passed through the plane. The following conditions were used behind the shock: total pressure of 147 PSI, total temperature of 294 K and Mach number of 3.3146. The conditions below the shock are the same as found in the Baseline inflow conditions.

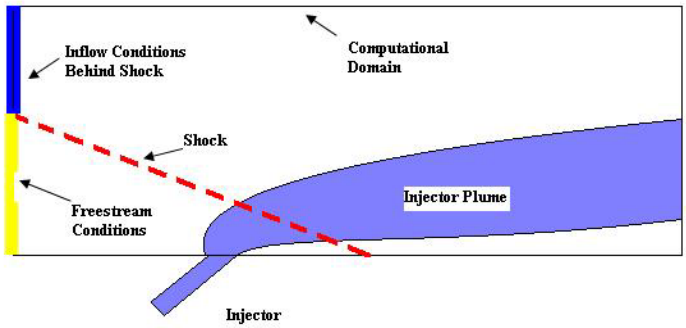

Figure 3.12 Inflow boundary condition change to induce a shock that intersects with the injectant plume.

The remaining boundary conditions for the shock impingement cases are the same as the Baseline case. The far-field boundary condition on the exterior walls allows the reflected shock to escape the domain.

3.1.6 Hydrogen Cases Set-up

The non-reacting, reacting hydrogen cases use the same grid as the Baseline case but with different inflow conditions for both the air inflow and the fuel inflow. The conditions are set to simulate the flow in the LENS[80] test facility in Niagara Falls, NY which uses hydrogen instead of helium as the injected fuel. The shock tube facility freestream conditions are set for a Mach 4 flow at a total pressure of 3,492 PSI and a total temperature of 4620 K. The hydrogen fuel inflow conditions are known and set for sonic injection at a total pressure of 1460 PSI and a total temperature of 611 K. The remaining boundary conditions are set to match the Baseline case boundary conditions.

3.2 Computational Grids

The multi-block structured grids generated were created using Gridgen[77] version 15.2. GASP requires a structured grid to be imported using the Plot3D format. The final grids that were used in the computational analysis presented in this research are defined in more detail below. Each grid was designed to have a small initial spacing as well as at least 40 nodes in the boundary layer in order to resolve the boundary layer gradients. The

grids were extruded from the wall using a hyperbolic tangent formula with the specified initial spacing. The formula increased the grid spacing more efficiently than a linear stepping formula would. The initial spacing for the grid in the boundary layer on the square cylinders was determined using the following formula:

$$\Delta y = \frac{0.7L}{\sqrt{\mathrm{Re}_L}} \qquad \textbf{3-4}$$

The spacing accuracy can be verified by calculating $y^+ \equiv \frac{yu^*}{\nu}$. A spacing of y^+ less than unity was calculated for all configurations, which is an acceptable value when used with the SST turbulence model.

The turbulence intensity was assumed to be 5% initially. The turbulence level inside the Virginia Tech Wind Tunnel was not known at the time the simulations were conducted. A studied conducted later varied the turbulence intensity to 15%, and those results are shown in Chapter 5. The turbulent length scale was assumed to be the same order of magnitude as the initial grid spacing. The turbulent kinetic energy and turbulent dissipation were determined (in GASP) from the specified turbulence quantities.

After the final grids were imported into GASP, they were sequenced within GASP. Sequencing removes every other grid point from the original (fine) grid. Sequencing develops the flow quicker but trades accuracy. Once the flow is developed, the finer grid is used and accuracy is obtained. Sequencing can increase the rate of convergence by solving on coarser grids to allow a problem to set up and then solving on the fine grid for accuracy. Using sequenced grids decreases the time and CPU needed. Sequencing can also be used to verify grid convergence.

Two different grid generation approaches were taken in the designs of the Baseline and aeroramp grids. Initially, a grid was constructed to maximize the cell clustering near the injector and flow-field of interest while decreasing the necessary cells in the far-field. This technique took the fine grid surrounding the injector and extruded the mesh along the fuel flow-path to the outflow plane of the domain. The second approach involved more cells across the entire domain with less control on grid clustering. The second technique created a Cartesian, H-type grid with minimal skew in

the cells. The original approach will be described and then the final grids used for each the analysis will be discussed in detail.

The first grid generation approach was taken only for the Baseline and aeroramp injectors. Further explanation will be given on why other grids were created with the second approach. The Baseline injector, original, grid can be found in Figure 3.13. The grid surrounding the injector pictured on the right is extruded from the bottom face of the domain to the outflow plane. This creates an arc similar to the actual flow-path of the injected fuel into the freestream. The original Baseline injector grid had 1.8 million cells, modeled without a symmetry plane and the domain was sequenced once to a coarser grid.

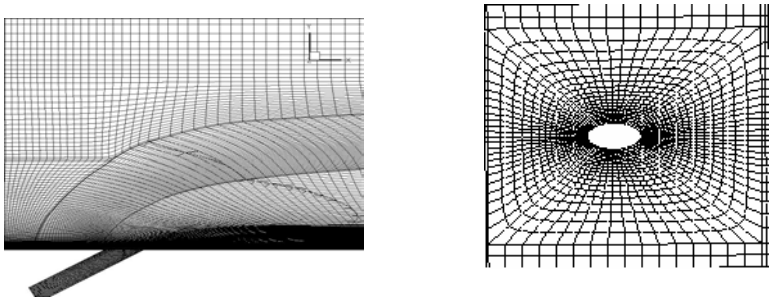

(a) Side-view (x-z plane) **(b) Bird's eye view of injector (x-y plane)**

Figure 3.13 Grid generation first approach for the Baseline injector.

The aeroramp grid was created in a similar manner and can be found in Figure 3.14. A side-view of the grid domain is picture on the left with flow left to right. The grid generated around the injectors, pictured on the right, is turned and extruded through the domain. The aeroramp was modeled with a symmetry plane, therefore only two of the four injectors were directly modeled. The grid around the front injector was interfaced with the grid around the rear injector through a chimera surface. The chimera surface was designed to mate two surfaces with different mesh designs. These surfaces iterate the solution between the adjacent cells. The original aeroramp grid had 1.2 million cells and was sequenced twice creating medium and coarse grids. Each sequence was run until convergence was achieved.

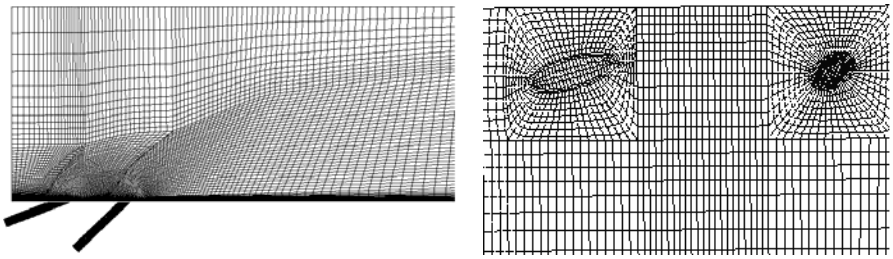

(a) Side-view (x-z plane) **(b) Bird's eye view of injector (x-y plane)**

Figure 3.14 Grid Generation first approach for the aeroramp injector.

The need to create a second grid for each injector arose from the distorted numerical predictions produced by the aeroramp grid. Figure 3.15 and Figure 3.16 plot mass fraction contours for the aeroramp injector at two different downstream locations with and without the grid overlaid. The influence of the grid design can be seen in the boundaries of the extruded face. The largest influence can be seen in Figure 3.16 at +/- 2 diameters from the centerline. The Baseline injector did not show the same strong influence of the grid as the aeroramp injector. Since the grid was shown to influence the solution, a strictly Cartesian grid was generated. For consistency, the Baseline injector grid was modified as well. The individual meshes used for each injector configuration are discussed in detail below.

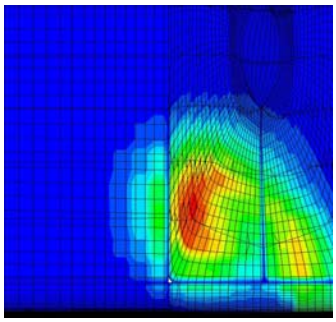

Figure 3.15 Mass fraction contour with overlaid grid for half of a crossplane (y-z plane) at $x/d_{eff} = 6$ for the aeroramp injector

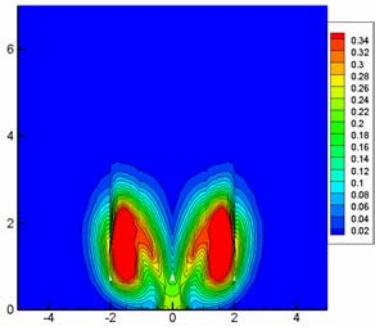

Figure 3.16 Mass Fraction contour for entire crossplane (y-z) at $x/d_{eff} = 6$ for the aeroramp injector

3.2.1 Baseline Injector Case

The final grid for the Baseline case had approximately 1.49 million cells with an initial Δy of $3x10^{-6}$m. A fine grid of 5.94 million cells and a coarser grid of 0.375 million cells was also studied for grid size sensitivity. The grid size is important in numerical modeling because if the spacing between nodes is too large, any physics occurring in between the cells is lost and the result is a prediction that does not capture the actual behavior of the flow. Figure 3.17 plots five different parameters that are focused on in the results section of this research. The plume size is defined by the plume width, $y\pm$, the plume maximum height, z_{max}, and the plume center of mass, z^{+}. The size parameters are plotted on the first vertical axes as normalized distances. The mixing characteristics of the plume were defined by the maximum fuel concentration, σ_{max} and the mixing efficiency parameter, η_m. The mixing parameters are plotted on the second vertical axes and are non-dimensional quantities. All parameters were measured at a single cross-plane downstream of injection. Each of these will be explained more thoroughly when the results are presented since the exact definitions are not needed for the grid size studies. Figure 3.17 shows that the largest changes in value for all of the studied parameters occur between the coarse and medium grids. There was minimal variation, if any, between the fine and medium grids. As a result, the medium grid refinement was assumed to be fine enough to capture the physics. The medium grid was also used for the shock-impingement studies and the hydrogen reacting/non-reacting studies.

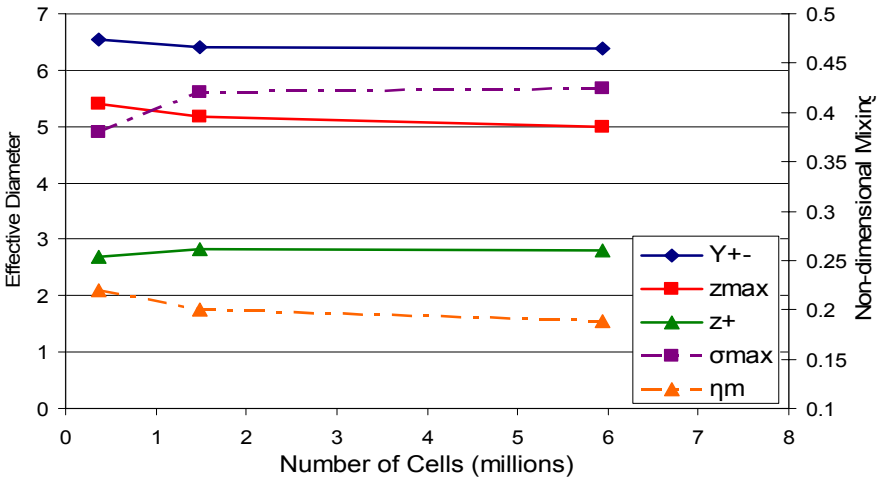

Figure 3.17 Grid size sensitivity study for the Baseline injector

The grids cells were clustered in the near-wall and shock regions in order to capture the boundary layer and steep gradients. An isometric view of the grid can be seen in Figure 3.18. The symmetry plane with a mesh extended into the injector feedstock is shown in Figure 3.19. Lastly, concentrated views of each plane can be found in Figure 3.20. The mesh in and surrounding the injector is extruded vertically to the top surface of the domain. The cross-plane, y-z, and side-view plane, x-z, are orthogonal and were designed to minimize element skew.

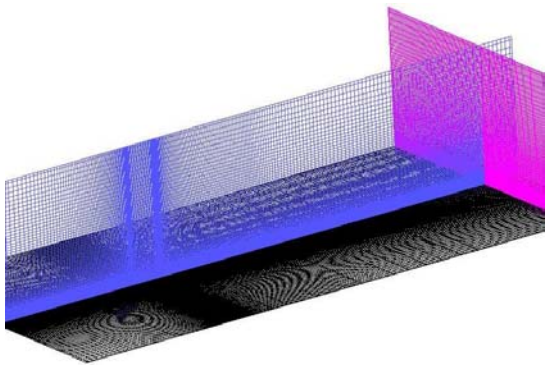

Figure 3.18 Iso-view of the grid topology with slices in all three planes. Black is the x-y plane, pink is the y-z plane and the blue is the x-z plane. The flow is going left to right.

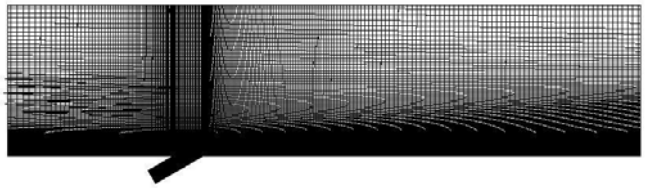

Figure 3.19 A slice in the x-z plane at y = 0 (the centerline) of the grid topology. The flow is going left to right.

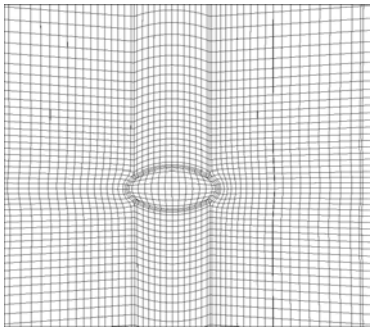

(a) Bird's eye view (x-y plane)

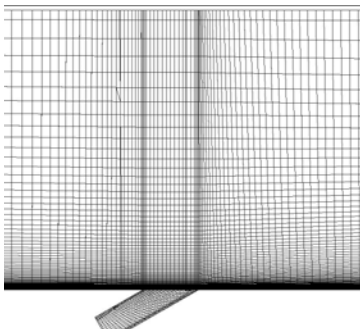

(b) Side-view (x-z plane)

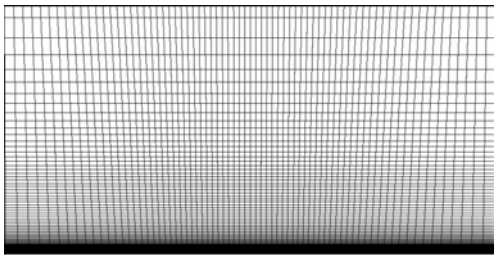

(c) Cross-plane (y-z plane)

Figure 3.20 2-D plane views of the Baseline grid.

The residual error for the momentum and turbulence equations and the mass balance were monitored over the course of the CFD analysis for convergence. Figure 3.21 and Figure 3.22 plot the residual convergence for the Baseline injector. Figure 3.22 plots the mass flow rate of helium in the outflow plane of the grid.

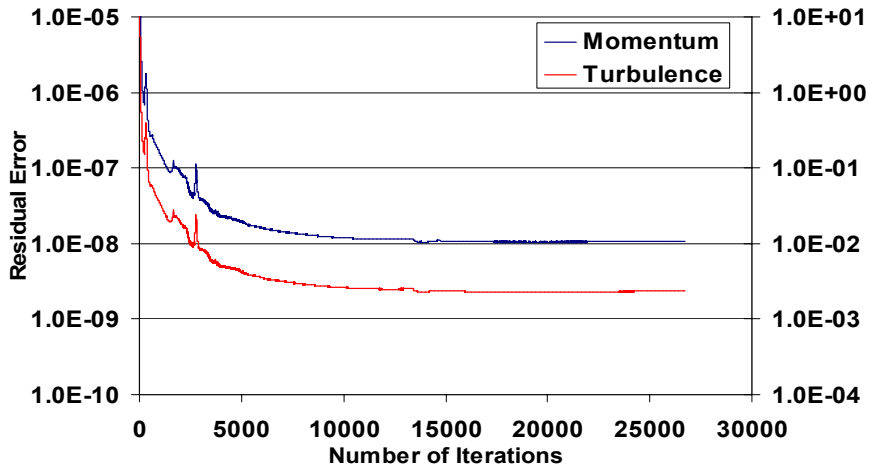

Figure 3.21 Baseline injector residual error convergence

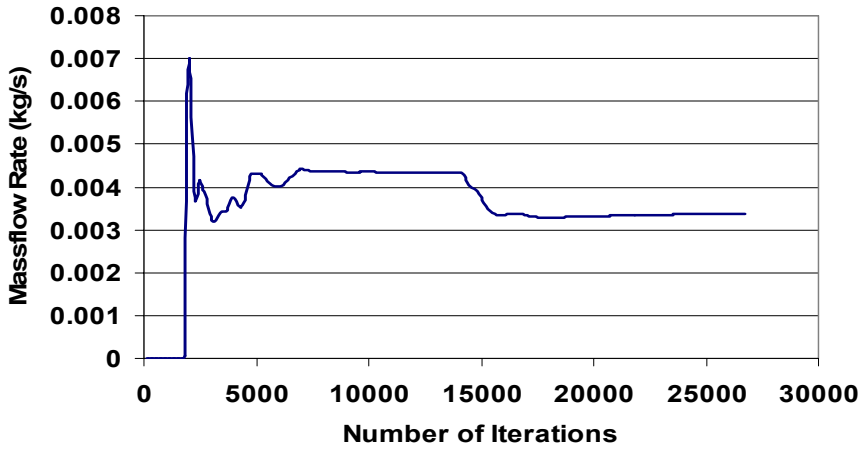

Figure 3.22 Baseline injector mass flow rate convergence

3.2.2 Aeroramp Injector Case

The structured grid used for the aeroramp injector configuration consisted of 1.27 million cells with an initial Δy of $3x10^{-6}$. An additional fine grid of 5.08 million cells and a coarse grid of 0.320 million cells were analyzed for grid size sensitivity. Figure 3.23 plots the values of five different parameters at the same downstream location for different grid refinement of the aeroramp grid. The same trend found with the Baseline grid study is found here, the largest changes for all parameters studied occurred between the coarse and medium grids. It was concluded that the medium aeroramp grid of 1.27 million cells is sufficient to capture the flow-field.

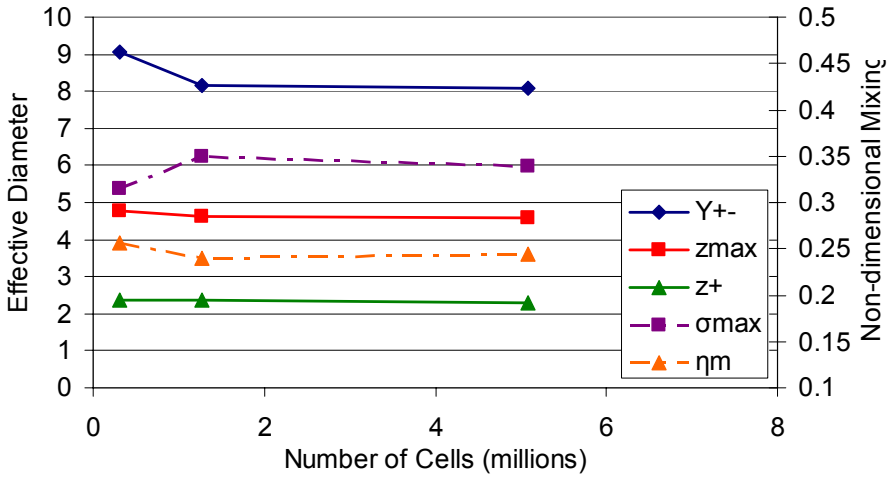

Figure 3.23 Grid size sensitivity study for the Aeroramp injector

The grid was clustered in the near-wall and shock regions in order to capture the boundary layer and steep gradients. The bottom surface of the grid around the four injectors, a side view, x-z plane, centered on the injector feed stocks and a cross-plane slice can be found in Figure 3.24. The mesh created on the bottom surface was extruded vertically to the top boundary of the domain. The mesh was not mapped to the outflow to mimic the flow field like the previous mesh mentioned earlier. The change in grid generation approach produced results that were independent of the mesh and boundary structure.

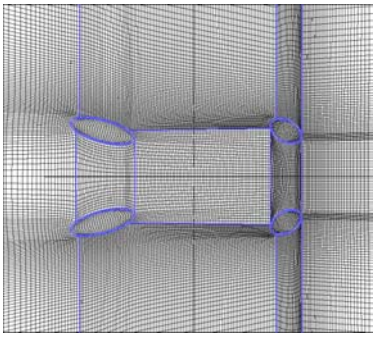

(a) Bird's eye view (x-y plane)

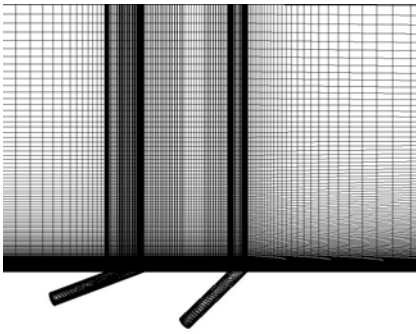

(b) Side-view (x-z plane)

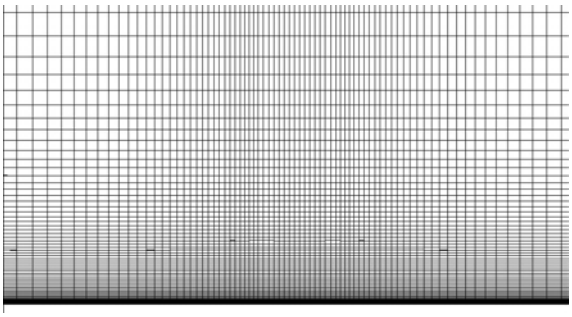

(c) Cross-plane view (y-z plane)

Figure 3.24 2D plane views of the aeroramp injector grid.

Convergence for the aeroramp injector was monitored through the analysis and can be found in Figure 3.25 and Figure 3.26. Figure 3.25 plots the momentum and turbulence residual errors and Figure 3.26 plots the mass flow rate of helium in the outflow plane.

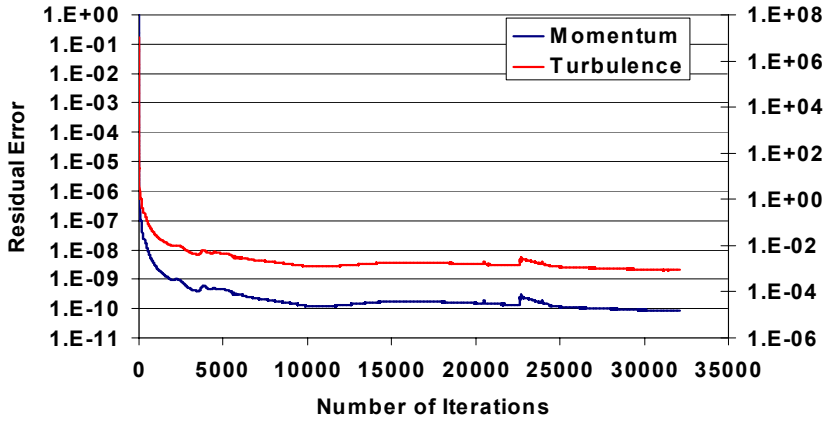

Figure 3.25 Aeroramp injector residual error convergence criteria

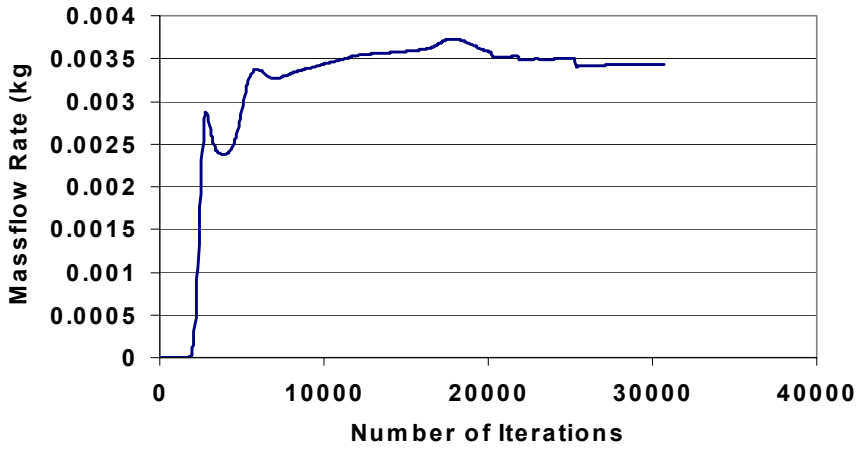

Figure 3.26 Aeroramp injector mass flow rate convergence

3.2.3 Aligned Diamond Injector Case

The aligned diamond injector grid consisted of 1.5 million cells with clustering in the boundary layer and areas of high gradients. A fine grid of 6.06 million cells was also studied to show grid size sensitivity. Figure 3.27 plots five different parameters studied in this research for the two different grid sizes. The parameters were taken in a single plane downstream of injection. The majority of the parameters hardly changed magnitude with grid refinement. The differences were considered small and the grid of 1.5 million cells was assumed sufficient to capture the flow-field. An even coarser grid was not studied because of time constraints and it was concluded that the results of the Baseline and aeroramp grids were sufficient to show that a coarser grid would adversely affect the accuracy of the solution.

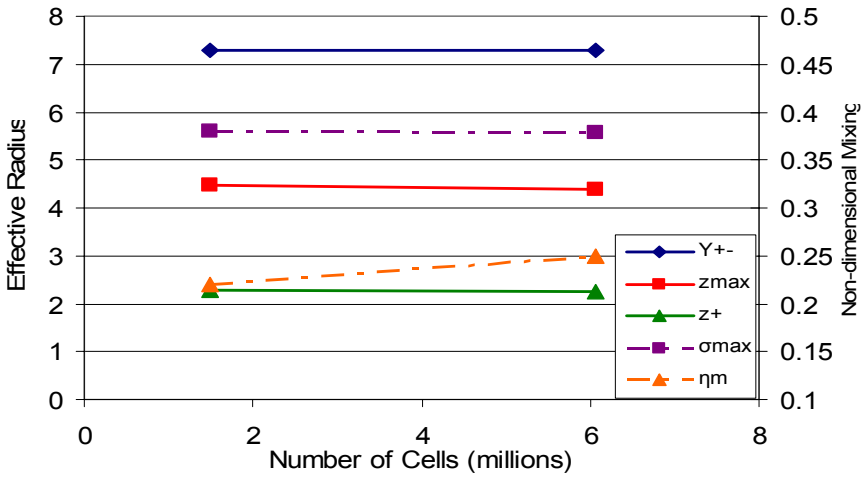

Figure 3.27 Grid size sensitivity study for the diamond injector

The structured grid used for the diamond injector configuration had an initial Δy of $3x10^{-6}$. The grid inside and surrounding the diamond is pictured in Figure 3.28. Also shown in Figure 3.28 is a side view centered on the injector feed stock and a slice in the y-z cross-plane. The mesh was kept as orthogonal as possible to minimize cell skew.

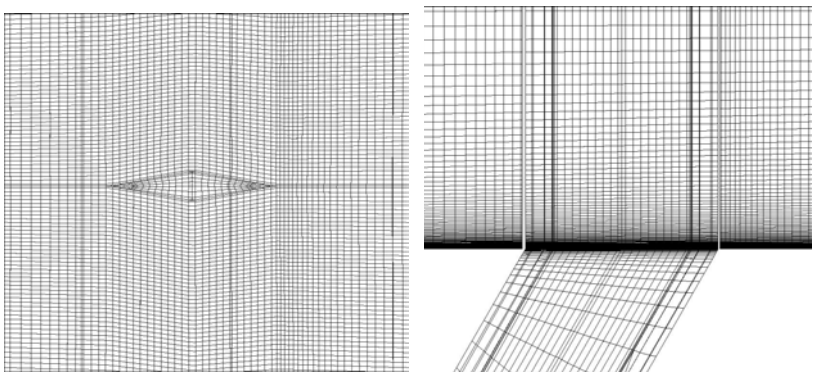

(a) Bird's eye view (x-y plane) **(b) Side-view (x-z plane)**

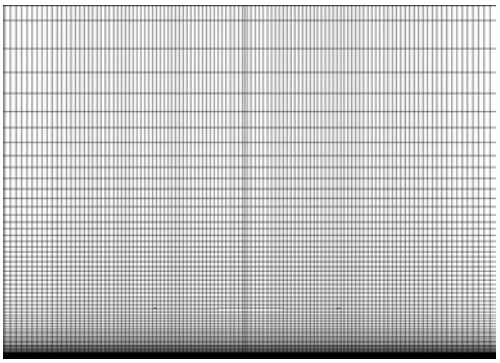

(c) Cross-plane view (y-z plane)

Figure 3.28 2D plane views of the aligned diamond injector grid.

The convergence for the aligned diamond injector can be found in Figure 3.29 Figure 3.30. The momentum and turbulence residual errors and the mass flow rate of helium in the outflow plane were used as convergence criteria.

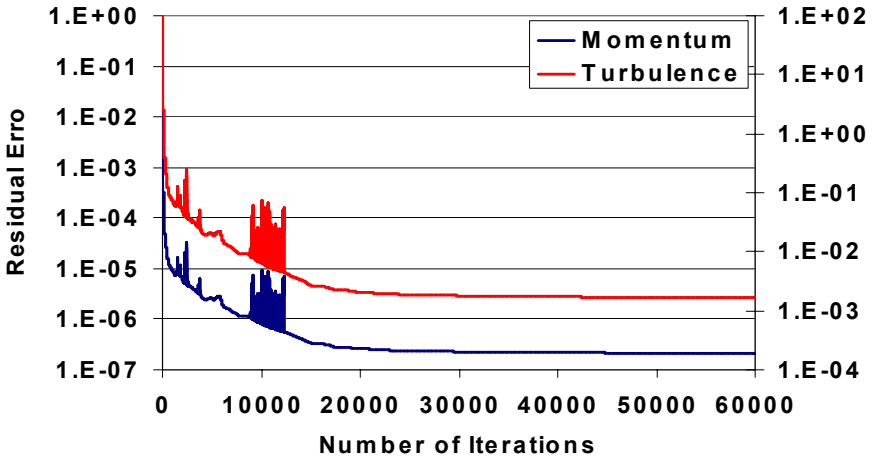

Figure 3.29 Diamond Injector residual error convergence

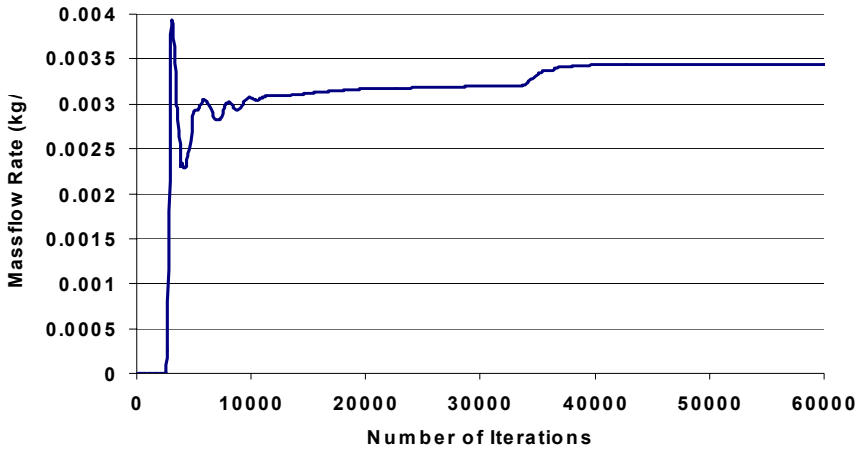

Figure 3.30 Diamond injector mass flow rate convergence

3.2.4 Yawed Diamond Injector Case

The yawed diamond injector grid consisted of 1.8 million cells with an initial Δy of $3x10^{-6}$. A grid sensitivity study was not performed for the yawed diamond injector case because the three previous grid studies for the Baseline, aeroramp and diamond injectors were considered sufficient to provide the necessary order of magnitude for the grid size. The yawed diamond injector grid was created using the three previous grids, especially the diamond injector grid as guidelines.

The yawed diamond injector has a similar y-z cross-plane and side view to the aligned diamond injector in Figure 3.28. The mesh in and surrounding the yawed diamond injector is shown in Figure 3.31. This mesh is extruded vertically to the top surface of the domain.

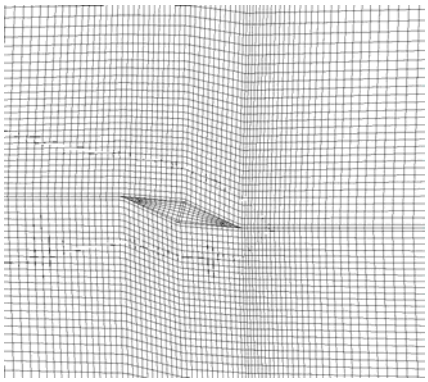

Figure 3.31 2D plane view of the yawed diamond injector (x-y plane).

Figure 3.32 and Figure 3.33 are plots of the convergence criteria used for the yawed diamond injector. The momentum and turbulence residual errors and the mass flow rate of helium out of the exit plane were used to monitor convergence. The noise in the convergence plots are a result of the yawing the diamond and creating shock unsteadiness in the flow.

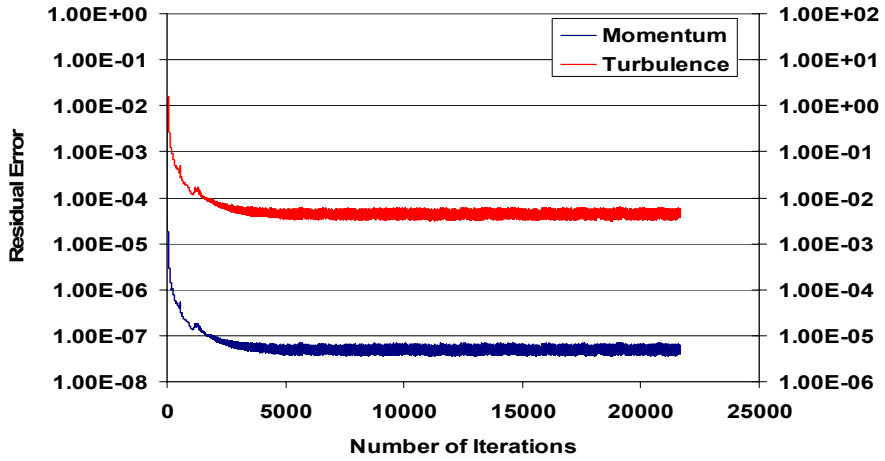

Figure 3.32 Yawed diamond residual error convergence

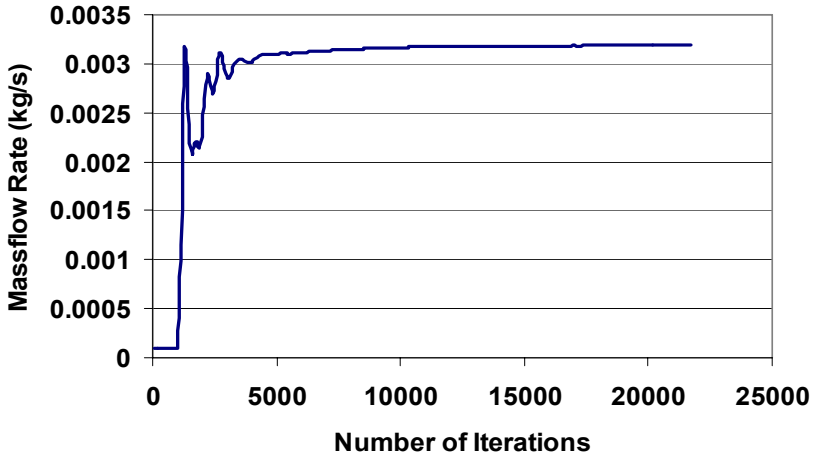

Figure 3.33 Yawed diamond mass flow rate convergence

3.2.5 Shock Impingement Cases

The grid used for the Baseline case analysis was also used for the shock impingement cases. The only modifications to the set up of the numerical model and grid were in the boundary conditions mentioned earlier. A grid study was performed and the

results were shown in the Baseline case section. The residual error convergence plots for the three shock cases can be found in Figure 3.34, Figure 3.35 and Figure 3.36.

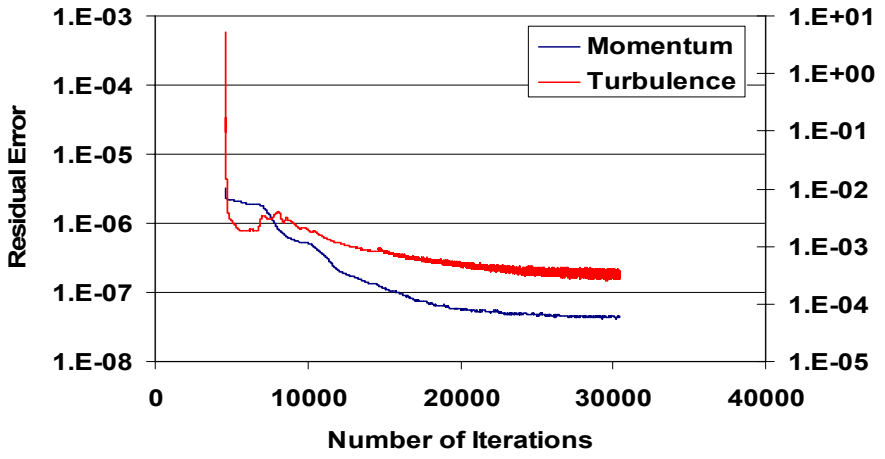

Figure 3.34 Shock case 1 residual error convergence

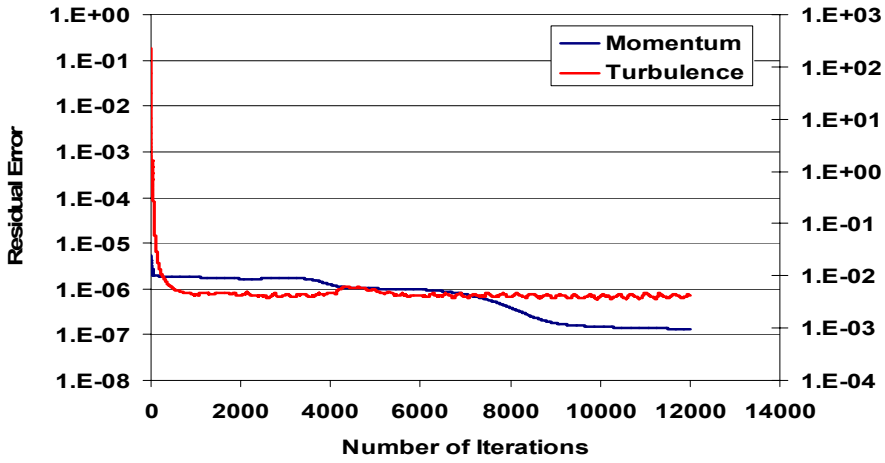

Figure 3.35 Shock case 2 residual error convergence

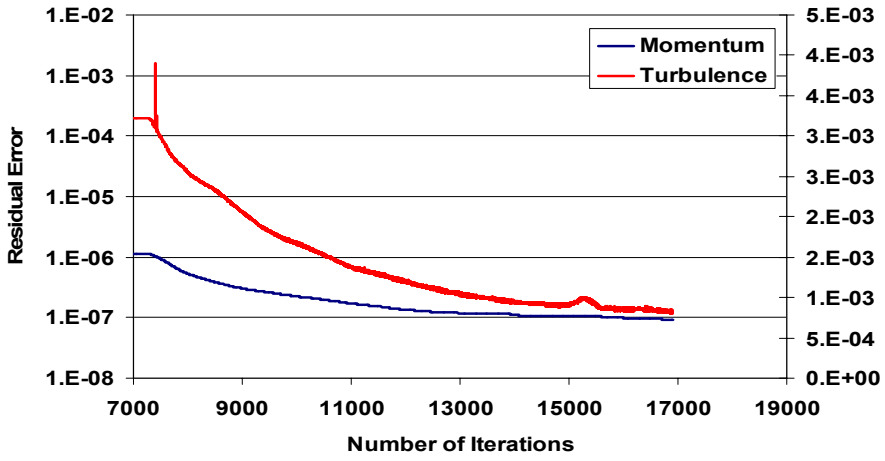

Figure 3.36 Shock case 3 residual error convergence

3.2.6 Hydrogen Case

The hydrogen reacting and non-reacting analyses use the same grid that was used for the Baseline case analysis. Since the purpose of the hydrogen studies was to analyze the ability of a non-reacting analysis to predict the mixing behavior of the reacting analysis, the injector design and computational grid were not the main focus and therefore kept simple and consistent. In addition, a grid study was already performed. The residual error convergence and hydrogen mass flow rate convergence in the outflow plane can be found in Figure 3.37 and Figure 3.38.

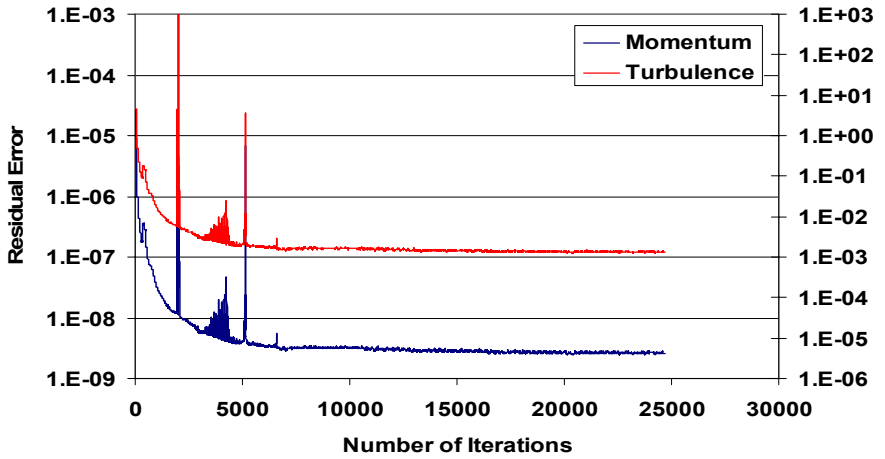

Figure 3.37 Hydrogen residual error convergence

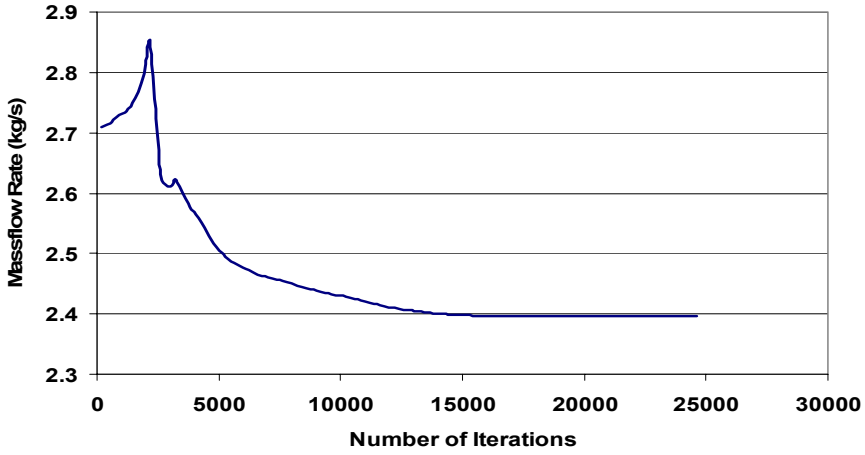

Figure 3.38 Hydrogen mass flow rate convergence

Chapter 4: Experimental Setup and Results Used for Comparison and Validation

This chapter briefly describes the experiments carried out in the supersonic wind tunnel at Virginia Tech which were used for validation of the CFD predictions. The Baseline configuration, aeroramp configuration and shock impingement studies were conducted by Luca Maddalena[81,82]. The diamond configuration tests were conducted by Peter Grossman[79]. This section is a summary of their test set-up and data reduction. Complete details can be found in those references.

4.1 Test Facilities and Equipment

Experiments were conducted in the Virginia Polytechnic Institute and State University unheated, blow-down supersonic wind tunnel with test section measuring 23 cm wide by 23 cm high and 30 cm long in the streamwise direction. A schematic of the wind tunnel nozzle and test section is shown in Figure 4.1. The tunnel was configured with a convergent-divergent nozzle resulting in a nominal freestream Mach number of 4.

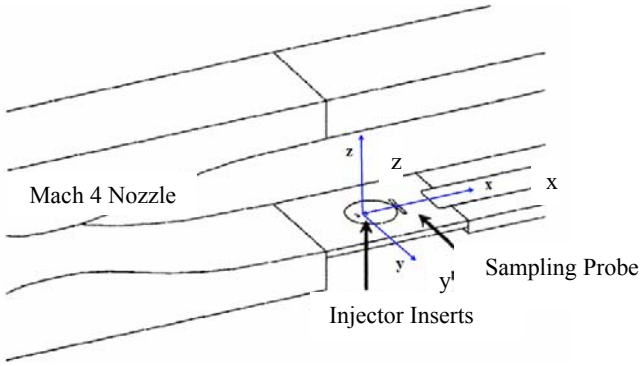

Figure 4.1 Virginia Tech test section setup

A two-dimensional shock generator, Figure 4.2, was used to produce a shock of 20° which was impinged upon the jet at three stations downstream of the injection point, 2, 8 and 16 effective diameters. Detailed measurement of the flow-field and concentration

were made with greatest emphasis on the region of shock wave/ boundary layer/ jet interaction.

Figure 4.2. Photograph of the Test section with the Shock Generator and Concentration Probe

4.2 Experimental Methods

4.2.1 Test Matrix

All wind tunnel tests were performed at a nominal free-stream Mach number of 4.0. Free stream conditions were fixed at a total pressure of 1034 kPa with an ambient mean total temperature of approximately 295 K, producing a freestream Reynolds number of 5.7e+7 per meter. These conditions resulted in a turbulent boundary layer with a thickness of approximately 20 mm at the point of injection. Heated helium was used as the injectant to simulate hydrogen fuel. The injectant was heated to an average total temperature of 313K and the average injection Mach number was sonic. The injected mass flow rate, G_j, was set to 3.4 g/s.

A Cartesian coordinate system was chosen with the origin on the wall surface along the test section centerline, as shown in Figure 4.3. The origin of the coordinate system is located on the wall in the middle of the injector array or single injector.

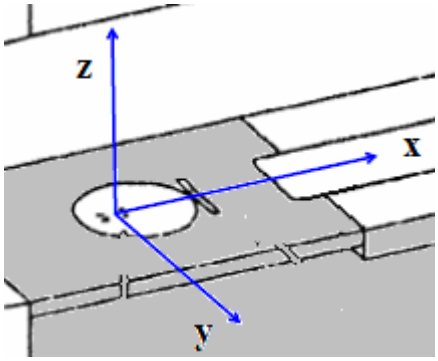

Figure 4.3 Cartesian Coordinate system

The positive x-axis is in the free stream direction, the positive z-axis is in the vertical direction perpendicular to the wall, and the y-axis spans the test section. All lengths besides the diamond injector configurations are normalized by the effective diameter, d_{eff}, defined as

$$d_{eff} = C_d^{1/2} d_{eq} \qquad \textbf{4-1}$$

where C_d is the injector discharge coefficient and d_{eq} is the equivalent jet diameter. The measured injector discharge coefficients were 0.88 for the Baseline single-hole injector and 0.83 for the aeroramp. The equivalent jet diameter is defined as the diameter of a single circular orifice having the same area as the combined area of all four orifices. The diamond configurations and the Baseline injector when compared to the diamond injectors were normalized by the effective radius, R_b, defined[78]

$$R_b = \sqrt{\frac{G_j}{\rho_\infty u\infty}} \qquad \textbf{4-2}$$

where G_j is the mass flow rate and ρ_∞ is the freestream density and u_∞ is the freestream velocity.

4.2.2 Aero-thermodynamic Probing

Aero-thermodynamic probing was accomplished by means of Pitot, cone-static and total temperature probes. The uncertainty on pressure measurement was evaluated to be ±0.06 atm.

Total temperature was measured with a rake consisting of three probes. The total temperature probes also had 4 small ports to improve the recovery factor. The ratio of capture to recovery area was 5 to 1 resulting in a recovery factor 0.97. The uncertainty on temperature measurement was evaluated to be ±2K.

4.2.3 Species Compositions Measurements

Mean species concentration measurements were obtained using an integrated sampling probe and gas analyzer designed specifically for use in supersonic flow. The fundamental concepts and design of this probe were developed at Virginia Tech by Prof. W. Ng and his students[83]. The concentration probe is an aspirating type attached to a vacuum pump. The unit consists of a constant temperature hot-film sensor operating in a channel with a choked exit. The probe is designed with a diverging channel between the tip and the sensor plane. The inlet hole at the tip of the probe has the same diameter as the choked orifice. These diameters are chosen so as to preclude the occurrence of a standoff shock at the probe tip. Flow visualization from spark Schlieren verified this design intention. The concentration probe was calibrated to measure the helium molar fraction uniquely related to a given pressure, temperature and rate of heat transfer sensed at the hot-film operating plane. The absolute measurement uncertainty in helium mass fraction was estimated to be approximately ±7%.

For the present investigation, the probe was inserted through the tunnel floor and mounted onto a traversing system. Between each run, the probe span-wise location was adjusted manually. There were 11 span-wise measurement locations. Data reduction methods are discussed in References 79, 81 and 82.

Chapter 5: Baseline Injector Predictions

5.1 Overview

In this section, numerical predictions for the Baseline, round injector are presented. Experimental data for this case have been collected as was discussed in Chapter 4. Flow-field visualization contours, mixing efficiency, total pressure losses and plume size will be used to compare the experimental results with the CFD predictions. Each of these types of results will be discussed before the results themselves are presented. Sensitivity studies were also conducted for the turbulent Prandtl number, turbulent Schmidt number, turbulence intensity, incoming boundary layer height and CFD software tools. The best prediction is used for future comparisons.

5.1.1 Integrated Parameters

The following were used to characterize the fuel-air plume, total pressure loss parameter, mixing efficiency parameter and plume size characteristics. These quantities are used in Chapter 5 and Chapter 6.

5.1.1.1 Total Pressure Loss Parameter

The overall total pressure losses are quantified using the overall total pressure loss parameter, which involves numerical integration of the mass-weighted total pressure field over a specified cross-plane area. The overall total pressure recovery, $P_{t,rec}$,used to determine the total pressure loss parameter is defined as[21]

$$P_{t,rec} = \frac{\int \rho u P_t dA}{\int \rho_\infty u_\infty P_{t,\infty} dA + \rho_j u_j P_{t,j} A_j} \qquad \textbf{5-1}$$

The total pressure loss parameter is defined as follows, $\Pi = 1 - P_{t,rec}$. A parameter value of $\Pi = 0$ indicates no total pressure loss and $\Pi = 1$ indicates complete total pressure loss.

5.1.1.2 Mixing Efficiency Parameter

In a non-reacting simulation of a supersonic combustor, it is useful to know the mixing efficiency of the injection process. This is intended to surmise how well the fuel would burn in an actual scramjet combustor with the same pressure field. The mixing efficiency, η_m, is the total mass of fuel which would react assuming steady, isentropic, quasi 1-D flow divided by the total mass flow rate of fuel. This is given by [84]

$$\eta_m = \frac{\int \rho u Z dA}{\int \rho u \alpha dA} \qquad \textbf{5-2}$$

Where $Z = \alpha$, if $\alpha \leq f$ (H_2 lean – all H_2 consumed) or $Z = (1-\alpha) f / (1-f)$ if $\alpha > f$ (O_2 lean – all O_2 consumed). Note that f is the stoichiometric hydrogen-air ratio.

In a reacting flow, the elemental fuel mass fraction used in the mixing efficiency parameter above must be modified. The elemental fuel mass fraction is found by tracking H atoms in the flow. The mass fraction of H_2 and H is used along with mass weighted mass fractions of H_2O, HO_2, HO and H_2O_2 to calculate the total mass fraction of H atoms in the evaluated plane. The mass fraction of H atoms is then used in Equation [5-2] to calculate a mass weighted mixing efficiency for the reacting simulation.

5.1.1.3 Plume Size Characteristics

A quantifiable measure of the penetration of the fuel plume into the main flow is given by the location of the center of mass in a cross-sectional plane (y-z) of the flow[85]

$$z^+ = \frac{\int \rho u \alpha z dA}{\int \rho u \alpha dA} \qquad \textbf{5-3}$$

Another plume parameter, the plume width, $y^{\pm}$, is defined by the distance between the plume side edges. The maximum vertical penetration, z_{max} and the plume width, $y^{\pm}$ are defined as the location on the edge of the plume where α is equal to the stoichiometric ratio for hydrogen in air, 0.0292.

5.1.2 Flow Field Visualization

Flow field visualization contours represent a cross section of the y-z plane located 16.4 effective diameters or 32 effective diameters downstream of injection. All experimental measurements were taken at 16.4 effective diameters. The planes extend 7 effective diameters in the vertical, z, direction and ±5 effective diameters laterally, y direction, from the centerline. Contours of mass fraction concentration (helium or hydrogen), Mach number, total pressure, Pitot pressure, total temperature and vorticity are shown. The total pressure and temperature contours are normalized by the freestream values.

5.2 Detailed Baseline Injector Predictions

The predictions for the Baseline, single round injector are presented in this section. The initial analysis used the default values for Pr_t = 0.9 and Sc_t = 0.5. A turbulence intensity of 5% was assumed for the freestream. The discussed predictions include the following: plume characteristics and integrated parameters, mass concentration, mixing, total pressure loss, total temperature, Mach number and vorticity contours. All integrated quantities are as defined above.

5.2.1 Mass Concentration and Mixing

The helium concentration contours found in Figure 5.1 show that the CFD predicts slower mixing of helium than the experiment. The helium concentration shown in the contour is the mass fraction of helium. The contours are slices in the y-z plane taken at x/d_{eff} of 16.4. The experimental results were taken by probing at 32 vertical locations and 11 lateral locations over the y-z plane and then interpolating between the points to create a contour. If the same number of grid points is used in the post-processing of the CFD analysis to create the concentration contour, Figure 5.2 is the result. The plume shape and contour levels in Figure 5.2 agree more closely with the experimental concentration results than the finer post-processing grid found in Figure 5.1. The number of grid points

used has a slight impact on the comparison. Both the experiment and CFD predict a horse-shoe shape of concentration with similar vertical penetration. The horse-shoe shape is indicative of the counter-rotating vortex pair that is formed from the jet injection into a cross flow. The fine CFD predicts slightly less lateral penetration than the experiment.

The maximum concentration is higher for the CFD predictions and the area of maximum concentration comprises a larger portion of the overall plume. Numerical mixing and mass diffusion is dominated by the choice of turbulence model and turbulence parameters. Studies are performed later in this chapter on turbulence parameters effect on the CFD predictions.

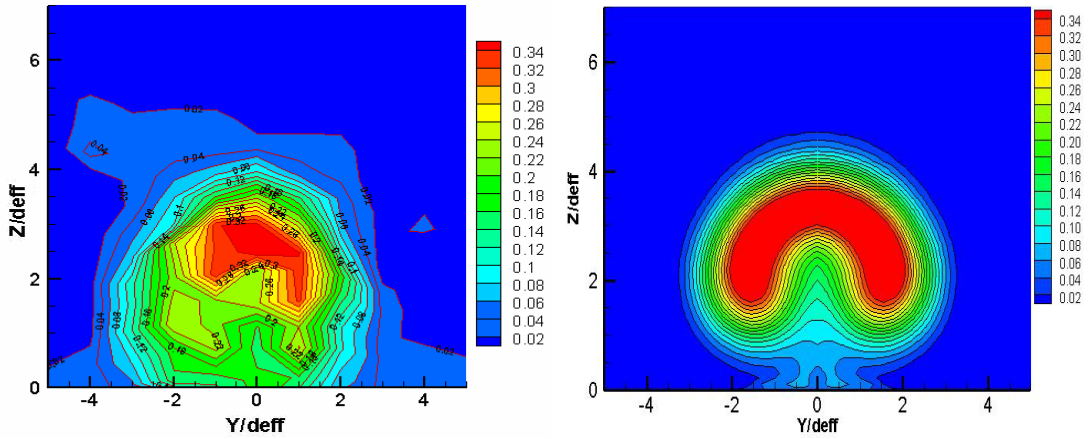

Figure 5.1 Calculated helium concentration contours in the x/d_{eff}=16.4 plane. The experimental result is on the left and the CFD prediction is on the right.

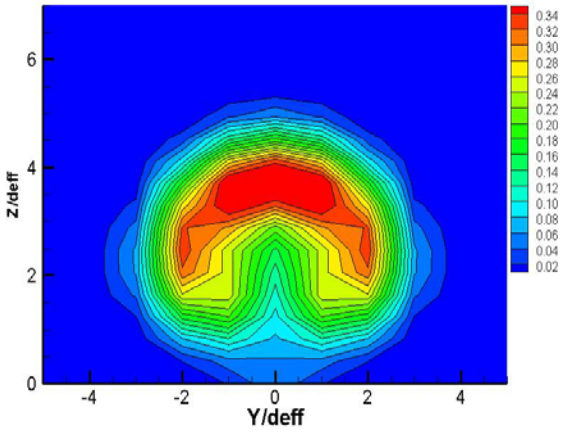

Figure 5.2 CFD prediction of helium concentration interpolated over a grid the same as the experiment.

Figure 5.3 plots helium concentration contours from the CFD prediction at two downstream locations, 16.4 effective diameters on the left and 32 effective diameters on the right. The maximum concentration at 32 effective diameters is 0.19 which is a 120% decrease in concentration from 16.4 effective diameters. The majority of the growth of the plume is in the vertical direction away from the surface. The rotation of the plume causes more vertical penetration than lateral spreading.

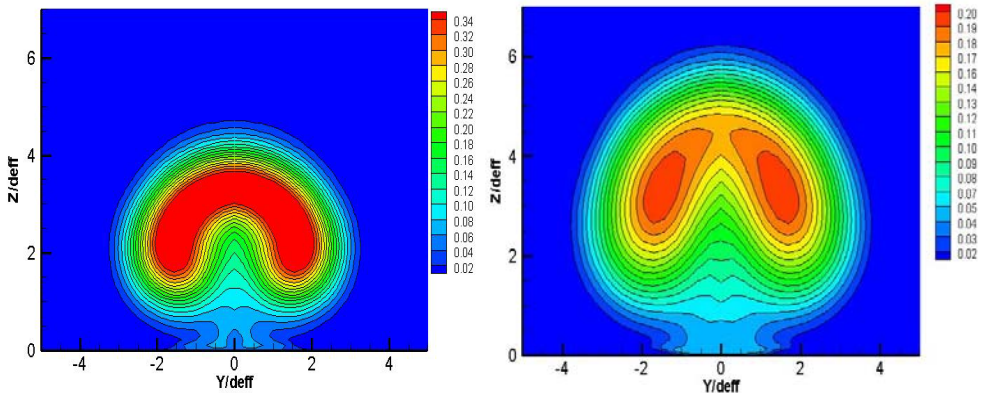

Figure 5.3 Calculated helium concentration contours in the x/d_{eff}=16.4 plane on the left and x/d_{eff}=32 plane on the right.

5.2.2 Total Temperature Ratio

The normalized total temperature contours can be found in Figure 5.4. The contours are slices in the y-z plane at x/d_{eff} = 16.4, and the total temperature was normalized by the freestream total temperature, 295 K. The total temperature contours are compared to the experimental results. Total temperature profiles allow for a qualitative and quantitative assessment of the penetration and mixing produced by the injectors. Crocco's Theorem relates fluid kinematics to thermodynamics of gases by Equation [5-4]. It states that total enthalpy gradients which are related to temperature gradients are accompanied by vorticity in compressible flows. The presence of vorticity (rotation) is beneficial for mixing flows.

$$T\nabla s = \nabla h_o - \vec{V} \times (\nabla \times \vec{V}) + \frac{\partial \vec{V}}{\partial t} \qquad \textbf{5-4}$$

The contours for both the experiment and CFD show the same horse-shoe shape found in the concentration contours, although the CFD predicts a steeper gradient between high and low total temperatures. Both contours have higher total temperature regions in the middle of each vortex. The difference in total temperature could be attributed to the definition of the incoming boundary layer. The inflow boundary layer profile was approximated based on turbulent methods and the known boundary layer height.

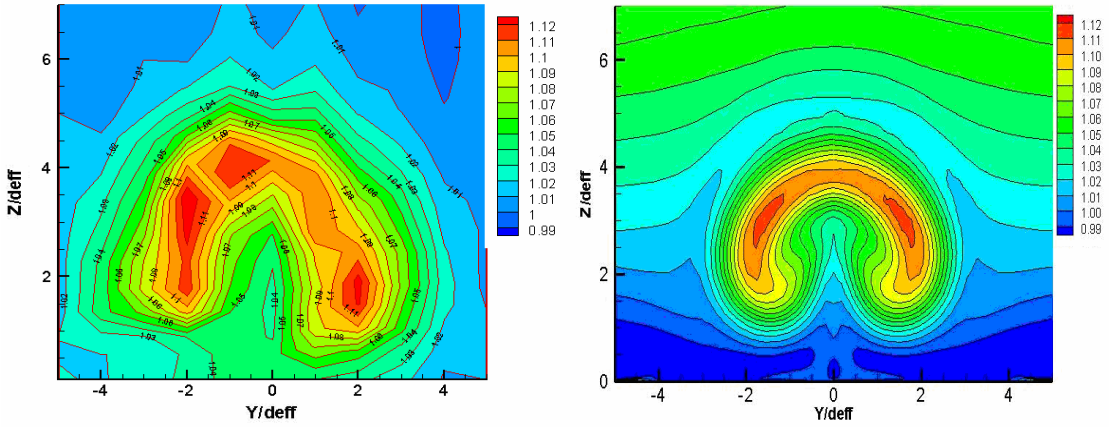

Figure 5.4 Normalized total temperature contours in the x/d_{eff}=16.4 plane. The experimental result is on the left and the CFD prediction is on the right.

5.2.3 Total Pressure

The predicted total pressure was used with the normal-shock relations to create plots of the Pitot pressure, P_{T2} (i.e. the total pressure measured using a hypothetic Pitot probe in the computed flow) found in Equation [5-4] below

$$\frac{P_{t2}}{P_{t1}} = \left[\frac{(\gamma+1)M_1^2}{(\gamma-1)M_1^2+2}\right]^{\gamma/(\gamma-1)}\left[\frac{\gamma+1}{2\gamma M_1^2-(\gamma-1)}\right]^{1/(\gamma-1)} \qquad \textbf{5-5}$$

The Pitot pressure was then normalized by the freestream total pressure. The resultant contours can be found in Figure 5.5. The Pitot pressure was used as a comparison with CFD because there is less data reduction involved in the experimental results and therefore less room for error when comparing the contours. The contours are slices in the

y-z plane taken at x/d_{eff} = 16.4. Total pressure contours allow for visualization of the losses incurred by the jet injection into a supersonic cross flow.

The contours look very similar between the CFD predictions and experimental results. The CFD analysis predicts the plume to be pulled off the surface, whereas the experimental results show a large area of low-pressure gas on the tunnel floor. The total pressure is more easily predicted by CFD tools because pressure losses are dictated more by momentum, a property less dependent on turbulence definitions, than the diffusion which dominates the mixing process.

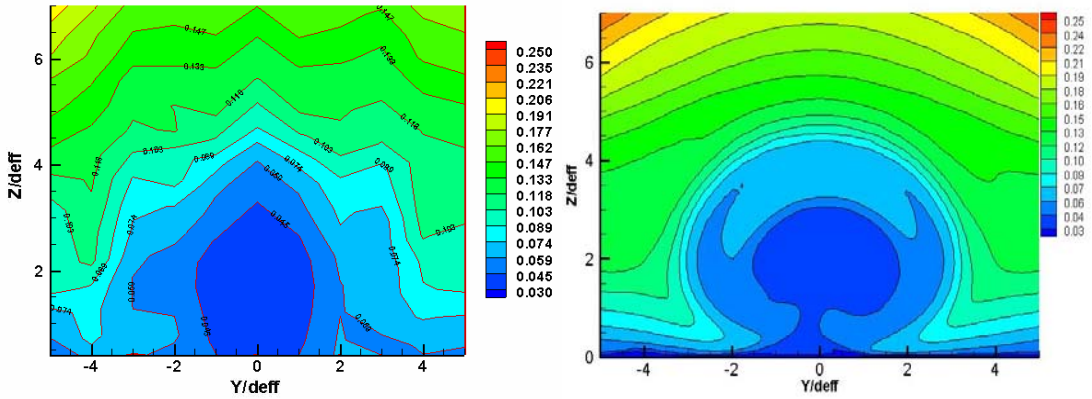

Figure 5.5 Normalized Pitot total pressure ratio in the x/d_{eff}=16.4 plane. The experimental result is on the left and the CFD prediction is on the right.

5.2.4 Mach Number Contours

Contours of the Mach number in the y-z plane at x/d_{eff} = 16.4 compared to experiment can be found in Figure 5.6. The interior of the plume is comprised of slower moving fluid than the surrounding areas. The slower moving region in the interior is beneficial for mixing quickly. The CFD software is able to predict the general shape and magnitude of the Mach number from the experiment. The fluid in the center of the plume is moving slightly faster in the prediction than in the experiment. Both contour plots show a dip towards the outside of the plumes. Considering just the left- hand side of the contours, the rotation of the plume cause by the CVP is in a counter-clockwise sense. As the fuel rotates, faster moving freestream air is entrained and then moves with the fuel towards the centerline. This produces the dip near the bottom, outside regions of the Mach

number contours. The stirring of the flow and the entrainment process are two of the primary mixing mechanisms of the CVP.

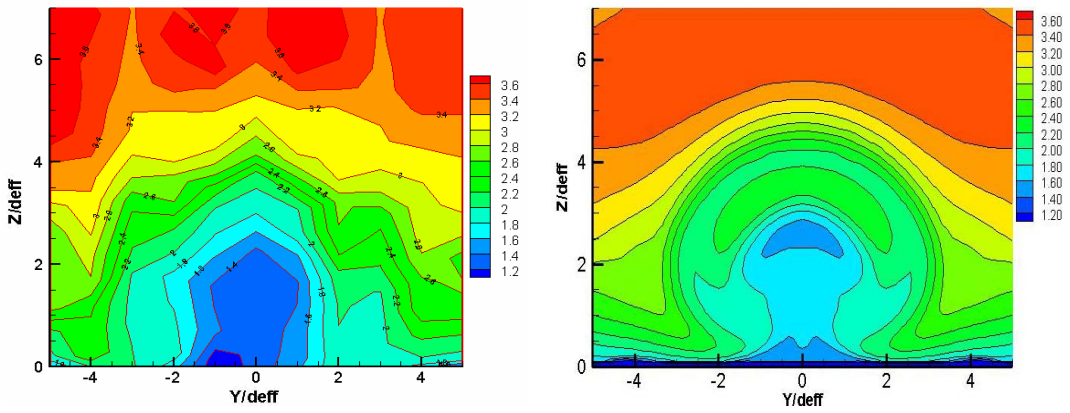

Figure 5.6 Mach number contours in the x/d_{eff}=16.4 plane. The experimental result is on the left and the CFD prediction is on the right.

5.2.5 Baseline Plume Characteristics and Integrated Parameters

This section presents in Table 5-1 the size, width and height of the jet plume at 16.4 and 32 effective diameters downstream. At 16.4 effective diameters, the CFD predictions are compared to the experimental results. CFD over-predicted the plume width by 0.6 effective diameters, but the maximum height agrees more closely with the experiment. Even though the plume center of mass is over-predicted, the overall area of the two plumes is similar.

The mixing efficiency parameter for the experiment and CFD agree very well (less than 1% difference) but the maximum concentration is over-predicted. The mixing efficiency parameter prediction was integrated over the smaller post-processing grid. However, there were minimal changes in mixing efficiency if the larger grid was used. The mixing efficiency is an area weight average that takes into account the mass flow rate of the fluid in addition to the fuel concentration.

The predicted total pressure loss parameter is similar to the experimental value. Total pressures are more easily predicted by the numerical simulation than the diffusion and mixing of species which can vary depending on the turbulence definitions.

CFD results can be used to extend the limited experimental data. Comparing the parameters at 16.4 and 32 effective diameters, the CFD analysis predicts that the plume width grows by 15% and the height increases by 19% from 16.4 effective diameters to 32 effective diameters. The maximum concentration decreases by 120% and the mixing efficiency increases by 70%.

Table 5-1 Plume characteristics and integrated parameters for the Baseline injector.

		Experiment Baseline $x/d_{eff} = 16.4$	CFD Baseline $x/d_{eff} = 16.4$	CFD Baseline $x/d_{eff} = 32$
Plume Width	**$y\pm$**	**5.80**	**6.40**	**7.36**
Maximum Plume Height	**z_{max}**	**5.20**	**5.17**	**6.13**
Plume Center of Mass	**z^{+}**	**1.75**	**2.82**	**3.22**
Maximum Concentration	**σ_{max}**	**0.34**	**0.42**	**0.19**
Mixing Efficiency	**η_m**	**0.20**	**0.20**	**0.34**
Total Pressure Loss Parameter	**Π**	**0.38**	**0.40**	**0.47**

5.2.6 Vorticity

Predicted vorticity magnitude contours in the $x/d_{eff} = 16.4$ plane and the $x/d_{eff} = 32$ plane can be found for the Baseline injector in Figure 5.7. Vortical flow enhances mixing through entrainment of freestream fluid and enhanced strain rates on the shear layer which increase the local diffusion gradients. The Baseline injector creates a horse-shoe contour that is to be expected of a jet in a cross flow. The interaction of the jet with a cross flow causes the jet plume to be pulled away from the surface and rotate up and away from the centerline. The plume contains a region of lower magnitude vorticity enclosed by a region of higher vorticity. Both contour plots show a region on the centerline of lower vorticity. The variation in vorticity or fluid rotation in the plume enhances the mixing. Further downstream, the largest magnitude of vorticity can be seen just off center on either side which corresponds to the cores of the counter rotating vortex pair.

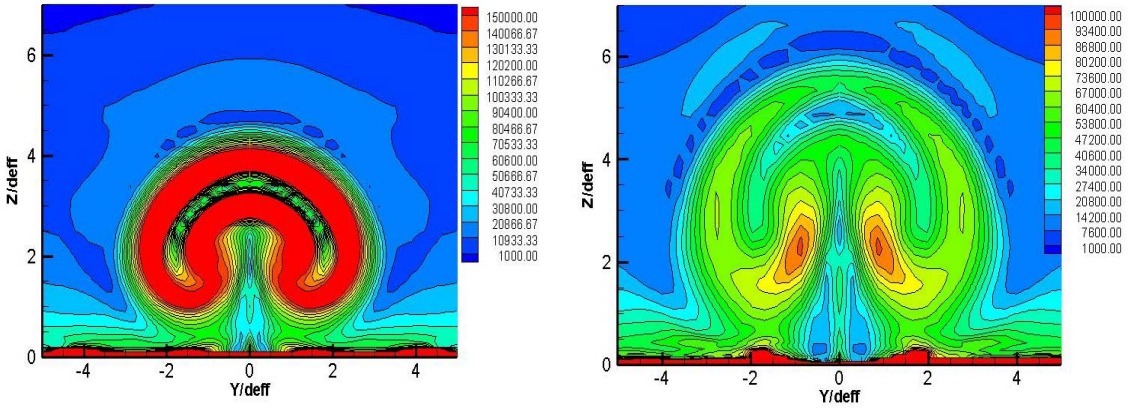

Figure 5.7 Predicted vorticity magnitude Baseline injector at the x/d_{eff}=16.4 plane on the left and the x/d_{eff}=32 plane on the right.

Figure 5.8 is a 3D plot of vorticity iso-surfaces for various constant levels of vorticity. The iso-surfaces offer a pictorial description of the behavior of the vorticity in the flow-field. Immediately behind the injector, the plume and entrained flow is further pushed away from the injector by the separation region. The iso-surfaces illustrate the rotating behavior of the single injector plume; the picture on the right clearly shows the counter rotating vortex pair. The CVP can also be seen by the streamlines in Figure 5.9. The fuel leaving the forward and side edges of the injector curls in a helical manner away from the bottom wall, this can been seen in the streamline contours found in Figure 5.10. Some of the fuel leaving the aft portion of the injector is caught near the surface and does not progress downstream with the core plume. Figure 5.10 also shows the horse-shoe vortex that forms just ahead of the separation region in front of the injector. There is a lower pressure region just aft of the injector that causes the flow that originally expanded away from the injector to curve back towards the centerline. This also aids with mixing in that more air is introduced into the fuel plume.

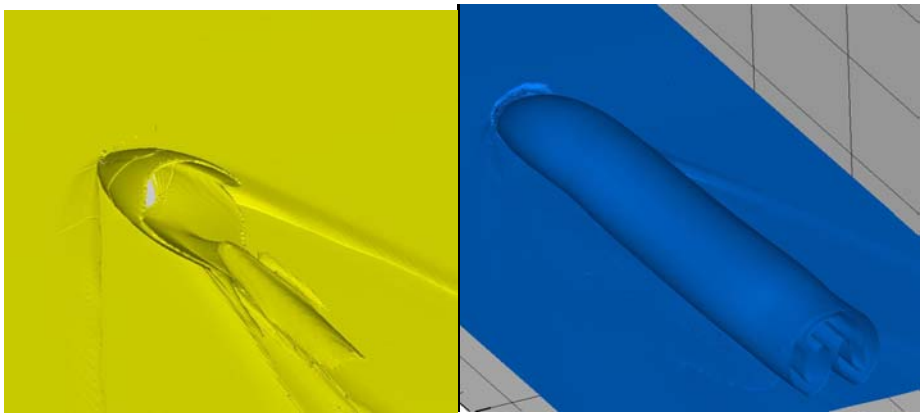

a. ω = 800,000 /sec **b. ω =100,000 /sec**

Figure 5.8 Iso-Surfaces of the Baseline Injector for two different vorticity strengths.

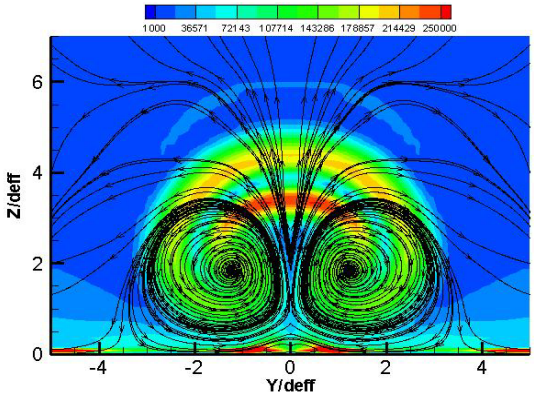

Figure 5.9 Vorticity contour with overlaid streamlines in the y-z plane at 16.4 effective diameters.

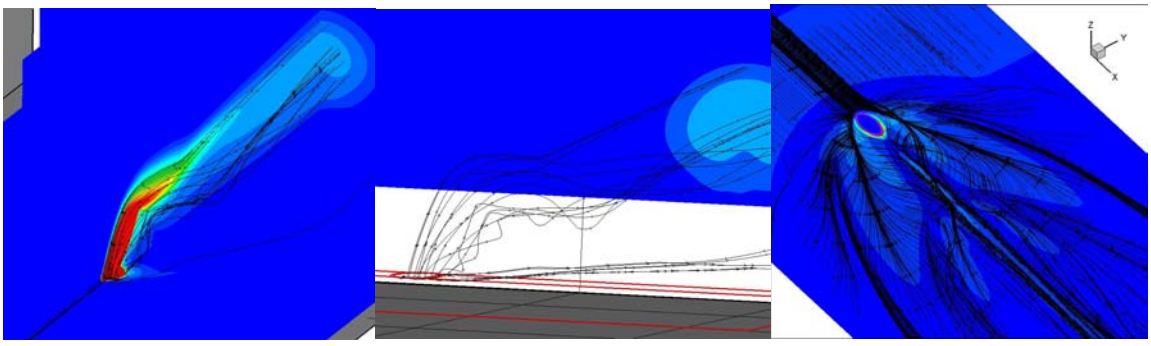

Figure 5.10 3D Momentum streamlines emanating from fuel jet. Flow is left to right.

5.3 Sensitivity Studies

Numerical analysis is used as a predictive tool throughout industry and academia. As computer technologies improve, so does the ability to more accurately predict various flow-fields. With the current technologies and resources, the tools must be appropriately calibrated to predict the physics of the actual flow. For the two-equation turbulence model used in this study, there are several turbulence parameters that can be adjusted to affect the outcome of the solution. To gain a better and more thorough understanding of how to model jets in a cross flow, trade studies were performed of the turbulence intensity, turbulent Prandtl number and turbulent Schmidt number. Next, the height of the in-flow boundary layer was varied to determine its influence. Lastly, predictions with the CFD software, GASP, are compared to the predictions with CFD software, FLUENT.

5.3.1 Turbulent Schmidt Number

The turbulent Schmidt number, Sc_t, used in GASP is a constant parameter defined by:

$$Sc_t = \frac{\mu_t}{\rho D_{t,ij}} \qquad 5\text{-}6$$

Where $D_{t,ij}$ is the binary diffusion coefficient, ρ is the local density and μ_t is the turbulent viscosity. The Schmidt number is the ratio of the diffusion of momentum to the diffusion of mass. It influences the behavior of small-scale turbulent structures and when $Sc_t<1$, mass diffusion is more dominate (than diffusion of momentum) which will play a large role in small-scale mixing. The default value in GASP is 0.5. The Sc_t was increased to 0.7 from 0.5 in the original Baseline CFD prediction. The yellow columns found in Table 5-2 represent the original Baseline predictions and the white columns on the right are for the adjusted Sc_t predictions.

An increase in Sc_t will decrease the rate at which mass is dispersed within the flow with respect to how momentum is diffused. A change in Sc_t slightly affects the predicted behavior of the flow-field. The results in the CFD predictions can be seen in Table 5-2 and Figure 5.11. The change in plume size caused by the increase in Sc_t, is

further from the experimental results than a Sc_t of 0.5. The plume center of mass is decreased by 0.2 effective diameters and the width is increased by 0.35 effective diameters. The mixing efficiency and maximum concentration do not vary significantly between predictions however, at 32 effective diameters the increased Sc_t prediction has a higher maximum concentration and lower mixing efficiency. The far-field mixing, downstream from injection, is more influenced by molecular diffusion and the turbulent Schmidt number influences the small-scale mixing in the flow-field. The result of the increased Schmidt number is a decrease in mass diffusion and an increase in fuel concentration.

Table 5-2 Integrated quantities for varying turbulent Schmidt numbers.

		Expr.	CFD $Sc_t = 0.5$		CFD $Sc_t = 0.7$	
	x/d_{eff}	16.4	16.4	32	16.4	32
Plume Width	$y\pm$	5.80	6.40	7.36	6.75	7.55
Maximum Plume Height	z_{max}	5.20	5.17	6.13	5.09	5.89
Plume Center of Mass	z^+	1.75	2.82	3.22	2.61	3.00
Maximum Concentration	σ_{max}	0.34	0.42	0.19	0.40	0.22
Mixing Efficiency	η_m	0.20	0.20	0.34	0.20	0.33
Total Pressure Loss Parameter	Π	0.38	0.40	0.47	0.39	0.47

Increasing Sc_t produces changes in the plume shape of the predictions but not overall significant changes in magnitude of the fuel concentration. Changes in the mass fraction contour can be seen in Figure 5.11 (a). The left-hand side of the contours in Figure 5.11 represents the original prediction for the Baseline injector and the right-hand side corresponds to the adjusted Sc_t analysis. A higher concentration of fuel is now found on the lower outside region of the plume. The total temperature contour, Figure 5.11 (b) predicts that an increase in Sc_t, with a decrease in mass diffusion, will decrease the total temperature in the core of the plume. The total pressure loss parameter, total pressure contour and Mach number contours do not change noticeably with varying Sc_t.

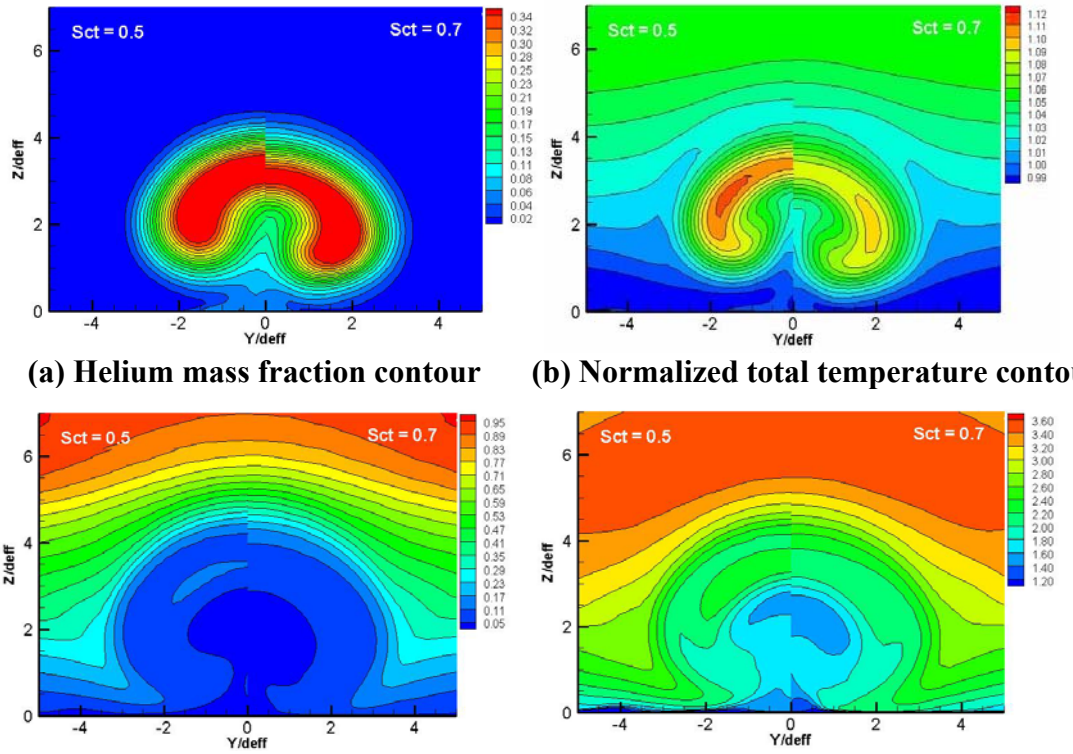

(a) Helium mass fraction contour **(b) Normalized total temperature contour**

(c) Normalized total pressure contour **(d) Mach number contour**

Figure 5.11 Turbulent Schmidt number contour comparisons. Original case with $Sc_t = 0.5$ is on the left and the case with $Sc_t = 0.7$ is on the right of each figure.

5.3.2 Turbulent Prandtl Number

The Prandtl number, Pr_t, is the ratio of the diffusion of momentum to the diffusion of heat. It relates the thermal conductivity to the eddy viscosity and density:

$$\mathrm{Pr}_t = \frac{\mu_t C_p}{k_t} = \frac{\mu_t / \rho}{k_t / (\rho C_p)} \qquad \textbf{5-7}$$

Where k_t is the thermal conductivity, Cp is the specific heat of the gas, ρ is the local density and μ_t is the turbulent viscosity. The Pr_t controls the relative thickness of the momentum and thermal boundary layers[86]. The Pr_t can be found in the energy equation controlling heat flux from turbulent gradients.

The original Baseline analysis was conducted using a default value for Pr_t of 0.9. The Pr_t was decreased to 0.7. The yellow columns found in Table 5-3 represent the

original predictions for the Baseline case, and the white columns on the right are for the adjusted Pr_t predictions. The effects of a decrease in Prandtl number can be seen in Table 5-3 and Figure 5.12. The plume size increases, both laterally and vertically, but the plume center of mass decreases 0.12 effective diameters. The decrease in the plume center of mass has better agreement with the experiment. The maximum concentration decreases to a value consistent with the experimental results also. The decrease in concentration causes the mixing efficiency to increase. The decrease in concentration can also be seen in the helium concentration contour, Figure 5.12(a). The left-hand side of the contours in Figure 5.12 represents the original Baseline prediction and the right-hand side corresponds to the adjusted Pr_t analysis. There is a decrease in total temperature seen in Figure 5.12(b). As the Pr_t number is decreased, the rate of heat diffusion with respect to mass diffusion increases. Therefore, the heated helium diffuses more rapidly into the freestream flow with a lower Pr_t number. The total pressure loss parameter and the total pressure contour do not vary with changes in Pr_t. The Mach number contour found in Figure 5.12 (d) depicts comparable Mach number values for the two predictions.

Table 5-3 Integrated quantities for varying turbulent Prandtl numbers

		Expr.	$Pr_t = 0.9$		$Pr_t = 0.7$	
	x/d_{eff}	16.4	16.4	32	16.4	32
Plume Width	$y\pm$	5.80	6.40	7.36	6.72	7.57
Maximum Plume Height	z_{max}	5.20	5.17	6.13	5.21	6.11
Plume Center of Mass	z^+	1.75	2.82	3.22	2.70	3.12
Maximum Concentration	σ_{max}	0.34	0.42	0.19	0.35	0.17
Mixing Efficiency	η_m	0.20	0.20	0.34	0.23	0.37
Total Pressure Loss Parameter	Π	0.38	0.40	0.47	0.40	0.46

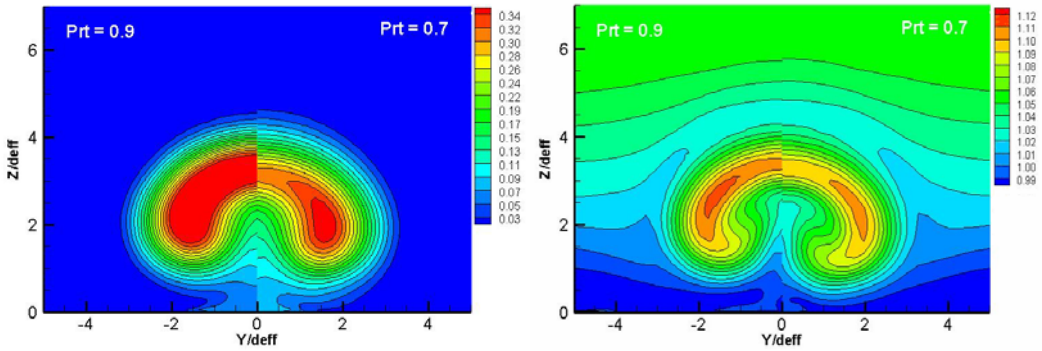

(a) Helium mass fraction contour **(b) Normalized total temperature contour**

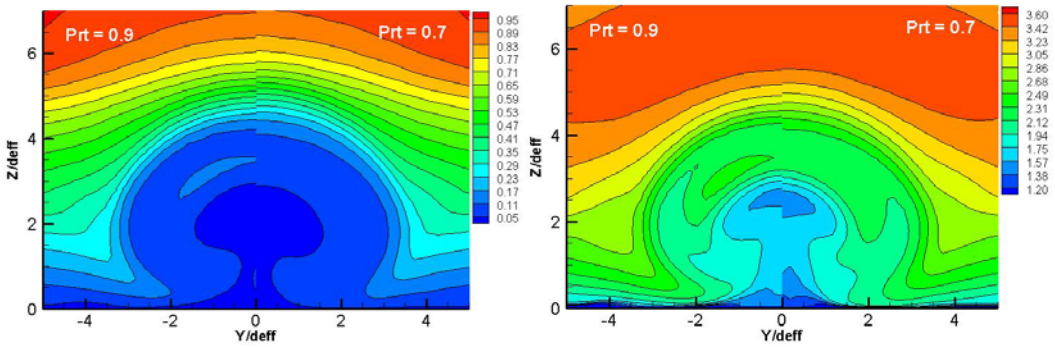

(c) Normalized total pressure contour **(d) Mach number contour**

Figure 5.12 Turbulent Prandtl number contour comparisons. Original case with $Pr_t = 0.9$ is on the left and the case with $Pr_t = 0.7$ is on the right.

A decrease in Pr_t for this case of heated light gas injected into a supersonic cross flow, leads to better agreement with the experimental results, specifically helium concentration and total temperature of the jet plume.

5.3.3 Freestream Turbulence Intensity

Turbulence intensity is defined as the ratio of the root-mean-square of the velocity fluctuations to the mean flow velocity. Usually, turbulence intensities above 10% are considered high[61].

The turbulence intensity in the wind tunnel used in the experiments was unknown. Therefore, an initial assumption of 5% was used for the Baseline predictions. To determine the effect turbulence intensity has on the CFD predictions, an additional analysis with a turbulence intensity of 15% was conducted. Increasing the turbulence intensity for this case of jets in a cross flow, resulted in small changes to the CFD predictions.

The jet plume penetrates less in the vertical direction but farther in the lateral direction, see Table 5-4. The contour plots in Figure 5.13 also show this trend. The maximum concentration decreases slightly with an increase in turbulence intensity. But the mixing efficiency is the same for a turbulence intensity of 5% and 15%. As turbulence intensity increases, the concentration plume becomes wider and shorter. Looking at the normalized total temperature, Figure 5.13(b), a turbulence intensity of

15% has moderately better mixing of the heated gas than a turbulence intensity of 5%. This can be seen by the larger region of lower temperature gas; more of the heated helium has mixed with the freestream. The Mach number contours, Figure 5.13(c), and normalized total pressure contours, Figure 5.13(d), are very similar for the two turbulence intensity cases. The contours differ in size of plume, but the magnitudes are alike. Higher freestream turbulence intensity improves mixing to a small extent for this particular case with a large defined boundary layer.

Table 5-4 Integrated quantities for varying turbulence intensities

		TI = 5%		TI = 15%	
	x/d_{eff}	16.4	32	16.4	32
Plume Width	$y\pm$	6.40	7.36	6.51	7.24
Maximum Plume Height	z_{max}	5.17	6.13	4.93	5.71
Plume Center of Mass	z^+	2.82	3.22	2.49	3.08
Maximum Concentration	σ_{max}	0.42	0.19	0.40	0.18
Mixing Efficiency	η_m	0.20	0.34	0.20	0.34
Total Pressure Loss Parameter	Π	0.40	0.47	0.42	0.47

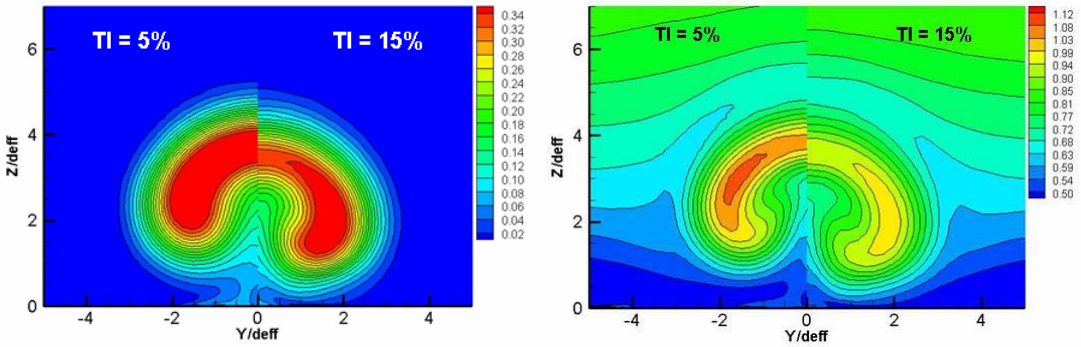

(a) Helium concentration contour (b) Normalized total temperature contour

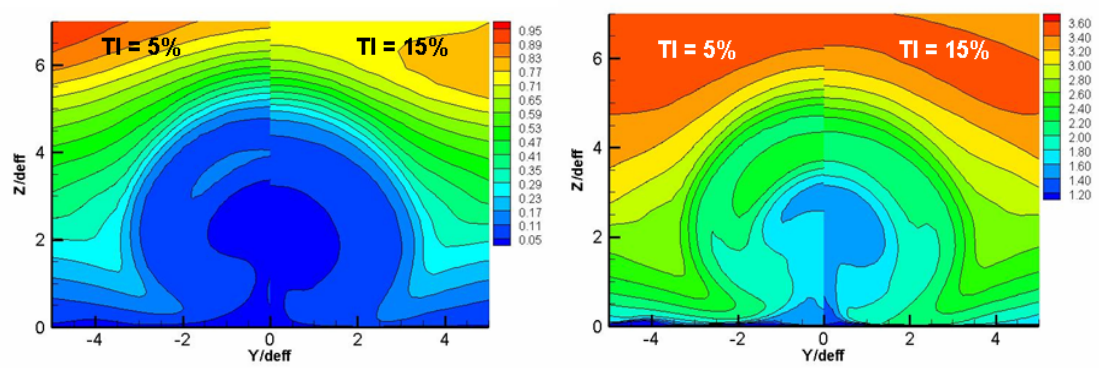

(c) Normalized total pressure contour **(d) Mach number contour**

Figure 5.13 Turbulent intensity contour comparisons. Original case with TI = 5% is on the left and the case with TI = 15% is on the right.

5.3.4 Computational Software Comparison

Computational fluid dynamics is a predictive tool that is used for its reduced cost and turn around time when compared to experimental testing. This section compares two different CFD software tools, GASP and FLUENT, in the ability to predict transverse jet injection into a supersonic cross flow. The input deck used in both software packages is set up identically. The boundary layer in both cases is slightly smaller than the boundary layer used in the Baseline analysis. These studies were performed before the boundary layer thickness was accurately determined. As a result, the contours and integrated parameters are slightly different than what are found above in the Baseline predictions. Since this is a comparison of just the CFD predictive tools, a small discrepancy in boundary layer size is acceptable.

The helium mass fraction contours can be found in Figure 5.14. Both software packages are able to predict the trends and behavior of the physical flow-field. There is good agreement between the integrated quantities and the contour plots. The plume height and width are very similar between the two software tools. GASP predicts a slightly wider plume. The plume center of mass agrees well between the two software packages. FLUENT predicts a more cone-like shape at the top of the plume, whereas GASP predicts a rounded, circular shape. The slight difference in shape could lead to the small discrepancy in mixing efficiency. Both software packages predict the total pressure losses found in the experiment.

Table 5-5 Integrated quantities for the Baseline case using GASP and FLUENT

		GASP	FLUENT
	x/d_{eff}	16.4	16.4
Plume Width	$y\pm$	5.14	5.04
Maximum Plume Height	z_{max}	4.50	4.48
Plume Center of Mass	z^{+}	2.41	2.42
Maximum Concentration	σ_{max}	0.57	0.55
Mixing Efficiency	η_m	0.18	0.15
Total Pressure Loss Parameter	Π	0.40	0.40

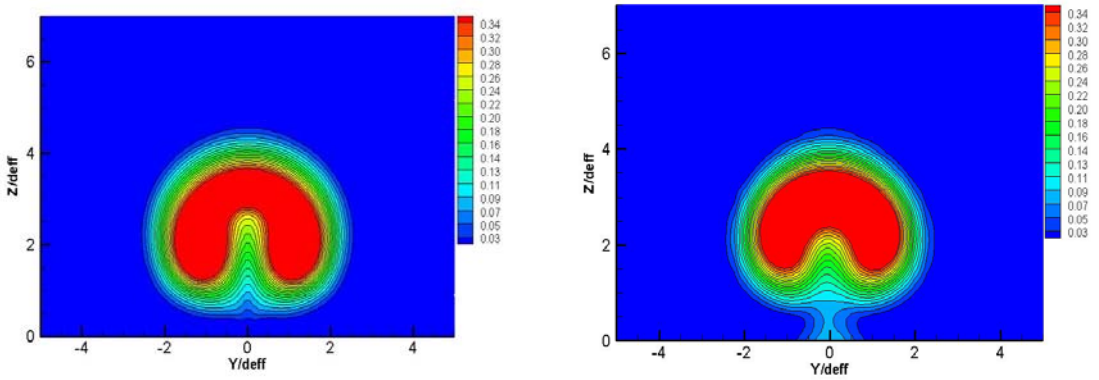

Figure 5.14 Helium mass fraction contours at 16.4 effective diameters downstream from injection, y-z plane comparing GASP and Fluent.

5.3.5 Boundary Layer Size Effects

This section presents helium mass fraction predictions comparing the Baseline injector with a boundary layer of 20 mm and a boundary layer of 8 mm at the point of injection. Comparing the two solutions shows that the predicted plume produced using a larger incoming boundary layer had better mixing capabilities. The integrated parameters can be found in Table 5-6. The predicted plume size is smaller for the smaller boundary layer both laterally and vertically. The location of the plume center of mass is also lower for the smaller boundary layer analysis. The maximum helium concentration is considerably higher for the smaller boundary layer and consequently the mixing efficiency is lower. The total pressure is similar for the two analyses.

Table 5-6 Integrated parameters for the Baseline injector with different freestream boundary layers

		CFD Baseline 20 mm bl	CFD Baseline 8 mm bl
Plume Width	$y\pm$	6.40	5.14
Maximum Plume Height	z_{max}	5.17	4.50
Plume Center of Mass	z^{+}	2.82	2.41
Maximum Concentration	σ_{max}	0.42	0.57
Mixing Efficiency	η_m	0.20	0.18
Total Pressure Loss Parameter	Π	0.40	0.40

The helium concentration contours can be found in Figure 5.15. One of the most noticeable differences in the two contours is the shape and size of the region of maximum concentration. The smaller boundary layer, pictured on the right, has a much larger area of maximum helium concentration than the larger boundary layer, pictured on the left. The plume size is also different, the larger boundary layer analysis predicted a wider and taller plume. This corresponds to faster spreading and mixing of the fuel with air. The larger boundary layer consists of a larger region of slower moving fluid. The slower it takes for the fuel to progress downstream, the easier it is for the fuel to mix with the freestream air. The faster moving freestream hinders mixing.

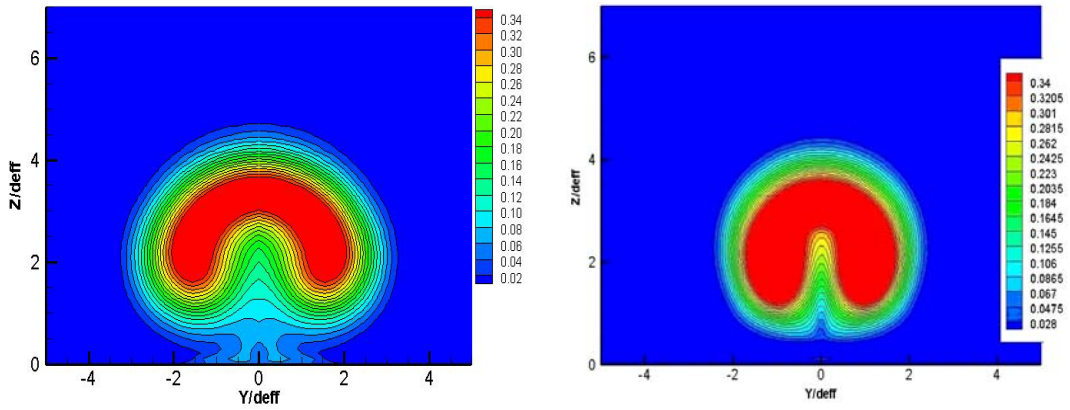

Figure 5.15 Calculated helium concentration contours in the x/d_{eff}=16.4 plane. The boundary layer of 20 mm is on the left and 8 mm is on the right.

The smaller incoming boundary layer changed the mixing characteristics of the helium with supersonic freestream air. The larger boundary layer had a larger velocity profile, which allowed for faster mixing and mass diffusion. The spreading rate of the plume predicted by the larger boundary layer is also larger in that the plume has more penetration both vertically and laterally.

Chapter 6: Injector and Flow: Comparison to the Baseline

In this section, numerical predictions for several injector and flow variations are presented and compared to the best Baseline predictions and the experimental results. First, an aeroramp injector consisting of an array of four orifices and a diamond or wedge-shaped injector that are both aligned and yawed to the incoming flow are examined and compared to the Baseline injector. Next, shocks are impinged upon the jet at three locations downstream of injection. Finally, comparisons of non-reacting and reacting simulations are also performed. The experimental data used for comparison have been collected and were discussed in Chapter 4. The analyses were conducted using a Pr_t = 0.7, Sc_t = 0.5 and freestream turbulence intensity = 5%. Flow-field visualization contours, mixing efficiency, total pressure losses and plume size will be discussed. Each of these categories was previously presented in Chapter 5-1.

6.1 Aeroramp Injector

The performance of the Baseline injector, a single round orifice is compared to that of an aerodynamic ramp injector array of four orifices. The transverse injector array has a total effective area equivalent to the Baseline injector. The aeroramp injector design was originally optimized for a Mach 2.4 cross flow with a hydrocarbon fuel. This research accesses the capability of that aeroramp injector in a Mach 4 cross flow with hydrogen fuel by comparing the performance to the Baseline injector and the experimental results. The predictions include the following: mass concentration, mixing, total pressure loss, total temperature, Mach number and vorticity. All integrated quantities were defined above.

6.1.1 Mass Concentration Contours

The helium concentration contour comparison of the CFD prediction and the experiment for the aeroramp injector can be found in Figure 6.1. The contours are slices in the y-z plane taken at the measurement plane, x/d_{eff} = 16.4. The CFD analysis predicts similar concentration levels. The location of maximum concentration is slighter higher in the vertical direction for the aeroramp injector. The plume penetration is over-predicted by the CFD analysis but the lateral penetration agrees well.

The aeroramp injector has two distinct plume cores off the centerline which show evidence of the main CVP. Air is captured between the left and right sets of injectors and as the plume progresses downstream that region increases the shear layer of the overall plume which increases the entrainment mechanism. The CFD predictions show less concentration of helium on the wall surface especially near the edges of the plume, but the experiment is an interpolated contour and the exact wall values were not measured.

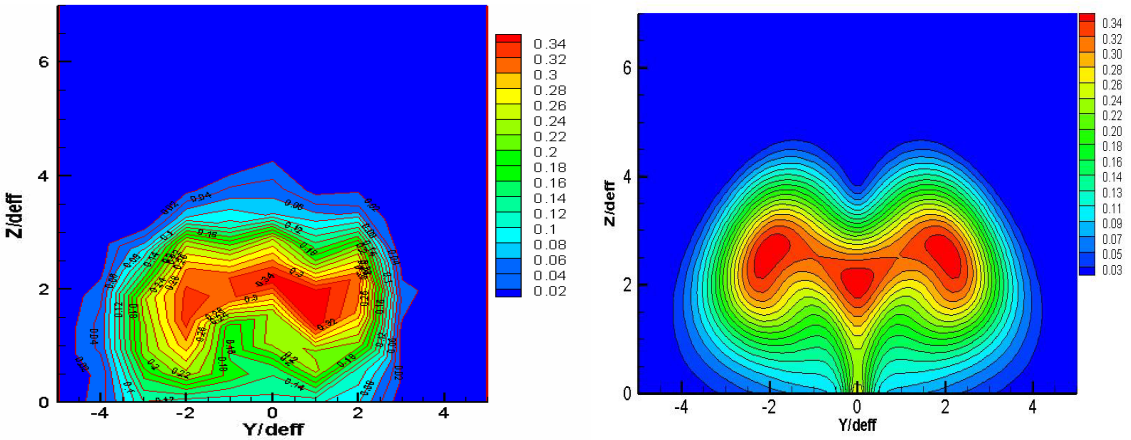

Figure 6.1 Calculated helium concentration contours in the x/d_{eff}=16.4 plane of the aeroramp injector compared to experiment. The experimental result is on the left and the CFD prediction is on the right.

Predicted helium mass fraction contours in the y-z plane at x/d_{eff} = 16.4 comparing the Baseline injector and the aeroramp injector can be found in Figure 6.2. The Baseline injector has a similar area of high mass fraction fluid. The aeroramp injector has a larger plume area than the predicted Baseline injector. The aeroramp injector has three regions of high concentration cores and the Baseline injector has one horseshoe region with two main cores at these concentration levels. The Baseline injector

is able to push more helium away from the surface on the centerline than the aeroramp injector. The gradient of helium concentration from inner plume to the outer region of the plume is more gradual for the aeroramp injector; there are larger regions of each level of concentration for the aeroramp injector.

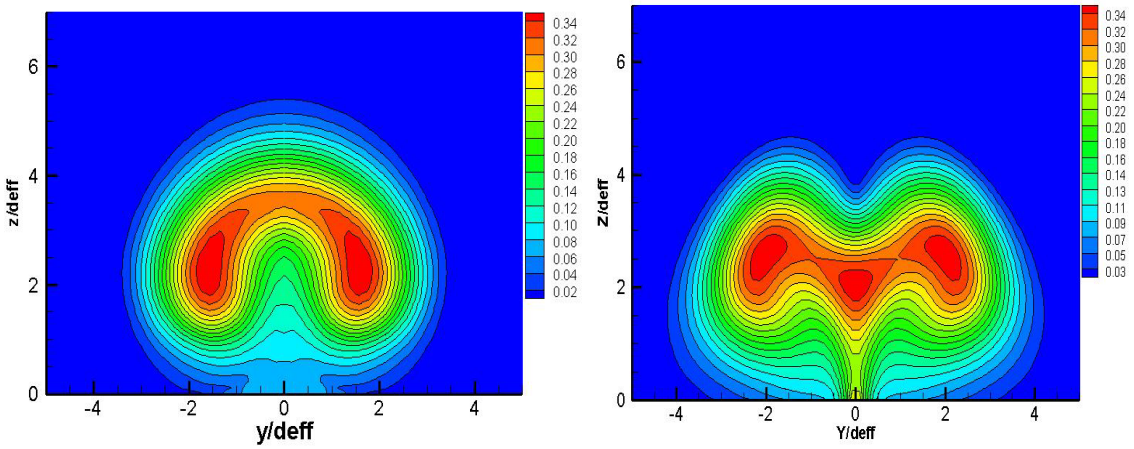

Figure 6.2 Calculated helium concentration contours in the x/d_{eff}=16.4 plane for the Baseline and aeroramp injectors. The Baseline prediction is on the left and the aeroramp prediction is on the right.

Predicted helium mass fraction contours at x/d_{eff} = 32 for the aeroramp injector configuration can be found in Figure 6.3. Note that the contour levels are not the same as the x/d_{eff} = 16.4 contours above. In order to better visualize the shape of the mass fraction in the plume at 32 effective diameters, the mass fraction contour levels were lowered. At 32 effective diameters, the region of highest helium mass fraction for the aeroramp injector has flattened across the plume. The aeroramp continues to have a wider area of helium concentration than the Baseline injector. The general shapes of the two plumes have not changed significantly over the plumes at 16.4 effective diameters but the concentration levels are significantly less. The levels of higher concentration gas are similar between the Baseline and aeroramp injectors, with the aeroramp having slightly higher mass fraction in the core of the plume.

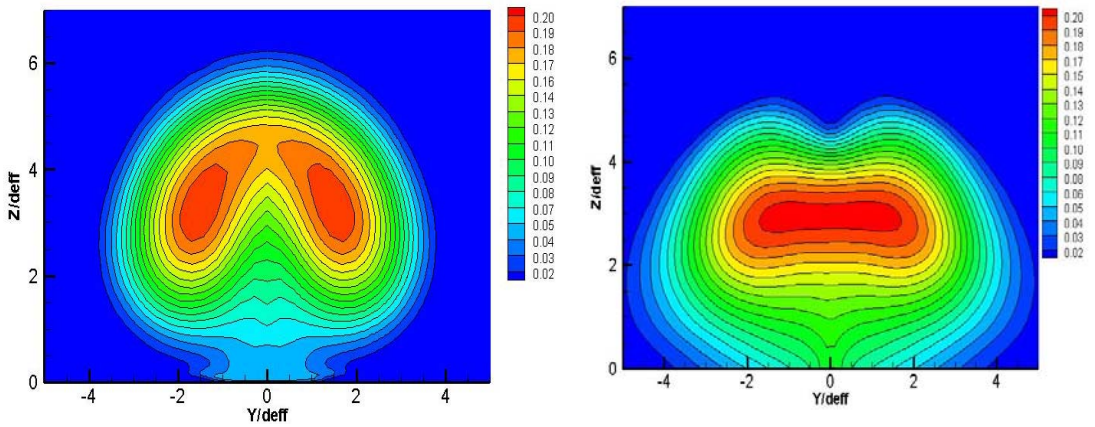

Figure 6.3 Calculated helium concentration contours in the x/d_{eff}=32 plane for the Baseline and aeroramp injectors. The Baseline prediction is on the left and the aeroramp prediction is on the right.

6.1.2 Total Temperature Ratio Contours

The total temperature contours for the aeroramp injector can be found in Figure 6.4. The CFD prediction of the total temperature is compared to the experimental result. The contours are slices in the y-z plane at x/d_{eff} = 16.4. The total temperature was normalized by the freestream total temperature, 295 K. The CFD and experimental predictions for the aeroramp injector show an area of low total temperature in the center of two higher total temperature cores. The low total temperature region is located at the top of the plume in the CFD prediction and in the middle of the plume for the experimental results. The magnitude is lower for the CFD than for the experiment. From the total temperature contours, it can be implied that the experiment mixes better than the CFD predicts because of the better mixing of the heated helium with the temperature of the freestream gas. The CFD shows a very low total temperature region surrounding the plume around the bottom edges of the contour plane. The total temperature gradient in the upper half of the CFD contour plane is not shown in the experimental contour. This could be attributed to the defined boundary layer in the CFD model. The fluid away from the plume is at a lower total temperature for the experiment than the for the CFD prediction.

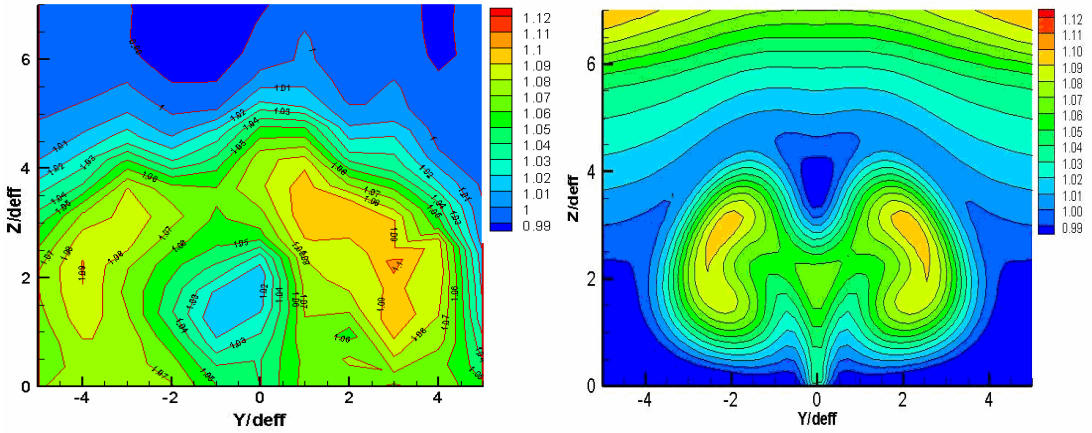

Figure 6.4 Predicted normalized total temperature ratio in the x/d_{eff}=16.4 plane of the aeroramp injector. The experimental result is on the left and the CFD prediction is on the right.

Comparisons of the total temperature ratio contours for the Baseline and aeroramp injector designs can be found in Figure 6.5. The aeroramp injector has a colder total temperature core than the Baseline injector. The lower total temperature regions of the aerormap injector can indicate better mixing of the heated helium.

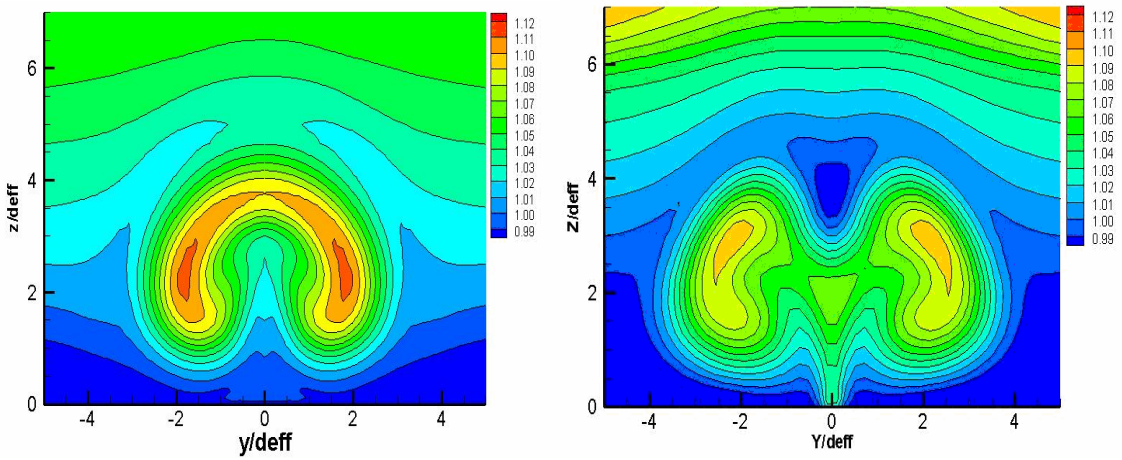

Figure 6.5 Calculated total temperature ratio contours in the x/d_{eff}=16.4 plane for the Baseline and aeroramp injectors. The Baseline prediction is on the left and the aeroramp prediction is on the right.

6.1.3 Mach Number Contours

Contours of Mach number in the y-z plane at x/d_{eff} = 16.4 compared to experiment for the aeroramp injector can be found in Figure 6.6. The CFD predicts slightly lower Mach numbers across the contour. The Mach number in the center of the plume is lower for the CFD prediction, but the fluid on the outer edges of the plume agrees well between the contours. The experiment is asymmetric but the lateral penetration of fluid moving at approximately Mach 2.0 on the left-hand side of both contours has very similar lateral penetration.

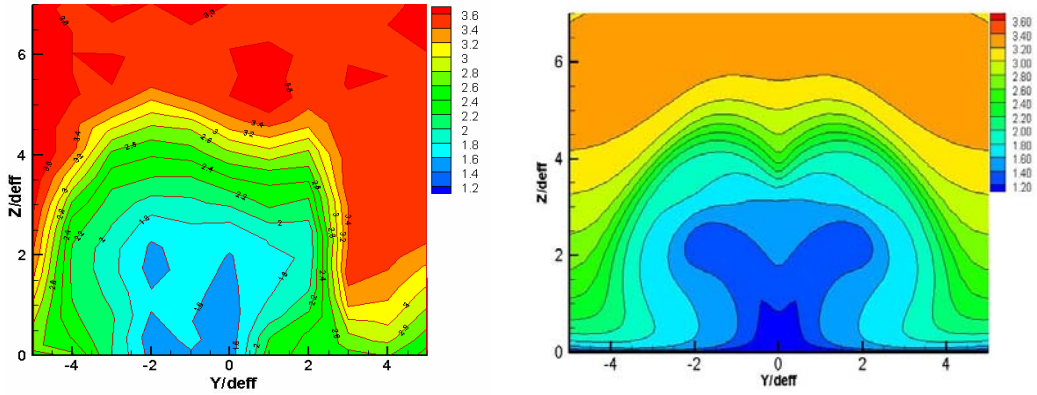

Figure 6.6 Calculated Mach number contours in the x/d_{eff}=16.4 plane of the aeroramp injector. The experimental result is on the left and the CFD prediction is on the right.

The CFD Mach number predictions for the aeroramp injector compared to the Baseline injector at 16.4 effective diameters can be found in Figure 6.7. The aeroramp injector has a larger area of slower moving fluid. This area begins on the centerline and branches outward. Slower moving fluid allows for higher residence times in a combustion chamber and aids in mixing of the fuel and air. The combination of multiple shocks created by injection from four orifices and the interaction of four fuel plumes plays a role in reducing the overall speed of the flow when compared to the Baseline injector. The second set of injectors contributes to the further slowing down of the plume core.

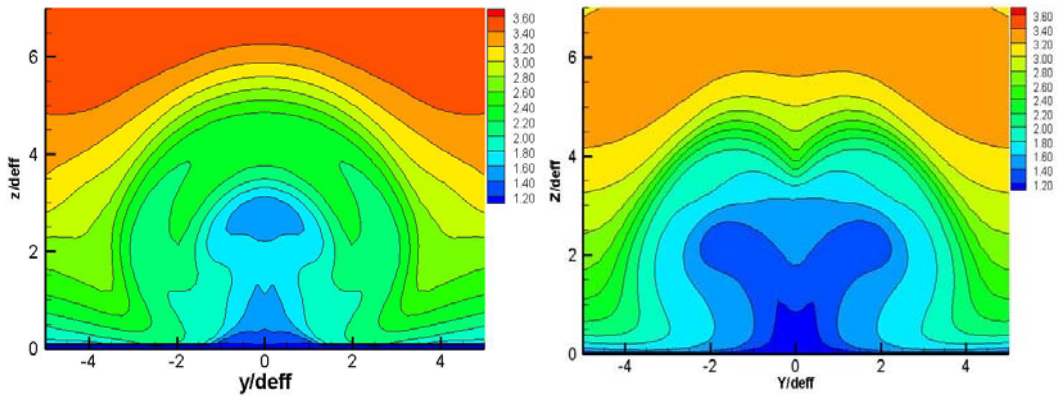

Figure 6.7 Comparison of calculated Mach number contours in the x/d_{eff}=16.4 plane for Baseline and aeroramp injectors. The Baseline prediction is on the left and the aeroramp prediction is on the right.

6.1.4 Total Pressure Ratio Contours

The predicted total pressure transformed with the normal-shock relations to create the Pitot pressure, P_{T2} (i.e. the total pressure measured using a hypothetical Pitot probe in the computed flow) and then normalized by the freestream total pressure to create contour plots of normalized Pitot pressure. The resultant contours can be found in Figure 6.8. The Pitot pressure was used as a comparison with CFD because there is less data reduction involved in the experimental data and therefore less room for error when comparing the contours. The contours are slices in the y-z plane taken at x/d_{eff} = 16.4. There is good agreement between the CFD and the experiment. The CFD predicts similar magnitudes in total pressure at the plume center. The low pressure ratio gas extends further vertically in the experiment than in the CFD prediction.

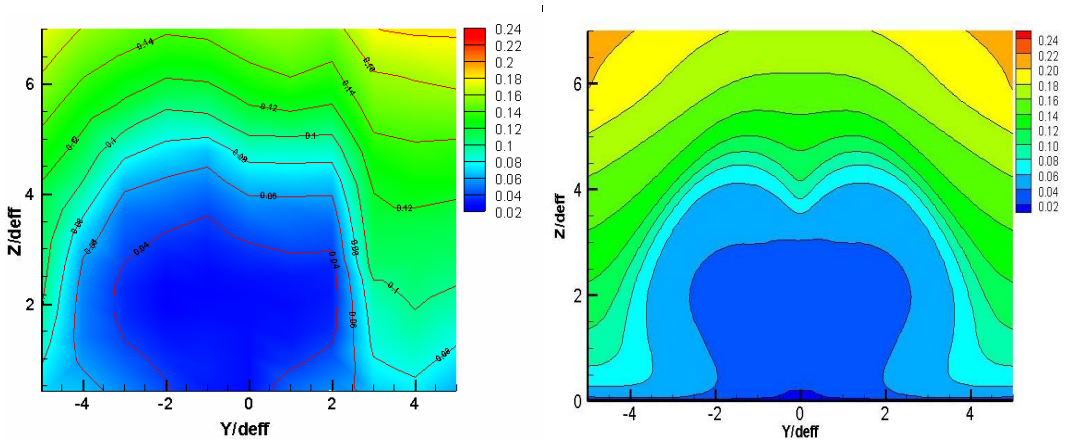

Figure 6.8 Normalized Pitot total pressure ratio in the x/d_{eff}=16.4 plane of the aeroramp injector. The experimental result is on the left and the CFD prediction is on the right.

The predicted Pitot pressure contour for the aeroramp injector is compared to that for the Baseline injector in Figure 6.9. The aeroramp produces a larger region of the lowest contour level of total pressure. The low pressure gas extends further laterally for the aeroramp injector than the Baseline injector. The dips found on the outside of the Baseline contour are not present in the aeroramp contour in this contour frame. The aeroramp configuration of four injectors with interacting flow-fields alters the behavior of the CVP through variations in total pressure between and around the four injectors. However, the aeroramp does not have a significant increase in total pressure loss from the Baseline injector because the largest losses come from the initial shocks ahead of the first row of injectors. The losses caused by the second row of injections are much less in comparison. The overall effect is similar pressure losses produced by both injectors.

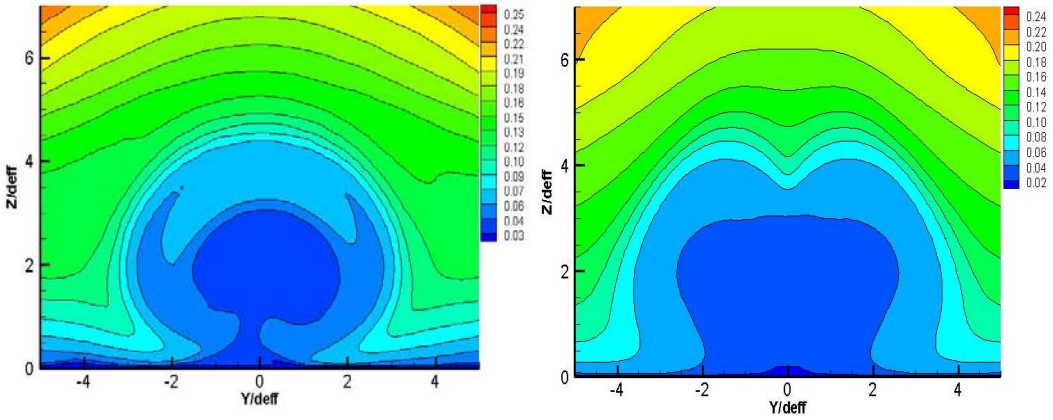

Figure 6.9 CFD prediction of normalized Pitot pressure ratio in the x/d_{eff}=16.4 plane. The Baseline prediction is on the left and the aeroramp prediction is on the right.

6.1.5 Plume Characteristics and Integrated Parameters

The plume center of mass and the mixing efficiency for the aeroramp injector is plotted at several downstream locations in Figure 6.10. The center of mass and the mixing efficiency, defined earlier, are integrated over several y-z cross-planes. The plot compares the aeroramp injector to the Baseline injector. The plume center of mass for the Baseline injector penetrates further into the freestream at every downstream location. The mixing efficiency, initially, is slightly higher for the aeroramp injector. After approximately 20 effective diameters, the Baseline injector has higher mixing efficiencies. The interaction of the four jets produced by the aeroramp injector produces better initial large-scale mixing of the fuel and air. The benefit in early increased mixing efficiency for the aeroramp injector is a minimum fuel residence time and shorter distance to thorough mixing.

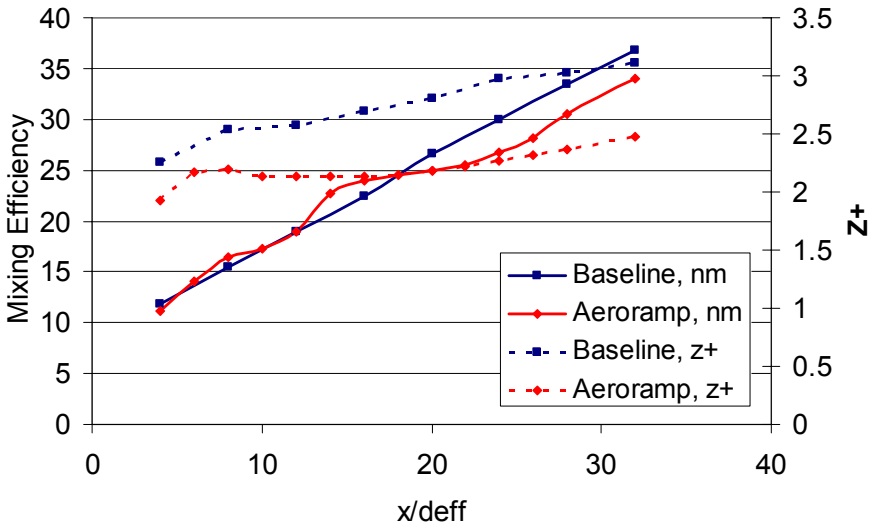

Figure 6.10 Downstream progression of the mixing efficiency and plume center of mass for the aeroramp injector compared to the Baseline injector.

This section presents the size, width and height of the plume at 16.4 effective diameters downstream for the aeroramp injector. The mixing efficiency and maximum helium concentration predict how well the aeroramp mixes the fuel with the freestream air. The total pressure loss parameter is also presented and does not differ largely between the experiment and CFD. Predictions for the aeroramp injector are compared to the experimental results in Table 6-1. The flow-field produced by the aeroramp injector is predicted by the CFD analysis. The predicted plume width and height are slightly larger than the experimental result, 0.25 effective diameters and 0.14 effective diameters respectively. The experimental probe measured approximately every 0.2 effective diameters, so a difference of 0.14 effective diameters could be contained within the interpolation error. The CFD analysis predicts a higher plume center of mass, 0.35 effective diameters. However, the mixing efficiency and the maximum concentration are in good agreement between the CFD analysis and the experimental results. The CFD over-predicted the maximum concentration by 3% which is within experimental uncertainty of the concentration probe, 7%.

Table 6-1 Plume characteristics and integrated parameters for the aeroramp injector at 16.4 effective diameters downstream from injection.

		Aeroramp Injector	
		Experiment	CFD
Plume Width	$y\pm$	7.90	8.15
Maximum Plume Height	z_{max}	4.50	4.64
Plume Center of Mass	z^{+}	2.00	2.14
Maximum Concentration	σ_{max}	0.34	0.35
Mixing Efficiency	η_m	0.22	0.24
Total Pressure Loss Parameter	Π	0.40	0.41

The CFD predictions comparing the aeroramp injector with the Baseline injector at 16.4 and 32 effective diameters can be found in Table 6-2. The aeroramp has a larger overall plume area with larger lateral penetration. The larger lateral penetration is expected for the aeroramp injector because the array is two injectors wide. The CFD predicts faster plume growth for the aeroramp injector than the Baseline injector from 16.4 effective diameters to 32 effective diameters. The maximum concentration and the mixing efficiency of the aeroramp and Baseline injector are very similar. Both the CFD prediction and the experimental results have a slightly smaller mixing efficiency for the Baseline injector than the aeroramp injector. The Baseline injector has a larger decrease in maximum concentration than the aeroramp injector at 32 effective diameters. The aeroramp and the Baseline injectors have the same total pressure loss parameter at 32 effective diameters. The aeroramp injector slightly improves mixing near injection over the Baseline injector without additional pressure losses.

Table 6-2 Plume characteristics and integrated parameters for the aeroramp injector at 32 effective diameters downstream from injection

		CFD Baseline Injector		CFD Aeroramp Injector	
x/d_{eff} location		16.4	32	16.4	32
Plume Width	$y\pm$	6.72	7.57	8.15	9.31
Maximum Plume Height	z_{max}	5.21	6.11	4.64	5.14
Plume Center of Mass	z^{+}	2.70	3.12	2.14	2.48
Maximum Concentration	σ_{max}	0.35	0.17	0.35	0.20
Mixing Efficiency	η_m	0.23	0.37	0.24	0.34
Total Pressure Loss Parameter	Π	0.40	0.47	0.41	0.47

6.1.6 Vorticity

Predicted vorticity magnitude contours in the x/d_{eff} = 16.4 and x/d_{eff} = 32 planes can be found for the aeroramp injector in Figure 6.11. Vortical flow enhances mixing through entrainment of freestream fluid and enhanced strain rates on the shear layer which increase the local diffusion gradients. The aeroramp improves mixing through increased large-scale mixing near injection while maintaining similar small-mixing behavior with the Baseline injector. Entraining of the freestream air between the injectors increases the stirring or macro-mixing of the fuel and air. A larger interface of fuel and air is then created which results in larger strain rates on the surface and more area for mass diffusion from molecular mixing. The interaction of the four injectors is also beneficial for the mixing process because vorticity is created from each injector in the array and the resultant plume contains the combination of vorticity from each injector. In addition, the interaction of the four plumes increases the turbulence in the flow and makes each individual plume more unstable initially.

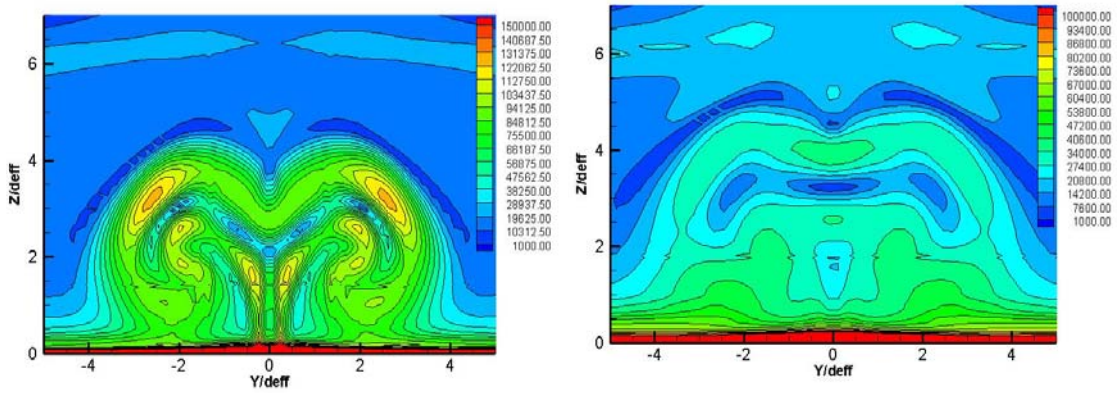

Figure 6.11 Predicted vorticity ratio in the x/d_{eff}=16.4 plane on the left and x/d_{eff}= 32 plane on the right of the aeroramp injector.

Vorticity contours of the Baseline and aeroramp injectors are compared to each other at x/d_{eff} = 16.4 in Figure 6.12. The Baseline injector has stronger vorticity in the plume. Both contours show regions of high vorticity that are sandwiched between regions of low vorticity. The interface of high and low vorticity can be compared to the fuel/air shear layer of the plume. The aeroramp has a larger interface of high and low vorticity than the Baseline injector. The aeroramp injector mixes faster than the Baseline injector by creating a larger interfacial surface area to entrain the freestream fluid. The Baseline injector appears to pull the helium away from the surface better than the aeroramp injector, however, the aeroramp has less vorticity on the surface and in the plumes as a result of improved mixing. The comparison of the two contours shows similar trends to the comparison of the Mach number contours. The Baseline predicted a higher Mach number plume and also a higher vorticity plume than the aeroramp injector.

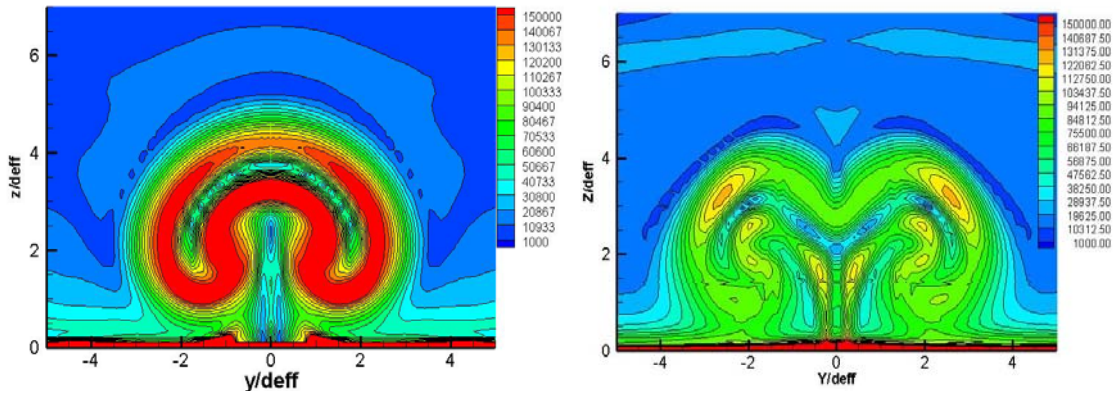

Figure 6.12 CFD prediction of vorticity in the x/d_{eff}=16.4 plane. The Baseline prediction is on the left and the aeroramp prediction is on the right.

Figure 6.13 shows vorticity iso-surfaces for various constant levels of vorticity for the aeroramp injector. The iso-surfaces offer a pictorial description of the behavior of the vorticity in the flow-field. Behind the first set of injectors in the aeroramp configuration, the existing fuel plume with some vorticity encounters the flow from the second row of injectors with their own vorticity. Some of the fuel-air mixture produced from the first set of injectors bends around and over the second set. This is why the aeroramp injector produces a larger plume area than the Baseline injector. The remainder of the fuel-air mixture flows between the rear set of injectors and is entrained in the rear injector flow-field. Figure 6.13.b and c. depict the shape of the vortex cores. There is a region of inner vorticity and a region of outer vorticity produced by the aeroramp. The iso-surfaces show the increased surface area in the aeroramp plume.

The rotational behavior of the plume can be seen in Figure 6.14. The figure depicts three-dimensional streamlines from three different viewpoints. The first figure with the flow into the page shows the helical behavior of the fuel as it leaves the injector and mixes with the freestream. The majority of the interaction between the four injectors is a result of front injectors impinging upon the rear injectors. The middle picture (birds-eye view) shows how the shape of the plume changes between the first set of injectors and the second set. There is a low pressure region behind the first set of injectors which pulls the freestream fluid back towards the rear set of injectors. This fluid then bends around both sides of the rear injectors. The low pressure region also acts as a recirculation region. The freestream flow in front of the injectors separates (which can also be seen in figure on the right) and then expands around the outside of the first injectors before curving back towards the centerline and impinging upon the second set of injectors. The second line of injectors gives the aeroramp injector more penetration as can bee seen by the streamlines in the figure on the right.

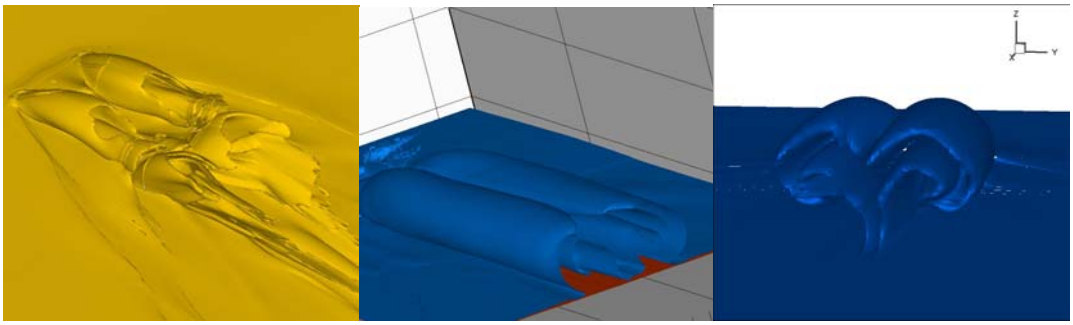

a. ω = 800,000 /sec **b. ω =50,000 /sec** **c. ω =150,000 /sec**

Figure 6.13 Iso-Surfaces of the aeroramp injector for various vorticity

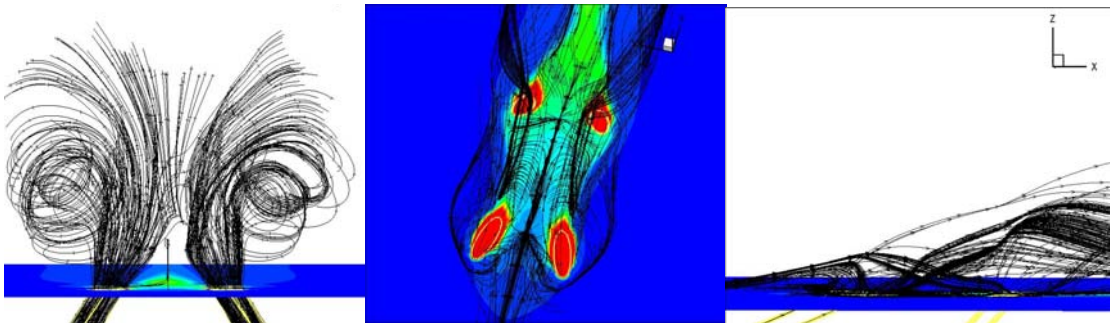

(a) y-z plane, flow into page (b) x-y plane, birds-eye view (c) x-z plane, flow left to right

Figure 6.14 3D Momentum streamlines emanating from fuel jet.

Two-dimensional streamlines are overlaid on vorticity contours for 6 different downstream locations in Figure 6.15. Figure 6.15 (a) shows two regions on either side of the centerline of opposite sense rotation. The different rotation directions seen in Figure 6.15(a) are a result of the vorticity produced from the front injectors interacting with the vorticity produced by the rear injectors. Looking at just the left hand side of that contour, the upper portion of streamlines rotates clockwise and the lower portion rotates counter-clockwise. As the flow proceeds downstream, the vorticity is summed (because of the vector nature of vorticity) and a strong CVP is created, Figure 6.15(d-f).

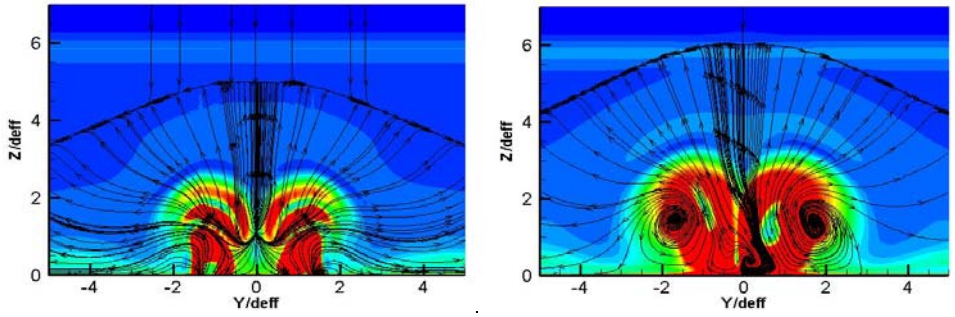

(a) $x/d_{eff} = 2$ **(b)$x/d_{eff} = 4$**

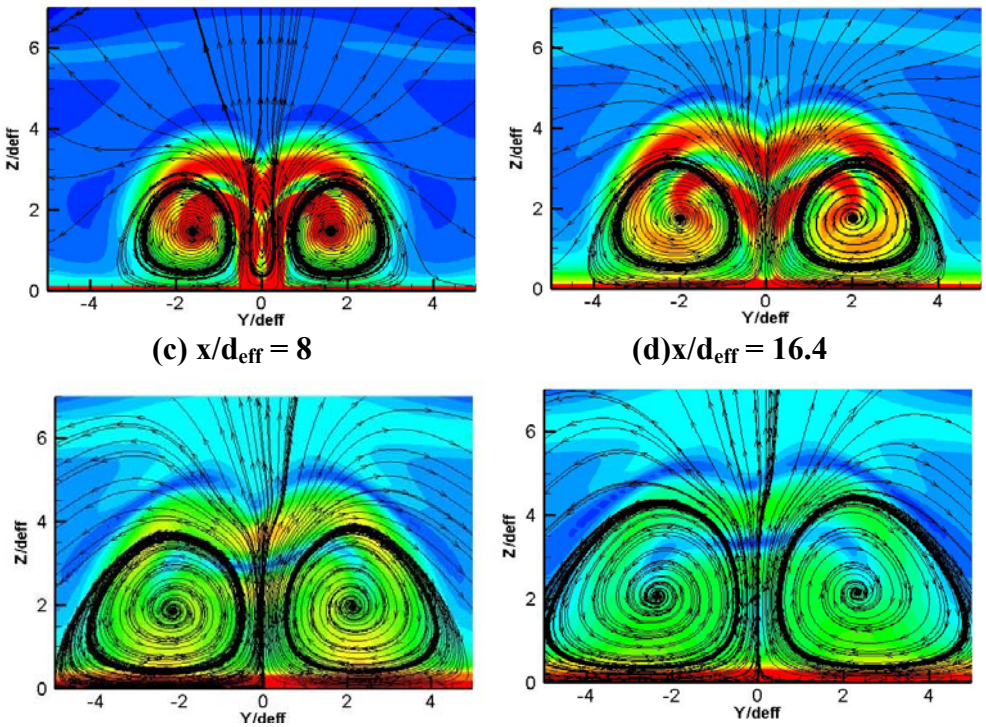

(c) $x/d_{eff} = 8$ (d) $x/d_{eff} = 16.4$

(e) $x/d_{eff} = 24$ (f) $x/d_{eff} = 32$

Figure 6.15 Contours of vorticity overlaid with streamlines for the aeroramp injector. Slices in the y-z plane at various x/d_{eff} locations.

6.1.7 Parametric Variation in Mass Flow for the Aeroramp Injector

The CFD analysis assumed constant and equal mass flow through each of the four injector orifices in the aeroramp injector. However in the experiment, the total mass flow was known only before the helium entered each injector feed tube. The mass flow could have been unevenly distributed into the four injector feed tubes. Additional CFD analyses were conducted with varying mass flow between the front and rear sets of injectors in order to determine the effect, if any, on the numerical predictions. The overall total mass flow remained constant among the analyses.

For the first analysis, twice as much mass flow was injected through the front injectors as through the rear set of injectors. This case will be designated “more-front” case. The second analysis injected twice as much mass flow through the rear set of injectors as through the front set; this case is designated, “more-rear” case.

Downstream progression plots of maximum helium concentration, mixing efficiency and plume center of mass are show in Figure 6.16 and Figure 6.17. The maximum helium concentration is larger for the "more-rear" case with the largest difference occurring closest to the injection point. The equal mass flow and the "more-front" case have similar maximum helium concentration values throughout the domain. The "more-front" case has a slightly lower concentration until 25 effective diameters. Past 25 effective diameters, all three cases have similar maximum concentration values. The mixing efficiency downstream progression displays similar trends to the helium concentration. The "more-rear" case has the lowest mixing efficiency throughout the domain while the "more-front" case and the equal mass flow case behavior more similar. The equal mass flow case has better mixing efficiency past 18 effective diameters but is accompanied by the smallest penetration into the freestream. The "more-front" case has the highest penetration. All three cases exhibit a large increase in penetration of the center of mass of the plume between 4 and 6 effective diameters. This is a result of the penetration increased caused by the second set of injectors.

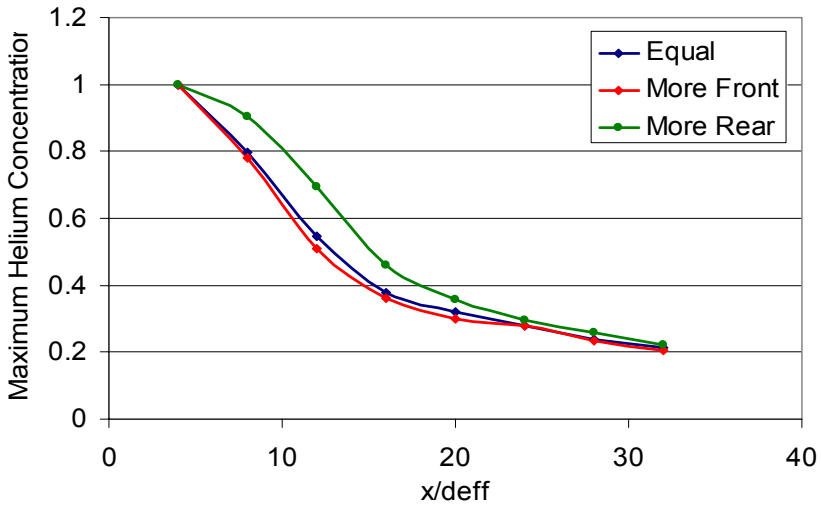

Figure 6.16 Downstream progression of maximum helium concentration for the aeroramp injectors with varying massflow.

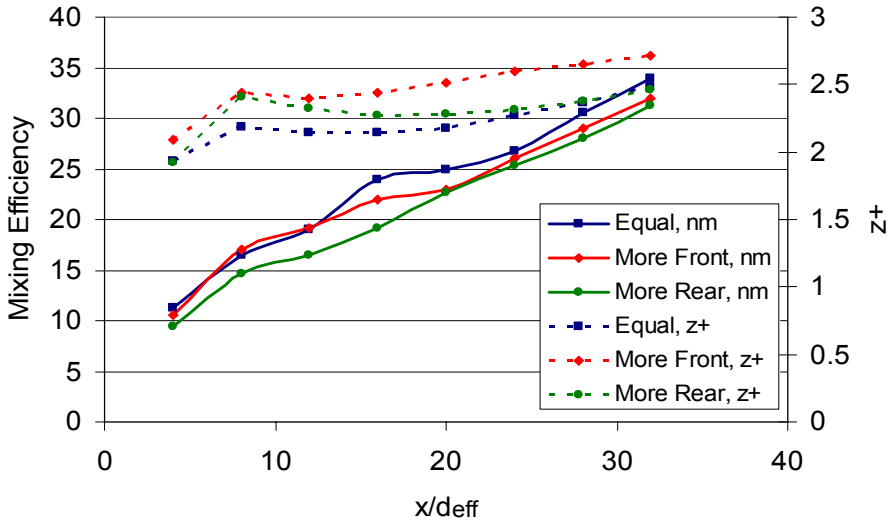

Figure 6.17 Downstream progression of mixing efficiency and plume center of mass for the aeroramp injectors with varying massflow.

The results found in Table 6-3 show that more mass flow through the front set of injectors improves mixing slightly over the original aeroramp predictions with equal mass flow through each injector orifice. The plume size is similar for the equal mass flow case and the "more-front" case but the "more-front" case has a smaller plume width which agrees better with experiment. The "more-rear" case penetrates the least vertically and has the highest plume center of mass. The plume size and center of mass are over-predicted for all three cases when compared to the experiment. The maximum concentration is lowest for the "more-front" case and largest for the case with "more-rear" case. The mixing efficiency parameter produced by the "more-front" case agrees with the experimental results. The total pressure loss parameter is similar for all three cases and the experiment.

Table 6-3 Integrated parameters for the parametric study of mass flow through the aeroramp injectors.

		Experiment	CFD		
			Equal	More Front	More Rear
Plume Width	**$y\pm$**	**7.90**	**8.15**	**8.02**	**8.54**
Maximum Plume Height	**z_{max}**	**4.50**	**4.64**	**4.69**	**4.49**
Plume Center of Mass	**z^{+}**	**2.00**	**2.14**	**2.44**	**2.27**
Maximum Concentration	**σ_{max}**	**0.34**	**0.35**	**0.33**	**0.46**
Mixing Efficiency	**η_m**	**0.22**	**0.24**	**0.22**	**0.19**
Total Pressure Loss Parameter	**Π**	**0.40**	**0.41**	**0.40**	**0.41**

Changing the mass flow rate through the injector orifices alters the behavior and mixing of the plume. This can be seen in the helium mass fraction contours found in Figure 6.18 and Figure 6.19. Better mixing is achieved with more of the injected mass flowing through the front set of injectors. As the injected fuel from the front injectors impinges upon the weak shock produced by the second set of injectors, it is lifted away from the surface and around the rear injectors. This interaction causes the flow to become unstable and turbulent which aids turbulent mixing. With more fuel mass injected through the aft injectors, the fuel center of mass is lower because of the lower injection angle and because the fuel is now not lifted off the surface by additional injectors like the "more-front" case. The majority of the injected fuel also does not encounter a second bow shock.

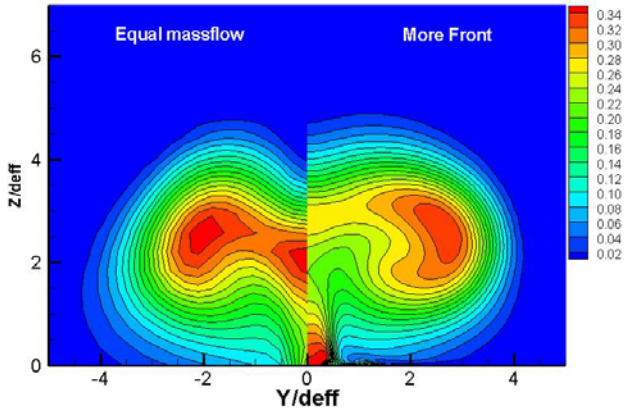

Figure 6.18 Helium mass fraction contour for equal mass flow out of each orifice and more mass flow from the front set of injectors for the aeroramp injector.

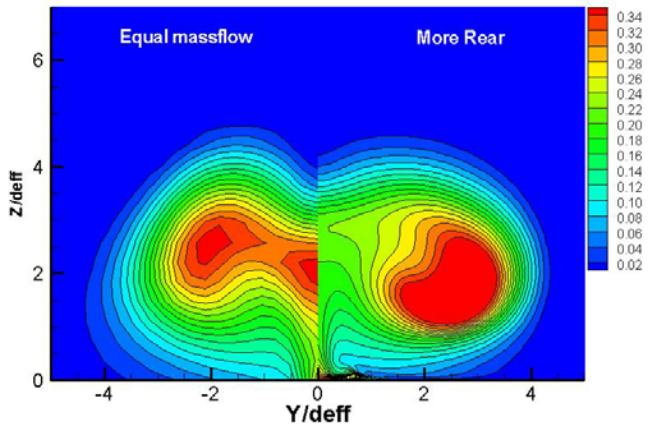

Figure 6.19 Helium mass fraction contour for equal mass flow out of each orifice and more mass flow from the rear set of injectors for the aeroramp injector.

6.2 Aligned Diamond Injector

Modifications to the Baseline design based on geometric methods were made. The single, round-hole Baseline injector was compared to a single diamond-shaped transverse injector with larger area and lower injection pressure to maintain the same mass flow rate as the Baseline injector. Comparisons to the experimental results and the Baseline predictions were made and are discussed below. The predictions include the following: mass concentration, mixing, total pressure loss, total temperature, Mach number and vorticity. All integrated quantities were defined above.

The effective injector diameter, d_{eff}, was used previously to normalize the Baseline and aeroramp injector predictions. However, the diamond and Baseline injectors have different orifice shapes and areas. The diamond injector predictions cannot be normalized by the same d_{eff}. Therefore, a different length scale was used for the diamond injector and for the Baseline injector predictions presented in the section. The length scale used is the effective radius, R_b, defined by[78]:

$$R_b = \sqrt{\frac{G_j}{\rho_\infty u_\infty}} \qquad \textbf{6-1}$$

Where G_j is the injector mass flow rate, ρ_∞ is the freestream density and u_∞ is the freestream velocity. R_b is equivalent to 3.383 mm and the experimental measurement plane corresponds to $x/R_b = 15.6$.

Typically, diamond shaped injectors are designed to have a low momentum flux ratio for optimal penetration (for example, $\bar{q} = 0.5$). Tomioka[78] and Grossman[79] showed that testing at a lower momentum flux ratio diamond injector improved penetration over the equivalent round-hole injector, whereas testing a higher momentum flux ratio injector did not improve penetration. The authors stated that this was a result of the jet rapidly expanding outward and losing the diamond shape and its benefits. The diamond injectors simulated in this study were performed with a momentum flux ratio of $\bar{q} = 1.2$, which is considered a somewhat high value for optimum performance.

6.2.1 Mass Concentration Contours

The diamond injector mass concentration CFD predictions are compared to the experimental results in Figure 6.20. The helium concentration contours are located in the y-z plane $x/R_b = 15.6$ downstream of injection. The plume shape is well predicted by the CFD with a cone-like bump located at the top, centerline of the plume. The lateral penetration is similar with the experiment showing more lateral penetration of fuel on the wall surface across the contour plane. The CFD predicts the plume to lift off the surface. The difference in concentration in the near-wall region could be attributed to differences in the time-averaged CFD analysis and the unsteady behavior of jet injection and the shock structure captured in the experiment. The area of maximum helium concentration comprises a larger region in the experimental results than in the numerical prediction. The maximum regions are similar away from the centerline but the magnitude of helium concentration on the centerline is under-predicted by CFD. The plume cores are located at a further lateral distance away from the centerline for the CFD prediction than for the experimental results.

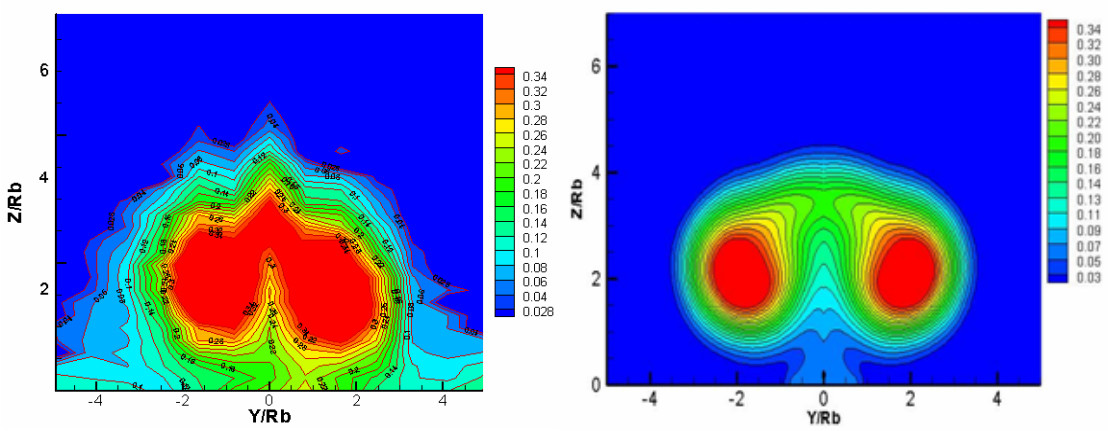

Figure 6.20 Calculated helium concentration contours in the x/R_b=15.6 plane of the diamond shaped injector compared to experiment. The experimental result is on the left and the CFD prediction is on the right.

Helium mass fraction contours in the y-z plane at x/R_b = 15.6 for the Baseline injector and the aligned diamond injector are compared to each other in Figure 6.21. The vertical penetration is similar for the two contours, but the diamond injector has more lateral penetration. The diamond injector has two distinct regions of high concentration helium on either side of the centerline. The regions of high fuel concentration for the Baseline injector are closer to the centerline than the diamond injector cores. The diamond injector mixes better on the centerline of the plume than the Baseline injector. The Baseline injector predicts a smaller region of high concentration fuel than the diamond injector.

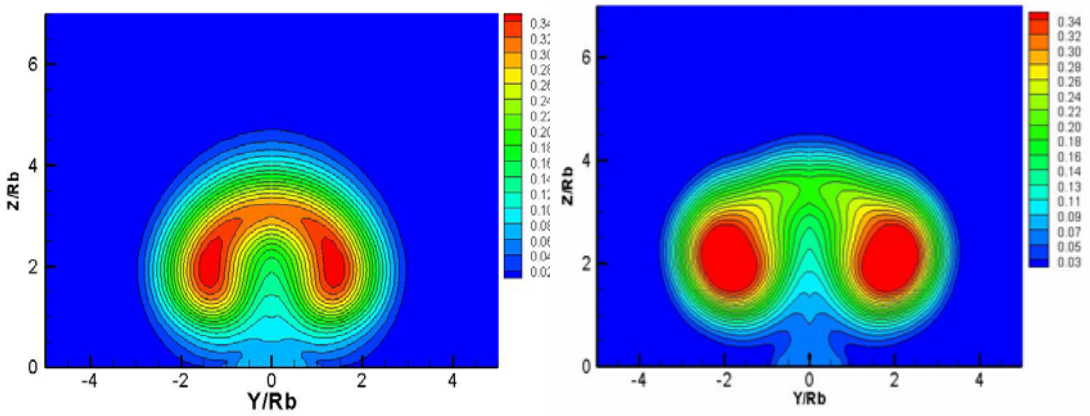

Figure 6.21 Calculated helium concentration contours in the x/R_b=15.6 plane for the Baseline and aligned diamond injectors. The Baseline injector is on the left and the diamond injector is on the right.

Helium mass fraction contours at $x/R_b = 27.8$ comparing the Baseline and aligned diamond injectors can be found in Figure 6.22. Note that the contour levels are not the same as the $x/R_b = 15.6$ contours. In order to better see the shape of the mass fraction in the plume at 27.8 effective radii, the mass fraction levels were lowered. The largest change in plume size with downstream progression for the diamond injector is in the vertical direction. The Baseline injector expands both laterally and vertically. The lateral penetration does not change for the diamond injector at 27.8 effective radii compared to 15.6 effective radii. The maximum concentration is higher for the Baseline injector at $x/R_b = 27.8$. The remainder of the concentration levels in the jet are similar for the two injectors.

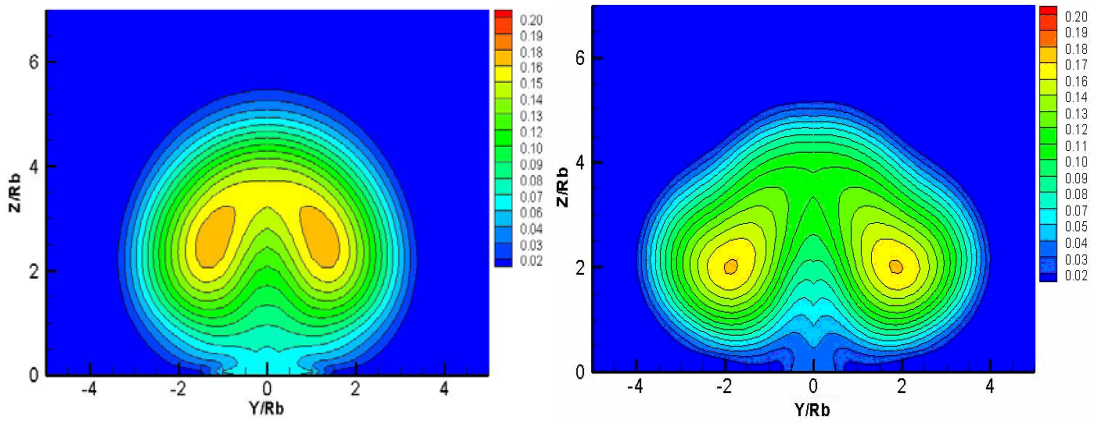

Figure 6.22 Calculated helium concentration contours in the x/R_b=27.8 plane for the Baseline and aligned diamond injectors. The Baseline injector is on the left and the diamond injector is on the right.

6.2.2 Total Temperature Ratio Contours

The total temperature contours in the y-z plane at $x/R_b = 15.6$ for the diamond injector are compared to experiment in Figure 6.23. The total temperature was normalized by the freestream total temperature, 295 K. The CFD predicts a similar shape with a peak near the top centerline of the plume, but the magnitude of total temperature at this location is not predicted by the numerical analysis. The CFD predicts a much lower total temperature plume with a smaller overall area. The CFD contour also shows the total temperature gradient produced by the boundary layer. Both contours show a region of low total temperature on the centerline of the plume.

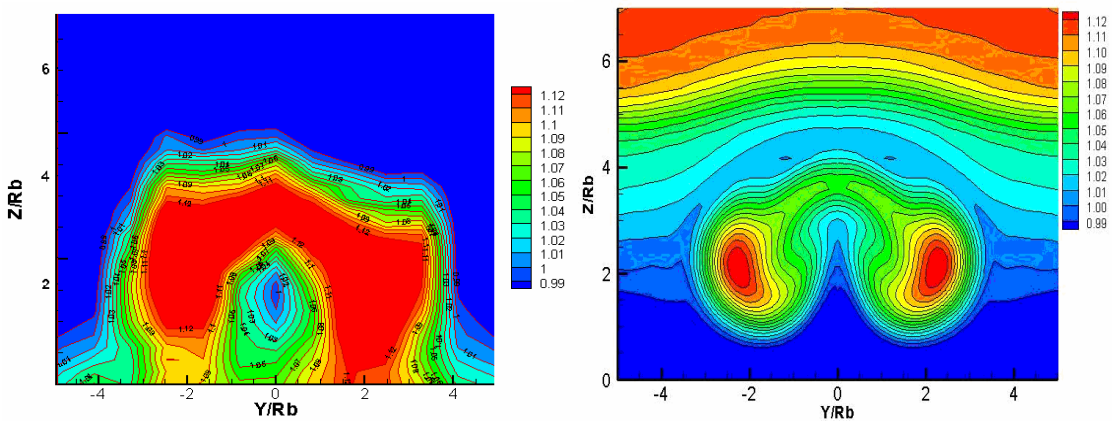

Figure 6.23 Predicted normalized total temperature ratio in the y-z plane at x/R_b =15.6 for the diamond injector. The experimental result is on the left and the CFD prediction is on the right.

Comparisons of the total temperature ratio contours for the Baseline injector and the diamond injector can be found in Figure 6.24. The diamond injector produces a higher total temperature core than the Baseline injector as predicted for both the CFD and the experimental results. The Baseline injector has a lower total temperature region away from the plume near the vertical boundary of the contour. The diamond injector produces two regions of high total temperature on either side of the centerline with a low total temperature region in the middle. Both contours show the horse-shoe like shape of the CVP, but the diamond injector has a larger distance in between the vortex cores.

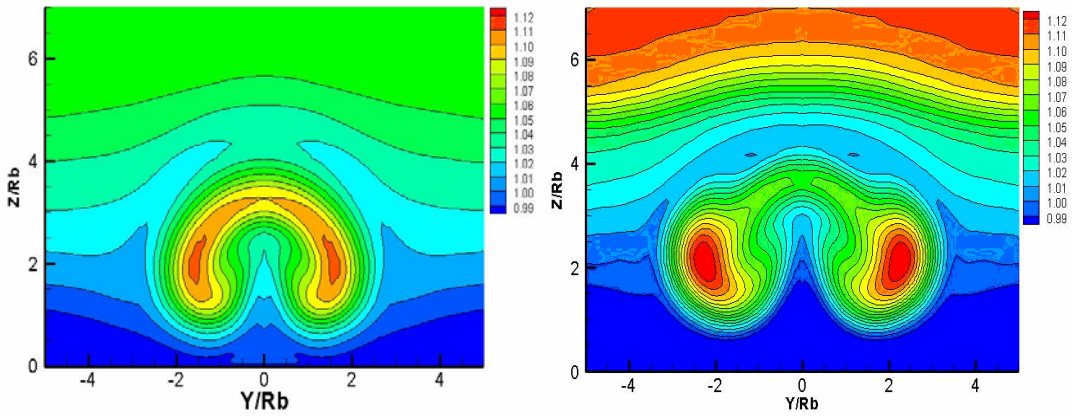

Figure 6.24 Calculated total temperature ratio contours in the x/R_b =15.6 plane for the Baseline and aligned diamond injectors. The Baseline prediction is on the left and the aligned diamond prediction is on the right.

6.2.3 Mach Number Contours

The Mach number contours for the diamond injector in the y-z plane at x/R_b = 15.6 are compared to the experiment in Figure 6.25. The contours are similar in shape, but differ in magnitude of the cores. Both contours show approximately the same vertical penetration but, the CFD analysis predicts a wider plume. The plume core is moving more quickly in the prediction than in the experimental results. The freestream fluid away from the plume is moving at similar speeds for both contours. The presence of a CVP can be seen in both contours by the dips produced on the outer edges of the plumes.

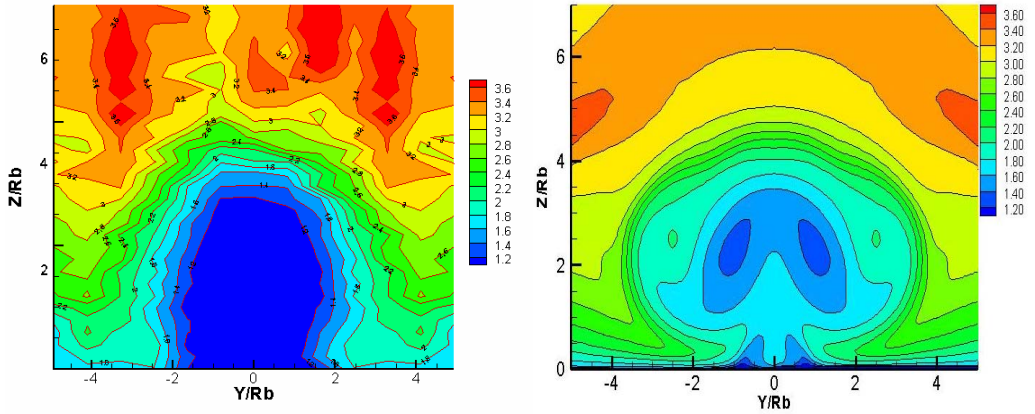

Figure 6.25 Calculated Mach number contours in the x/R_b =15.6 plane of the aligned diamond injector. The experimental result is on the left and the CFD prediction is on the right.

The CFD Mach number predictions for the diamond injector compared to the Baseline injector at 15.6 effective radii can be found in Figure 6.26. The diamond injector has a wider region of low-speed fluid than the Baseline injector and the magnitude of that fluid is smaller. The fluid away from the plume is moving slower in the diamond injector contour than in the Baseline injector contour. This could be an outcome of the different shock strengths produced by injection from two orifices of different shape. The small difference in speed of the freestream air behind the shocks would also affect the speed of the jet plume.

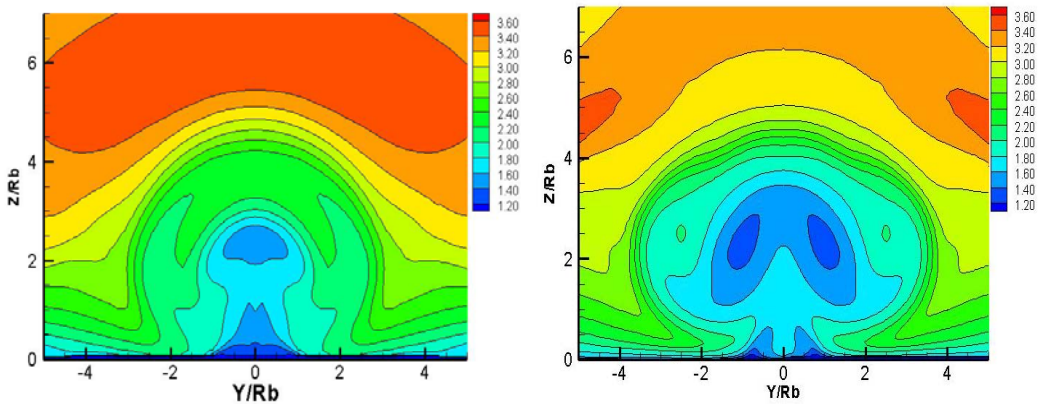

Figure 6.26 Comparison of calculated Mach number contours in the x/R_b =15.6 plane for Baseline and aligned diamond injectors.

6.2.4 Total Pressure Ratio Contours

The predicted total pressure was normalized by the freestream total pressure and can be found in Figure 6.27. The predictions for the diamond injector are compared to the normalized total pressure ratio. Previously, the aeroramp and Baseline injectors were compared to the experimental Pitot pressure contours. Only the total pressure contour for the experimental results was available for comparison with the CFD predictions for the diamond injector. The contours slices in the y-z plane were taken at x/R_b = 15.6. There is good agreement between the CFD and the experiment. The low total pressure ratio region has a similar shape and magnitude for both contours.

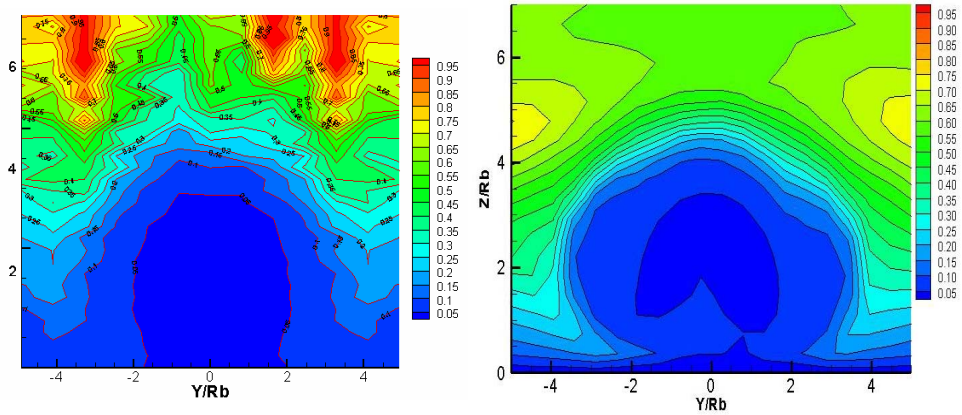

Figure 6.27 Normalized total pressure ratio in the y-z plane at x/R_b =15.6 plane of the aligned diamond injector. The experimental result is on the left and the CFD prediction is on the right.

Normalized total pressure contour comparisons for the Baseline injector and the aligned diamond injector in a y-z plane at 15.6 effective radii can be found in Figure 6.28. The magnitude of the total pressure ratio in the plumes is similar for the two predictions which indicate similar losses.

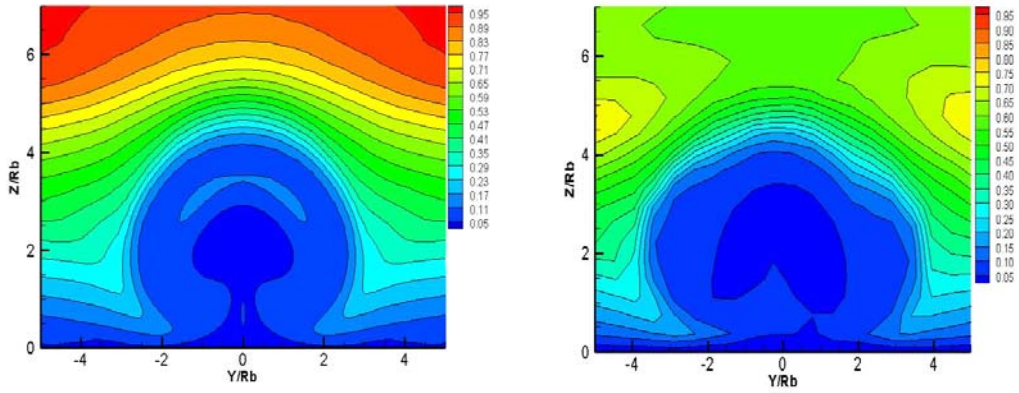

Figure 6.28 Normalized total pressure ratio in the y-z plane at x/R_b =15.6 comparing the Baseline injector and the aligned diamond injector. The Baseline injector is on the left and the diamond injector is on the right.

6.2.5 Plume Characteristics and Integrated Parameters

The mixing efficiency and plume center of mass for the diamond injector at several downstream locations is compared to the Baseline injector in Figure 6.29. Keep in mind that in this section the data used for Baseline injector integrated parameters were normalized by $R_{b,}$ not d_{eff} (as in Chapter 5). The change in the normalization method affects the plume width, maximum plume height and plume center of mass. The mixing efficiency is similar for the two analyses with the diamond injector predicting less mixing between 14 and 20 effective radii. The penetration of the center of mass for the two injectors is very comparable near the injector however, farther downstream the Baseline injector is predicted to have a higher center of mass.

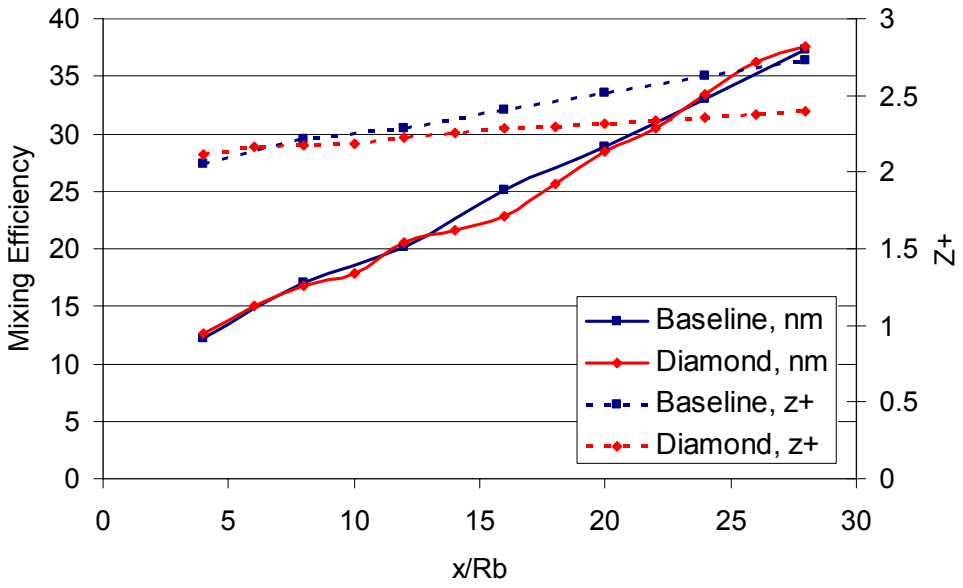

Figure 6.29 Downstream progression of mixing efficiency and plume center of mass for the diamond injector compared to the Baseline injector.

The results and predictions of the integrated parameters for the aligned diamond injector can be found in Table 6-4. The width and height of the plume is under-predicted by approximately 0.50 effective radii and 0.53 effective radii respectively by the CFD. The predicted center of mass of the plumes at 15.6 effective radii agrees well with the experimental results, differing by 0.19 effective radii. The CFD predicts a smaller maximum helium concentration and a mixing efficiency that is higher than the experimental results. The total pressure loss parameter is smaller than the experimental results, but not significantly.

Table 6-4 Plume characteristics and integrated parameters for the aligned diamond injector compared to the Baseline injector at 15.6 effective radii downstream from injection.

		Diamond Injector	
		Experiment	CFD
Plume Width	$y\pm$	**7.80**	**7.30**
Maximum Plume Height	z_{max}	**5.00**	**4.47**
Plume Center of Mass	z^{+}	**2.10**	**2.29**
Maximum Concentration	σ_{max}	**0.57**	**0.38**
Mixing Efficiency	η_m	**0.18**	**0.22**
Total Pressure Loss Parameter	Π	**0.29**	**0.32**

The CFD predictions at 27.8 effective radii can be found in Table 6-5. The diamond injector predictions are also compared to the Baseline injector predictions. The diamond injector has a larger plume width than the Baseline injector by 1.65 effective radii, but the Baseline injector is predicted to have a larger increase in plume width from 15.6 to 27.8 effective radii. The Baseline injector penetrates slightly further vertically than the diamond injector, but the plume center of mass is higher for the diamond injector at 16.4 effective radii. The experimental results showed similar trends, the maximum plume height and center of mass for the diamond injector did not improve over the Baseline injector at this momentum flux ratio.

The diamond-shaped injector predicts a higher maximum concentration than the Baseline injector with slightly less mixing efficiency. The changes from 15.6 to 27.8 effective radii were similar for both injector configurations. The Baseline injector has a higher total pressure loss parameter at both downstream locations which is a result of the higher losses incurred across the bow shock in front of the Baseline injector as opposed to the losses from the oblique shock off the leading edge of the diamond injector. In addition, the separation region present upstream of the Baseline injector does not exist ahead of the diamond injector.

Table 6-5 Plume characteristics and integrated parameters for the diamond injector at 27.8 effective radii downstream from injection

		CFD Baseline Injector		CFD Diamond Injector	
x/R_b location		**15.6**	**27.8**	**15.6**	**27.8**
Plume Width	**$y\pm$**	**5.65**	**6.48**	**7.30**	**7.71**
Maximum Plume Height	**z_{max}**	**4.58**	**5.33**	**4.47**	**5.04**
Plume Center of Mass	**z^+**	**2.15**	**2.81**	**2.29**	**2.42**
Maximum Concentration	**σ_{max}**	**0.35**	**0.17**	**0.38**	**0.17**
Mixing Efficiency	**η_m**	**0. 23**	**0.37**	**0.22**	**0.39**
Total Pressure Loss Parameter	**Π**	**0.40**	**0.46**	**0.32**	**0.41**

6.2.6 Vorticity

The vorticity contours at x/R_b = 15.6 and x/R_b = 27.8 in the y-z plane for the diamond injector can be found in Figure 6.30. The diamond injector has several regions of high vorticity surrounded by areas of lower vorticity. There is a low vorticity region located vertically on the centerline of the plume and there is an arch-shaped region across the top bump of the plume. These areas are surrounded by flow with faster rotation. A CVP has been formed from injection through the diamond shaped orifice. The vortex pair pulls freestream air into the plume and then pushes the shear layer up the centerline away from the surface. It is then rotated away from the centerline while entraining more air. The diamond injector produces a vortex pair that is farther apart laterally than the Baseline injector. The large region between vortex cores encourages mixing of the fuel with the freestream air. As the fluid progresses downstream, more air is entrained in the plume and mixing is increased. At 27.8 effective radii the majority of the vorticity is present in the bottom portion of the plume in two upside-down horseshoe shapes.

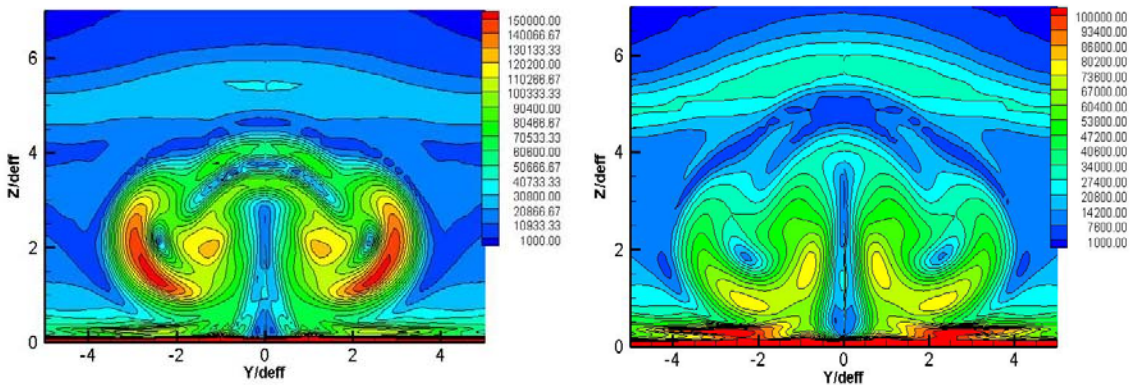

Figure 6.30 Predicted vorticity ratio in the x/R_b =15.6 plane on the left and x/R_b =27.8 plane on the right of the aligned diamond injector.

Vorticity contours of the Baseline and aligned diamond injectors at x/R_b = 15.6 are compared in Figure 6.31. The Baseline injector has stronger vorticity in the plume than the diamond injector. The diamond injector has a larger area of high-low vorticity interfaces than the Baseline injector. These areas aid in the mixing of the fuel and air.

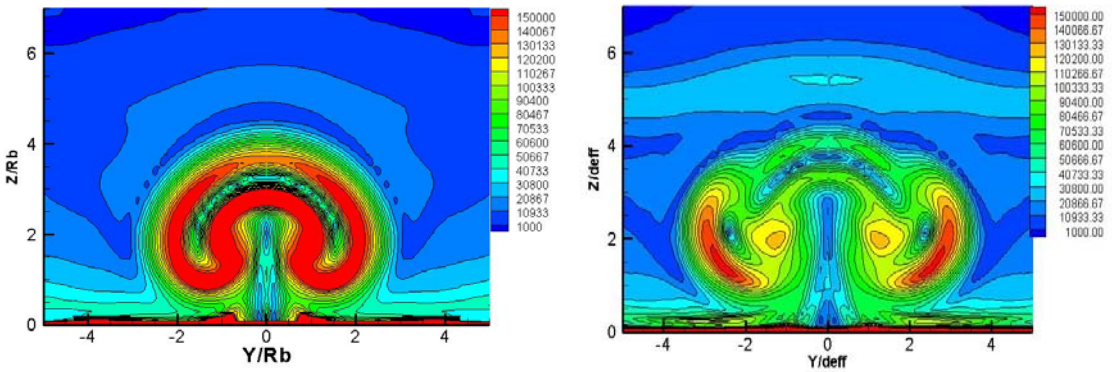

Figure 6.31 Predicted vorticity of the Baseline and aligned diamond injector in the x/R_b =15.6 plane. The Baseline prediction is on the left and the aligned diamond prediction is on the right.

Figure 6.32 pictures a constant vorticity iso-surface for the aligned diamond injector. The most interesting part of this figure is the three surface "bumps" created by the injection. Flow injected from the front tip of the injector produces the middle bump and the interaction of the fuel injected from the sides and the freestream air produces the outside bumps. The compression shock created by the sharp edge of the diamond shape changes the direction of the in-coming flow on either side of the injector. The flow leaving the front end of the injector has an initial rotation that is separate from the CVP.

The contrast in surface allows for a large shear layer and added vorticity on the upper portion of the centerline of the plume.

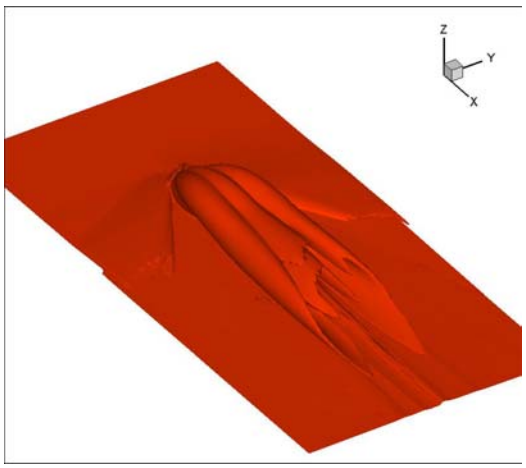

ω =150,000 /sec

Figure 6.32 3D vorticity iso-surface of the aligned diamond injector

Vorticity contours overlaid with streamlines for several y-z planes can be found in Figure 6.33. The CVP is not fully developed until 15.6 radii downstream. The initial vortex pair is very unstable, which is good for large-scale, turbulent mixing. The unstable fuel-flow is "stirred" with the freestream air. At $x/R_b = 4$, a small vortex can be seen on the centerline of the contour. The small vortex is produced by the rotation of the fuel leaving the forward end of the injector. It eventually becomes part of the larger vortex pair as the flow progresses downstream and the CVP becomes stronger and more stable.

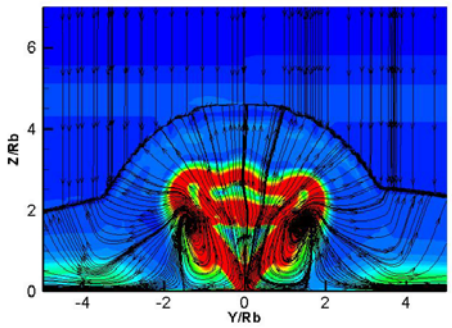

(a) $x/R_b = 2$

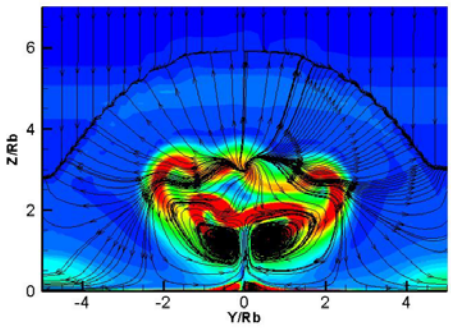

(b) $x/R_b = 4$

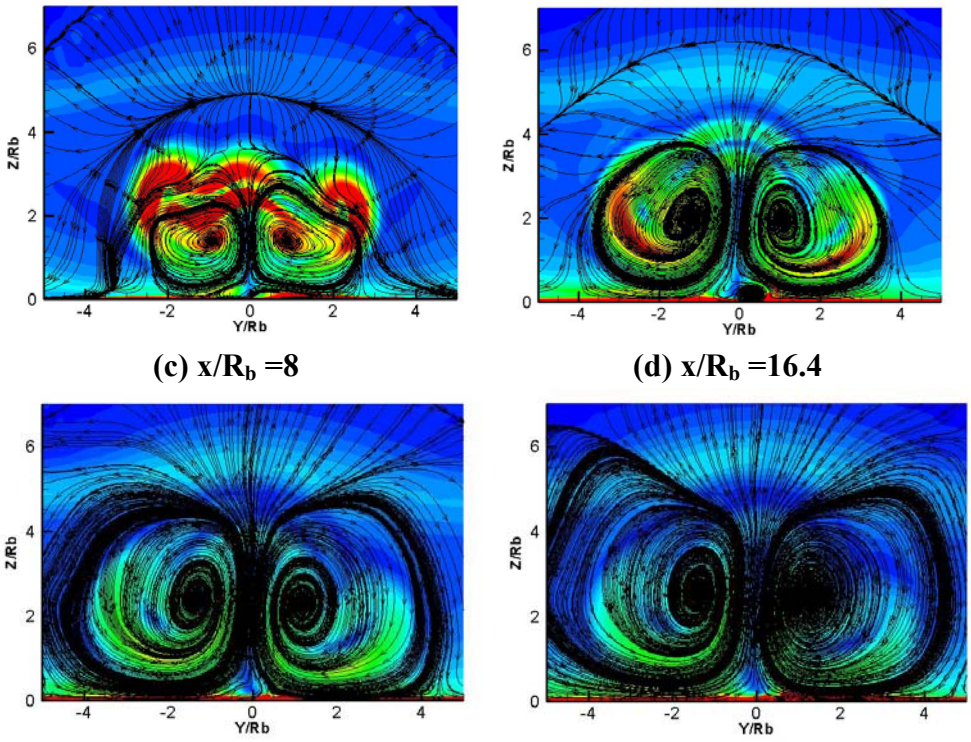

(c) x/R_b =8 **(d) x/R_b =16.4**

(e) x/R_b = 24 **(f) x/R_b = 32**

Figure 6.33 Contours of vorticity overlaid with streamlines for the aligned diamond injector. Slices in the y-z plane at various x/R_b locations.

The freestream flow does not separate off the leading edge but instead, separates from the sides of the diamond. It then reattaches at the aft end of the injector (Figure 6.34a). The flow immediately behind behaves similarly to the flow behind a wing on an airplane. There is a recirculation region aft of the injector, which can be seen in Figure 6.34 (c). The lower pressure region behind the injector pulls the streamlines back towards the centerline where the flow from either side meets. The resultant vortex shedding aids in turbulent mixing. Some of the fuel injected from the forward end and down the centerline of the diamond injector does not enter into the CVP as seen in Figure 6.34(a). The streamlines emanating from the sides (both the expansion and compression) rotate into the vortices that form the CVP. They encounter not only a change in pressure caused by the expansion from injection but also the changes in pressure created by the diamond shape. The diamond injector, in this situation, produces good initial mixing which is dominated by the large-scale mixing of the fuel-air process. As the air is entrained within

the fuel plume the shear layer increases. The increase in interfacial area causes mixing through molecular diffusion to occur.

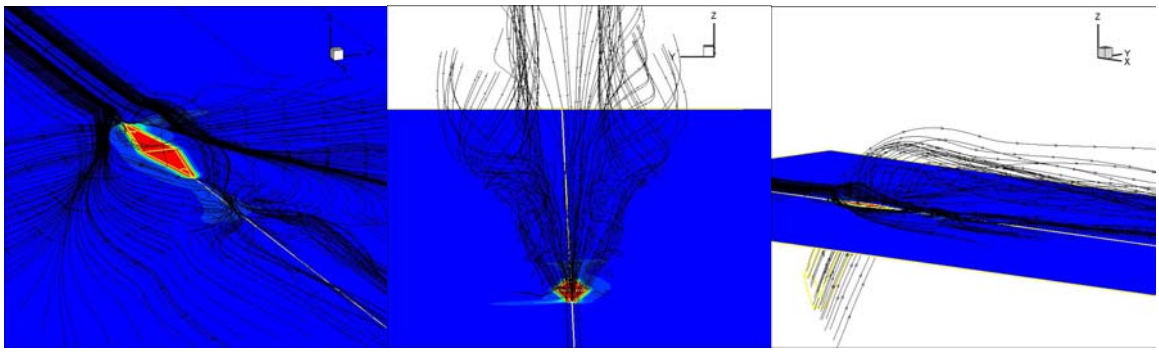

(a)flow is upper left to lower right (b) flow directly into page (c) flow left to right

Figure 6.34 3D momentum streamlines for the aligned diamond injector.

6.3 Yawed Diamond Injector

The aligned diamond was rotated 15° about the vertical axis so that the approach flow encounters a yawed diamond injector. The yawed diamond injector is compared to the single round Baseline injector in this section. Comparisons to the experimental results are also made. The predictions include the following: mass concentration, mixing, total pressure loss, total temperature, Mach number and vorticity. All integrated quantities were defined above.

Similar to the aligned diamond injector, the effective injector diameter, d_{eff}, will not be used to normalize the predictions. Instead, the effective radius, R_b, will be used for the yawed diamond injector and for the Baseline injector predictions presented in the section.

6.3.1 Mass Concentration Contours

The helium concentration contours of the 15° yawed diamond injector can be found in Figure 6.35. The contours are slices in the y-z plane located $x/R_b = 15.6$ downstream from the injection point. The general shape of the plume is predicted by the CFD analysis but the magnitude is not predicted as well. The CFD analysis predicts a smaller region of high helium concentration. The experiment penetrates farther in the

vertical direction and shows helium to be present near the wall surface across the contour. Both plumes are asymmetric with highest penetration off-center. Both plumes also spread further laterally from the center on the side opposite to the highest vertical penetration. The CFD contour has a horse-shoe like shape but is larger on one side.

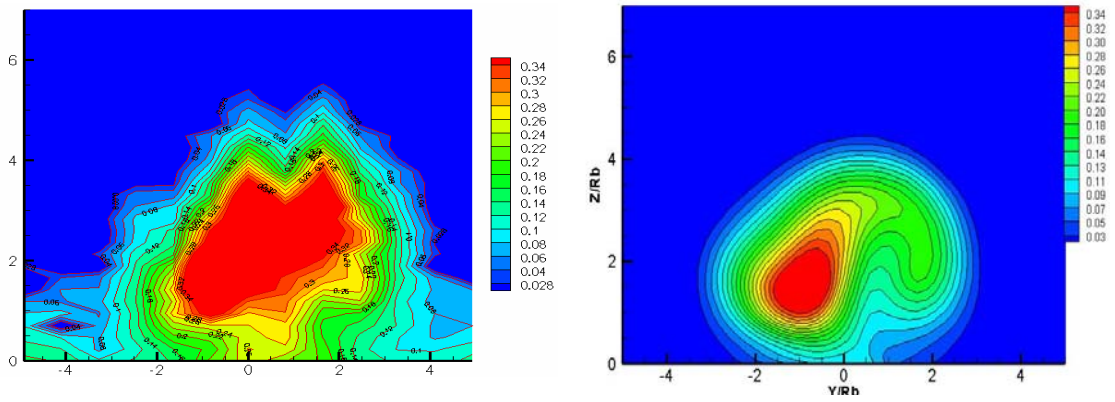

Figure 6.35 Calculated helium concentration contours in the x/R $_b$ =15.6 plane of the 15° yawed diamond injector compared to experiment. The experimental result is on the left and the CFD prediction is on the right.

CFD prediction contours of helium mass fraction in the y-z plane at x/R $_b$ = 15.6 for Baseline injector and the yawed diamond are compared to each other in Figure 6.36. The Baseline injector and the yawed diamond injector have similar plume areas. The Baseline injector lifts away from the surface better than the plume from the yawed diamond injector. The yawed diamond injector has a larger area of lower helium mass fraction than the Baseline injector and the contours show slightly better mixing than the Baseline contour because of the plume overall has a larger region of low concentration at this downstream location.

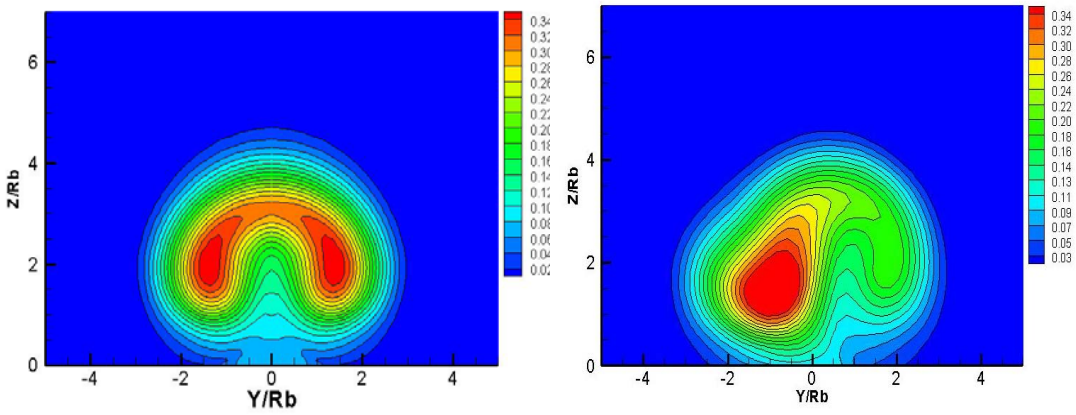

Figure 6.36 Calculated helium concentration contours in the x/R$_b$ =15.6 plane for the Baseline and yawed diamond injectors. The Baseline injector is on the left and the yawed diamond injector is on the right.

CFD predicted contours of helium mass fraction at x/R$_b$ = 27.8 for the Baseline and yawed diamond injector configurations can be found in Figure 6.37. Note that the contour levels are not the same as the x/R$_b$ = 15.6 contours. To better see the shape of the mass fraction in the plume at 27.8 effective radii, the mass fraction levels were lowered. Similar to the aligned diamond injector, the yawed diamond plume does not change in the lateral spreading but the vertical penetration is increased with downstream progression. The yawed diamond injector has a higher helium concentration than the Baseline injector at this downstream location. Better mixing is achieved by the Baseline injector at this downstream location. This could indicate that the Baseline injector has better small-scale mass diffusion behavior than the yawed diamond injector.

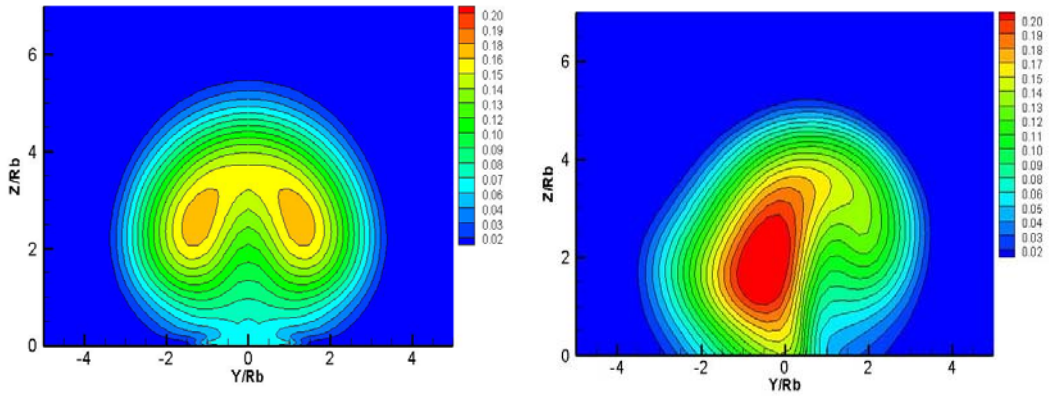

Figure 6.37 Calculated helium concentration contours in the x/R$_b$ = 27.8 plane for the Baseline and yawed diamond injectors. The Baseline injector is on the left and the yawed diamond injector is on the right.

6.3.2 Total Temperature Contours

The total temperature contours in the y-z plane at $x/R_b = 15.6$ for the diamond injector are compared to experiment in Figure 6.38. The total temperature was normalized by the freestream total temperature. The normalized total temperature contours for the CFD and for the experiment are different in magnitude and shape. The large difference could be attributed to the boundary layer definition of the in-coming flow. The boundary layer height was known and the profile was approximated based on turbulent boundary layer methods. The experiment shows a very large region of high total temperature that extends approximately 6 effective radii vertically. The CFD predicts a smaller plume shape that does not extend as high in the z/R_b direction. The CFD predicts a lower total temperature ratio throughout the entire plume region than the experiment shows.

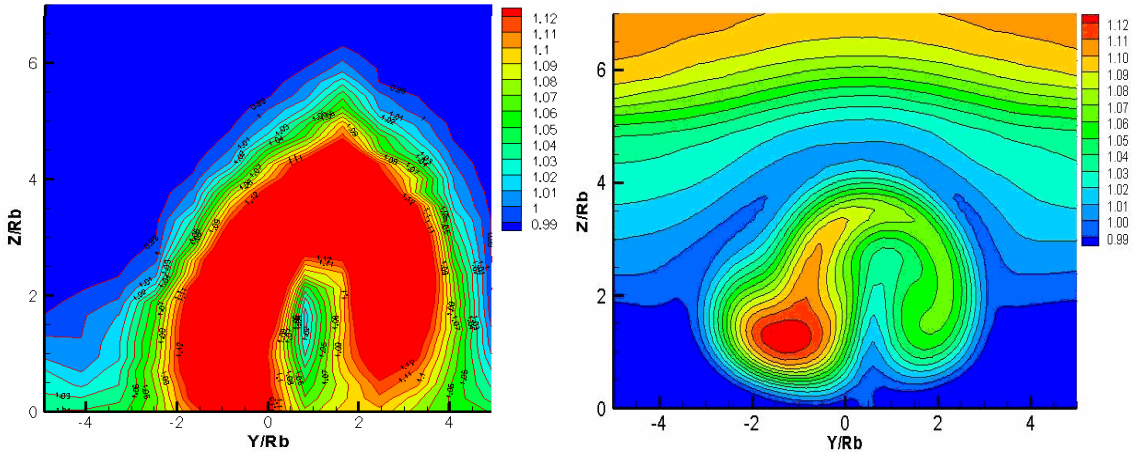

Figure 6.38 Predicted normalized total temperature ratio in the $x/R_b = 15.6$ plane of the yawed diamond injector. The experimental result is on the left and the CFD prediction is on the right.

Comparisons of the total temperature ratio contours for the Baseline injector and the yawed diamond injector can be found in Figure 6.39. The yawed diamond prediction shows a larger region of high total temperature than the Baseline prediction. This region is at a higher magnitude than the Baseline. There is a higher total temperature region at the top of the contour of the yawed diamond similar to the contour of the aligned diamond.

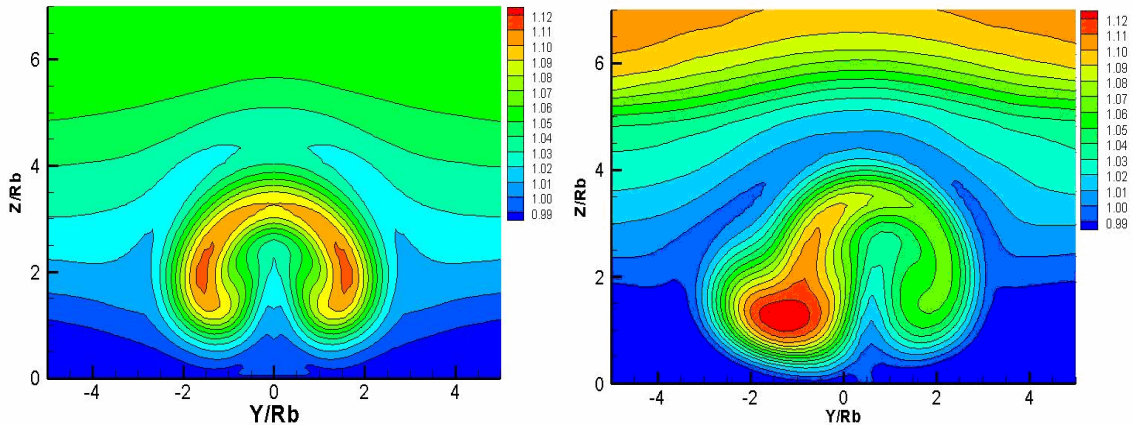

Figure 6.39 Calculated total temperature ratio contours in the x/R_b = 15.6 plane for the Baseline and yawed diamond injectors. The Baseline prediction is on the left and the yawed diamond prediction is on the right.

6.3.3 Mach Number Contours

The predicted Mach number contour for the yawed diamond injector in the y-z plane at x/R_b = 15.6 is compared to experiment in Figure 6.40. There is good agreement for the shape of the plume between the experiment and CFD, and the CFD is able to predict the vertical penetration of the plume. Similar to the aligned diamond injector, the region of slow moving fluid is larger for the experiment.

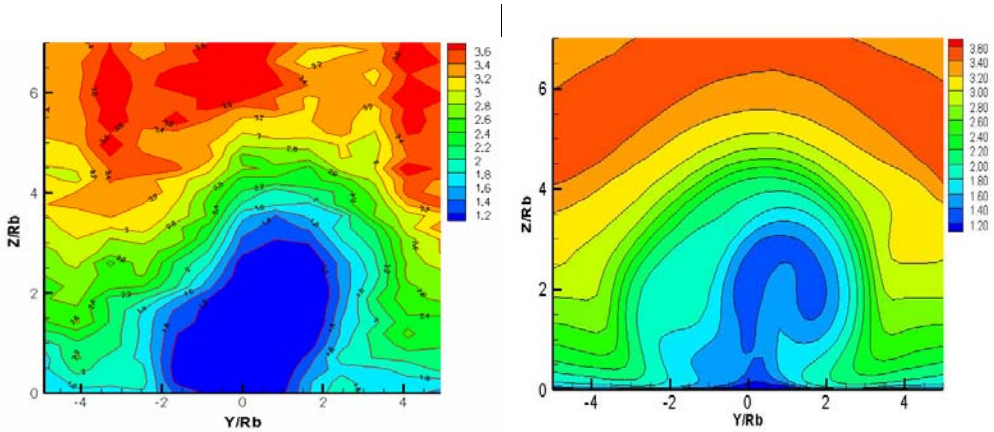

Figure 6.40 Calculated Mach number contours in the x/R_b =15.6 plane of the yawed diamond injector. The experimental result is on the left and the CFD prediction is on the right.

The Mach number CFD predictions for the yawed diamond injector compared to the Baseline injector at 15.6 effective radii can be found in Figure 6.41. The yawed

diamond injector has a slower moving core than the Baseline prediction which is consistent with the experimental results. The Mach numbers on the outer portions of the contour are very similar for the two injectors. The yawed diamond does not produce a symmetric plume like the Baseline injector but still has a horseshoe-like shape.

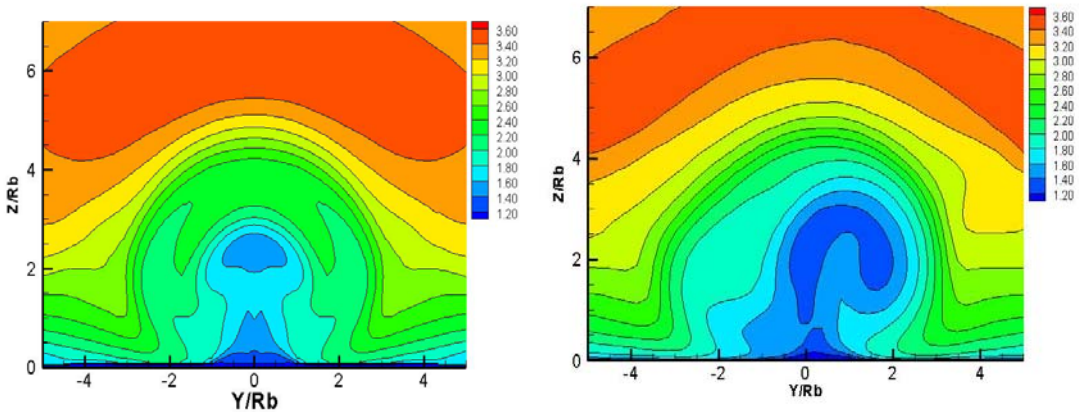

Figure 6.41 Comparison of calculated Mach number contours in the $x/R_b = 15.6$ plane for Baseline and yawed diamond injectors. The Baseline prediction is on the left and the yawed diamond prediction is on the right.

6.3.4 Total Pressure Contours

The predicted total pressure for the yawed diamond injector was normalized by the freestream total pressure and can be found in Figure 6.42. The diamond injector is compared to the normalized pressure ratio as opposed to the normalized Pitot pressure ratio because of the available experimental data. The contours are slices in the y-z plane were taken at $x/R_b = 15.6$. There is very good agreement between the CFD and the experiment. The magnitude of total pressure ratio in the plume and the shape of the plume are well predicted. The total pressures are more easily predicted by numerical analysis than mass diffusion.

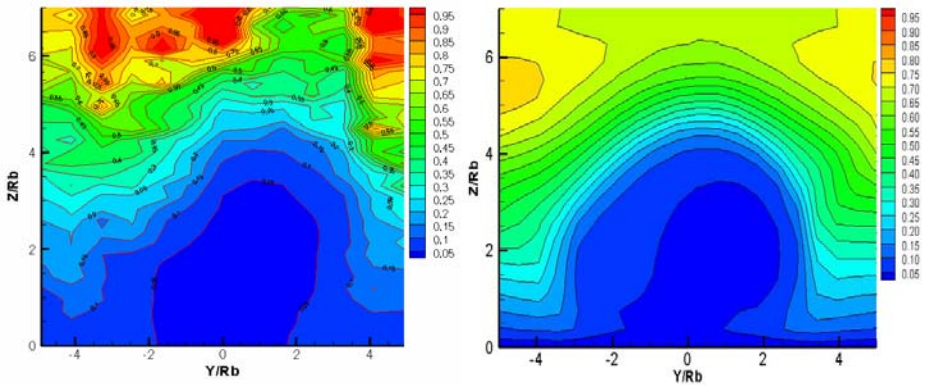

Figure 6.42 Normalized total pressure ratio in the x/R $_b$ = 15.6 plane of the yawed diamond injector. The experimental result is on the left and the CFD prediction is on the right.

Normalized total pressure contour comparisons of the Baseline injector and the yawed diamond injector can be found in Figure 6.43. The magnitude of total pressure in the plume is similar for the two contours. The yawed diamond injector has a larger region of low total pressure gas.

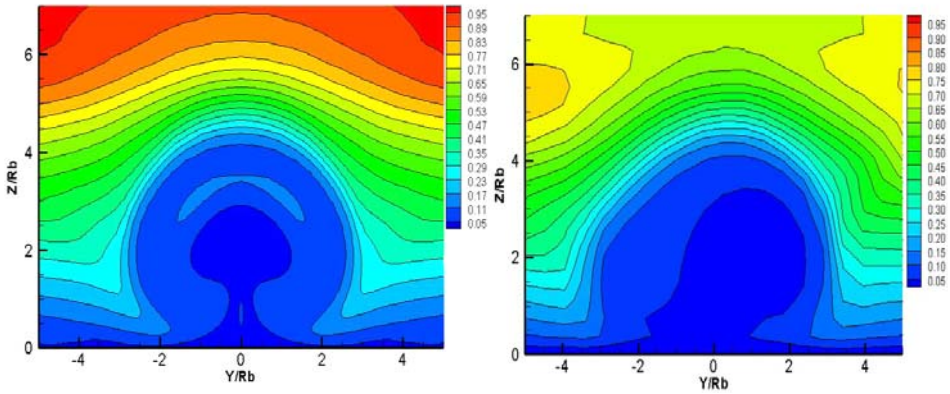

Figure 6.43 Normalized total pressure ratio in the y-z plane at x/R$_b$ = 15.6 comparing the Baseline injector and the aligned diamond injector. The Baseline injector is on the left and the diamond injector is on the right.

6.3.5 Plume Characteristics and Integrated Parameters

The downstream progression of mixing efficiency and plume center of mass is plotted for the yawed diamond injector in Figure 6.44. Comparisons are also made to the Baseline injector and the aligned diamond injector. The yawed diamond injector has the highest mixing efficiency closest to injection, however as the plume progresses

downstream, the yawed diamond injector has the smallest mixing efficiency. The benefits of rotating the diamond injector occur closest to injection in the large-scale mixing region. The initial penetration of the center of mass is comparable for all three injectors. After approximately 14 effective radii, the center of mass for the Baseline injector penetrates the furthest. The diamond injectors have almost identical center of mass penetration with downstream progression.

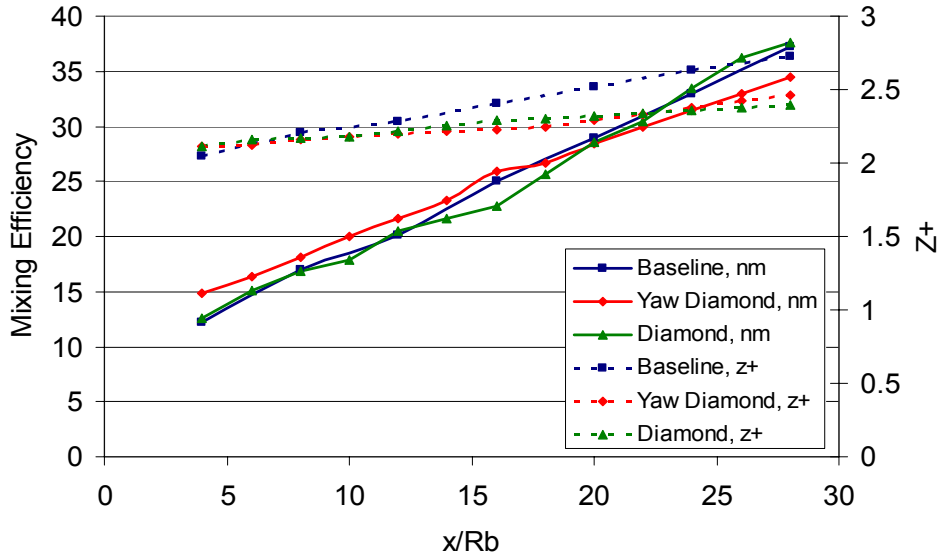

Figure 6.44 Downstream progression of mixing efficiency and plume center of mass for the yawed diamond injector comparing to the Baseline and aligned diamond injectors.

A comparison of the experimental results and the computational predictions for the yawed diamond injector can be found in Table 6-6. The width and height of the plume is under-predicted by 0.85 and 0.64 effective radii respectively by the CFD analysis. However, the predicted center of mass of the plumes agrees well with the experimental results. The maximum concentration for the yawed diamond injector is under-predicted by CFD and as a result, the mixing efficiency is over-predicted. The values are similar to the predicted values for the Baseline injector. The total pressure loss parameter is larger than the experimental results, but both the experiment and the CFD predict a decrease in total pressure loss parameter for the yawed injector from the Baseline injector.

Table 6-6 Plume characteristics and integrated parameters for the yawed diamond injector compared to the Baseline injector at x/R_b =15.6 downstream from injection.

		Yawed Diamond	
		Experiment	CFD
Plume Width	**$y\pm$**	**7.30**	**6.45**
Maximum Plume Height	**z_{max}**	**5.2**	**4.56**
Plume Center of Mass	**z^+**	**2.23**	**2.22/0.92**
Maximum Concentration	**σ_{max}**	**0.61**	**0.41**
Mixing Efficiency	**η_m**	**0.17**	**0.26**
Total Pressure Loss Parameter	**Π**	**0.25**	**0.30**

The CFD predictions at 15.6 and 27.8 effective radii are compared to the Baseline injector and can be found in Table 6-7. The yawed diamond injector spreads laterally almost a diameter more than the Baseline injector and has similar vertical penetration as the Baseline injector. The plume center of mass for the yawed diamond injector is higher than the Baseline injector at 15.6 effective radii. The Baseline injector has a faster growth rate of the plume with downstream progression than the yawed diamond injector. This could be attributed to better small-scale mixing by the Baseline injector. There is a larger increase in plume width, height and center of mass from 15.6 to 27.8 effective radii for the Baseline injector than for the yawed diamond injector.

Keeping in mind that the CFD under-predicted the concentration compared to experiment, there is a similar decrease in concentration over distance between the Baseline and yawed diamond injectors. The Baseline injector had a larger increase in mixing efficiency from 15.6 to 27.8 effective radii than the yawed diamond with similar values at 27.8 effective radii. The total pressure loss parameter increases by the same amount for both injectors. The yawed diamond injector has a lower total pressure loss parameter than the Baseline injector because even though the total pressure contours were similar, the integrated parameter is mass-weighted. The same trend was found between the Baseline and aligned diamond injectors.

Table 6-7 Plume characteristics and integrated parameters for the yawed diamond injector at $x/R_b = 27.8$ downstream from injection

		CFD Baseline Injector		CFD Yawed Diamond Injector	
x/R_b location		**15.6**	**27.8**	**15.6**	**27.8**
Plume Width	**$y\pm$**	**5.65**	**6.48**	**6.45**	**6.70**
Maximum Plume Height	**z_{max}**	**4.58**	**5.33**	**4.56**	**5.12**
Plume Center of Mass	**z^+**	**2.15**	**2.81**	**2.22/0.92**	**2.46/0.461**
Maximum Concentration	**σ_{max}**	**0.35**	**0.17**	**0.41**	**0.23**
Mixing Efficiency	**η_m**	**0. 23**	**0.37**	**0.26**	**0.35**
Total Pressure Loss Parameter	**Π**	**0.40**	**0.46**	**0.30**	**0.37**

6.3.6 Vorticity

The predicted vorticity contours at $x/R_b = 15.6$ and $x/R_b = 27.8$ in the y-z plane for the yawed diamond injector can be found in Figure 6.45. The yawed diamond injector has a small vortex core to the right-hand side of the centerline, but the vortex appears to separate from the remainder of the plume's stronger vorticity, especially as the plume moves downstream. The left-hand side of the plume has an area of high vorticity near the surface. Again, there is an area of low vorticity fluid surrounded by an area of high vorticity fluid. The rotation of the plume is away from the centerline, but the fluid that is forced down and to the left is then rotated clockwise towards centerline and over the top of the plume to the right hand side where it loses rotation. The center of the plume is comprised of a region of weaker vorticity surrounded by stronger vorticity in the fluid. There is also a slender region of low vorticity on the centerline of the plume. The interfaces of weak and strong vorticity aid in mixing through entrainment and diffusion.

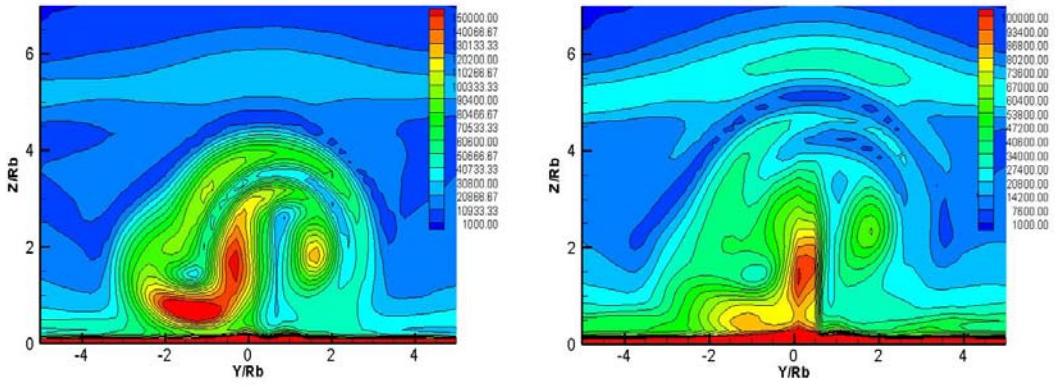

Figure 6.45 Predicted vorticity in the y-z plane at x/R_b =15.6 on the left and at x/R_b =27.8 on the right of the yawed diamond injector.

The yawed diamond vorticity prediction is compared to the Baseline prediction at 15.6 effective radii in Figure 6.46. The yawed diamond injector is predicted to have stronger vorticity in the bottom portion of the plume, whereas the Baseline injector has stronger vorticity away from the surface. The Baseline injector predicts stronger vorticity in the plume than the yawed diamond injector. The same trend was found when comparing the Baseline injector to the aligned diamond injector. The change in shock strength and structure created by the different shape injectors plays a role in the magnitude difference in the vorticity contours. Comparing the vorticity of the diamond injector and the yawed diamond injector shows that for the studied flow condition, an increase in vorticity is not achieved by rotating the diamond injector. The mixing is similar for the two cases as well.

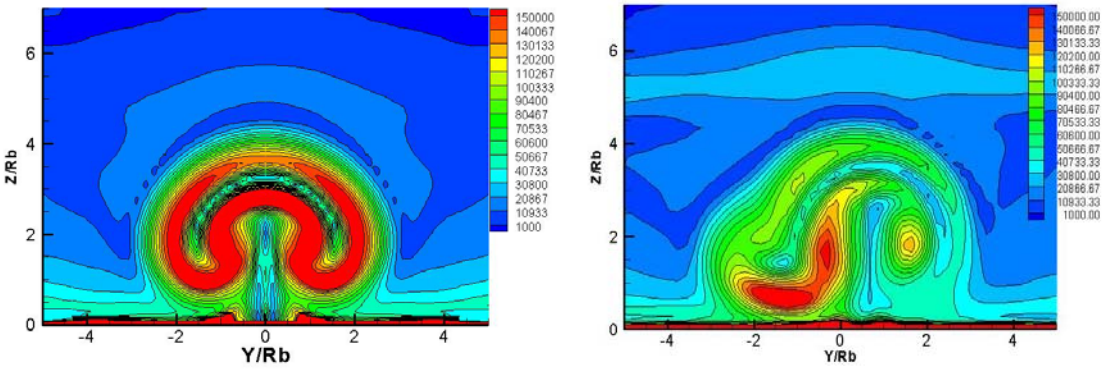

Figure 6.46 Predicted vorticity of the Baseline and yawed diamond injector in the y-z plane at x/R_b =15.6. The Baseline prediction is on the left and the yawed diamond prediction is on the right.

A vorticity iso-surface contour of the yawed diamond injector can be found in Figure 6.47. Flow is directed out of the page. Rotating the diamond injector causes the plume to skew towards one side. The diamond injector now behaves like a wing at an angle of attack with a higher pressure on one side and lower pressure on the other. The pressure differential causes rotation of the fluid and induces vorticity. A horse-shoe type shape can still be seen but it is rotated and skewed with unequal strength vorticies.

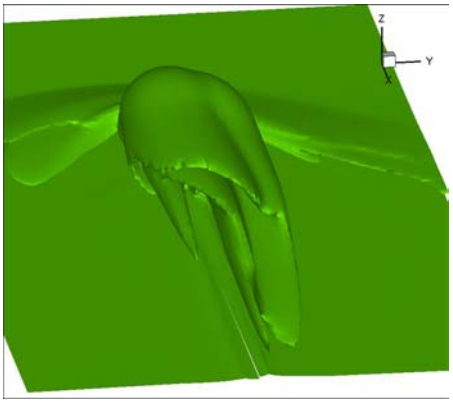

ω =100,000 /sec

Figure 6.47 3D vorticity iso-surface for the yawed diamond injector.

Figure 6.48 overlays vorticity contours with 2-D velocity streamlines. The contours are slices in several y-z planes. It takes approximately 15.6 effective radii for the CVP to form for the yawed diamond injector (similar to the aligned diamond injector). Rotating the diamond injector causes the CVP produced by injection to tilt with unequal vortex strengths. Closer to injection, the vortex pair is unstable. The unstable flow structure is beneficial for large-scale mixing which occurs closest to the injection point.

The behavior of the flow around the injector can be seen by the 3-D streamlines found in Figure 6.49. The CVP can be seen by the streamlines in Figure 6.49(b). The difference in behavior of flow around either side of the yawed diamond injector can be seen in Figure 6.49 (a). Vortex shedding is produced from the sharp points of the diamond injector and the pressure changes from the compression and expansion of the flow surrounding the injector Vortex roll-up in front of the injector and around the sides is evident in the picture on the right, Figure 6.49(c). The fuel injected near the edges of the orifice contains the majority of the rotation.

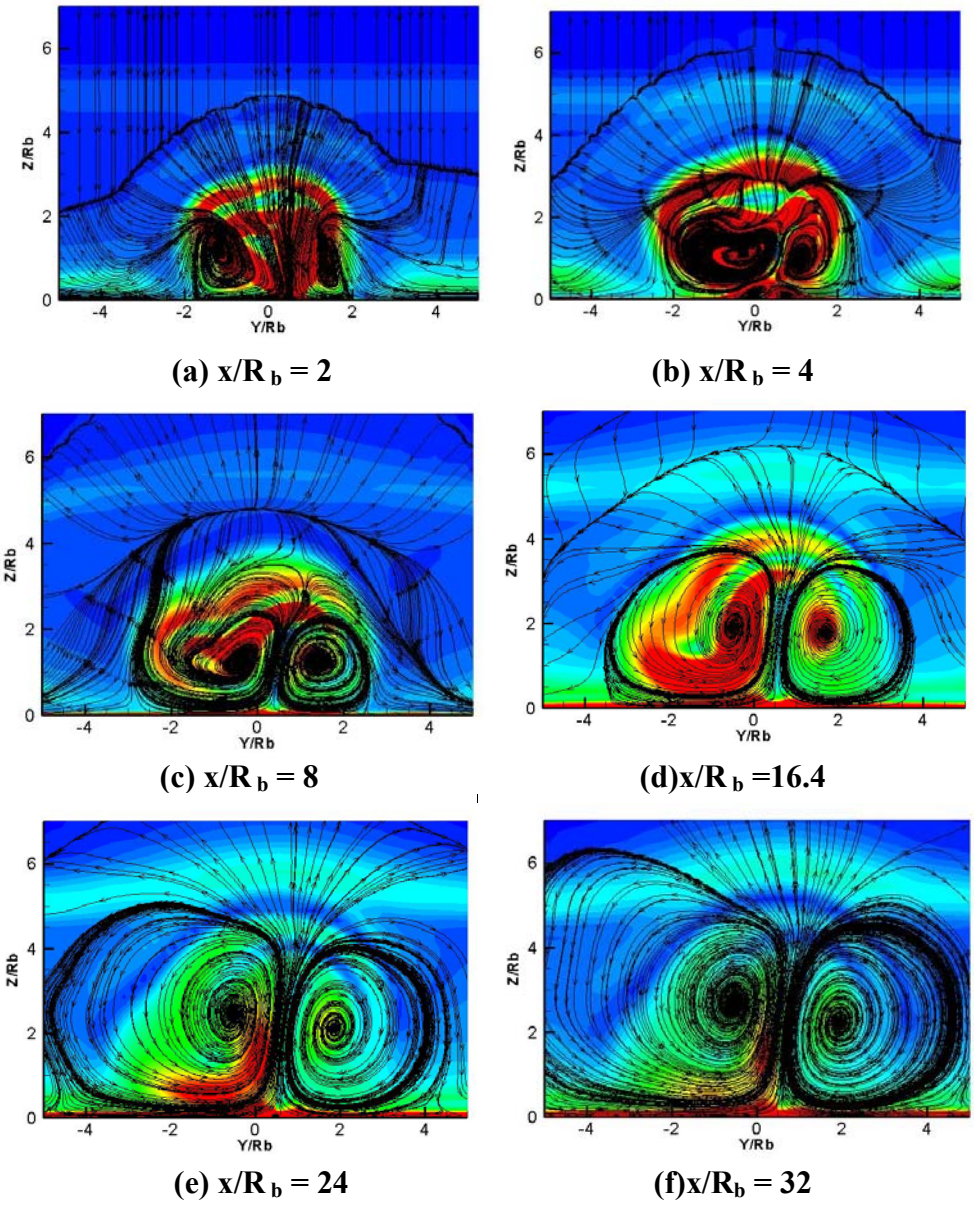

(a) $x/R_b = 2$ (b) $x/R_b = 4$

(c) $x/R_b = 8$ (d) $x/R_b = 16.4$

(e) $x/R_b = 24$ (f) $x/R_b = 32$

Figure 6.48 Contours of vorticity overlaid with streamlines for the yawed diamond injector. Slices in the y-z plane at various x/d_{eff} locations.

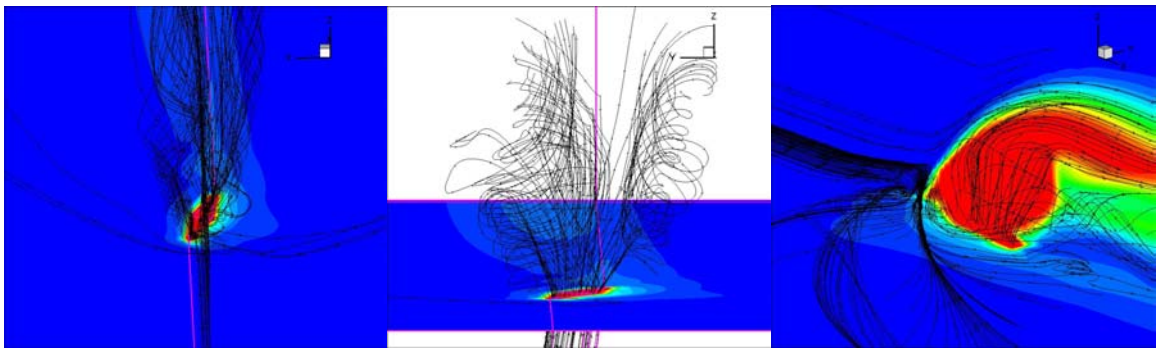

(a) Flow into page **(b) Flow into page, y-z plane** **(c) Flow left to right**

Figure 6.49 3D Momentum streamlines of the yawed diamond injector.

6.4 Unsteady Analysis

Unsteady analyses were performed for the Baseline injector and the aeroramp injector. The steady state and unsteady predictions seen below contain a boundary layer that is slightly more than half the height of the boundary layer in the main calculations for comparison with the experiments. The unsteady analysis with the smaller boundary was assumed to be sufficient from which to draw conclusions. The integrated parameters shown below are representative of the smaller boundary layer predictions as well.

The unsteady predictions were run using a dual-time stepping method in GASP. The Baseline unsteady analysis was completed using a time step of 5e-8 seconds and 7 inner iterations per time step. The analysis took 700 hours wall-time and 21,000 CPU hours to run on 80 processors. The aeroramp unsteady analysis was completed with a time step of 1.0e-7 seconds and 7 inner iterations per time step. It took approximately 400 hours wall-time and 11,000 CPU hours to run on 80 processors. The grids used for this analysis were the same as described in Chapter 3.

Initial oscillations caused by the transient solution were present in the predictions, however, the perturbations were damped out and the solutions for both injectors converged on the steady state solutions. A correlation coefficient was calculated to compare the unsteady and steady state predictions. The correlation coefficient is defined as:

$$R^2 = 1 - \frac{\sum (y_i - \hat{y})^2}{\sum (y_i - \bar{y})^2} \qquad \textbf{6-2}$$

Where y_i is the time averaged variable, $\hat{y}$ is the steady state variable and $\bar{y}$ is the average variable. An R value of 1 is 100% correlation and a R value of 0 corresponds to no correlation.

Figure 6.50 is a slice in the y-z plane at 16.4 effective diameters. The figure shows the resultant correlation coefficient for the Baseline injector. The steady state and unsteady predictions are almost identical. If the correlation coefficient is integrated over the contour plane, the helium mass fraction has an R^2 value of 95% and the vorticity has an R^2 value of 99%. Note that the data used for the unsteady contour plane were not time averaged. Instead, the concentration values that the unsteady solution converged to were used.

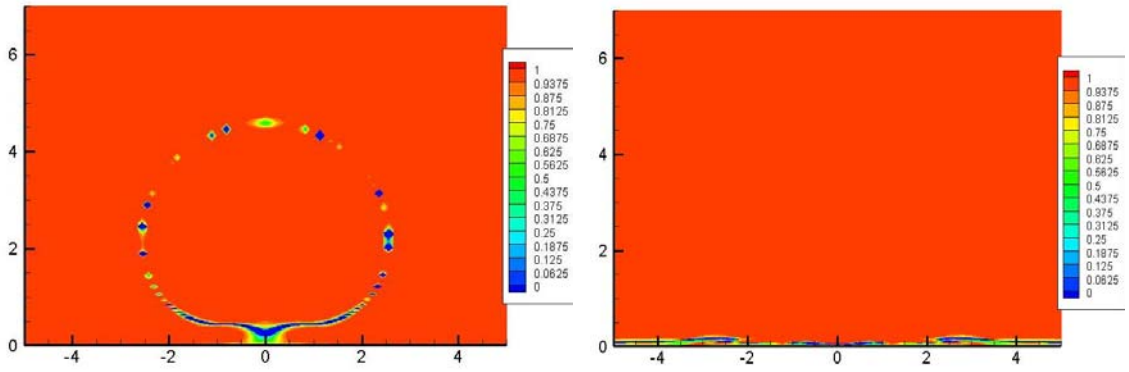

Figure 6.50 Correlation coefficient of helium mass fraction on the left and vorticity on the right for the Baseline injector.

Vertical lines of pressure along the centerline and at 1.5 diameters off-center just aft of the injector were plotted. The plots, Figure 6.51 and Figure 6.52 did not show any oscillations in pressure over time.

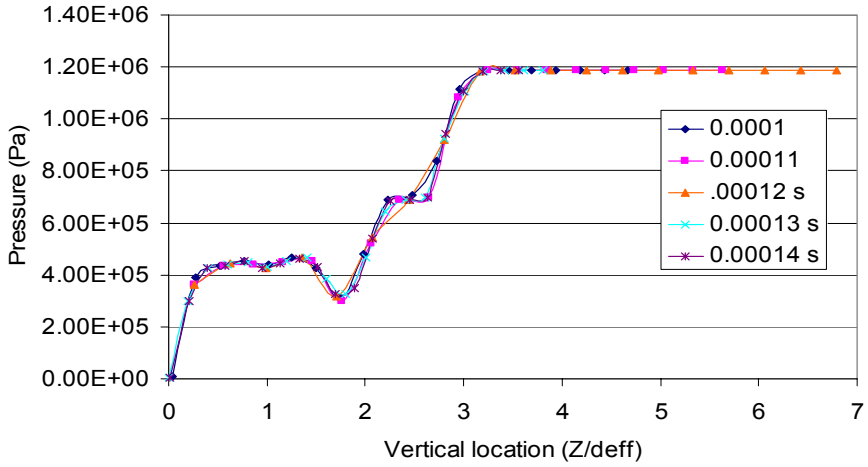

Figure 6.51 Pressure at $x/d_{eff} = 2$ and $y/d_{eff} = 1.5$ in the vertical direction for the Baseline injector.

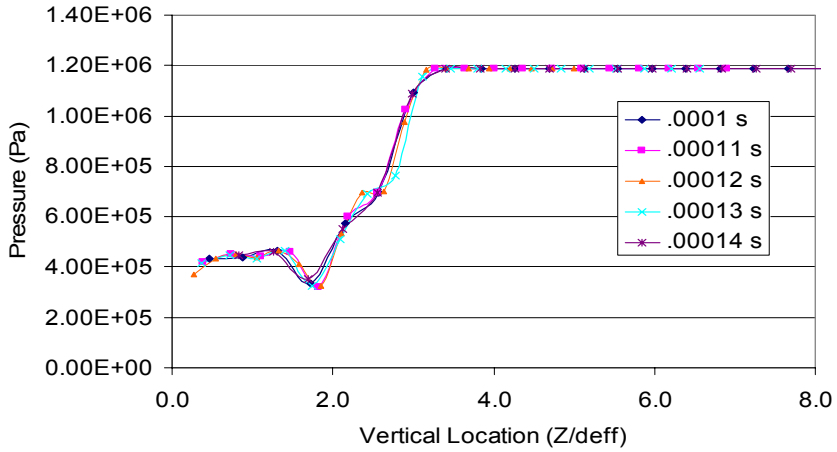

Figure 6.52 Pressure at $x/d_{eff} = 0$ and $y/d_{eff} = 1.5$ in the vertical direction for the Baseline injector.

Table 6-8 lists the steady state and unsteady integrated parameters for the Baseline injector. The maximum concentration and the mixing efficiency agree very well between the two simulations. The total pressure loss parameter also has good agreement. There are only very small difference between the steady state predictions and the unsteady converged prediction.

Table 6-8 Integrated parameters for the Baseline injector for steady state and unsteady predictions

		Steady	Unsteady
	x/d_{eff}	16.4	16.4
Plume Width	$y\pm$	5.14	5.14
Maximum Plume Height	z_{max}	4.50	4.49
Plume Center of Mass	z^+	2.41	2.41
Maximum Concentration	σ_{max}	0.57	0.56
Mixing Efficiency	η_m	0.18	0.19
Total Pressure Loss Parameter	Π	0.40	0.40

The correlation coefficient for the steady and unsteady analyses for the aeroramp injector can be found in Figure 6.53. The contours are slices in the y-z plane at 16.4 effective diameters. If the correlation coefficient is integrated over the plane, the helium mass fraction has a R^2 value of 78% and the vorticity has a R^2 value of 93%. The contours show relatively good agreement between the steady state and unsteady predictions for the aeroramp injector.

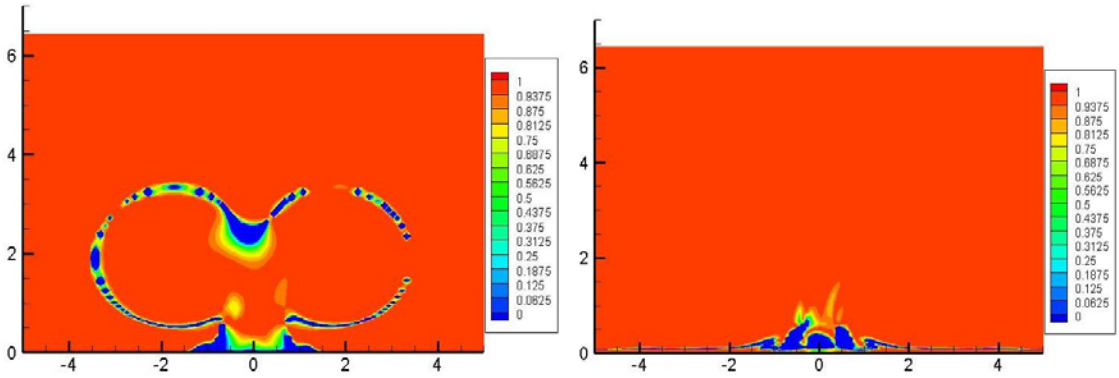

Figure 6.53 Correlation coefficient of helium mass fraction on the left and vorticity on the right for the aeroramp injector.

Table 6-9 lists the steady state and unsteady integrated parameters for the aeroramp injector. The size of the plume is very similar for steady state and unsteady analyses. The total pressure loss parameter is the same for both the steady state and unsteady solutions. The maximum concentration is slightly higher for the unsteady solution and the mixing efficiency is similar but the unsteady prediction is 0.01 lower than the steady state prediction.

Table 6-9 Integrated parameters for the aeroramp injector for steady state and unsteady predictions.

		Steady	Unsteady
	x/d_{eff}	16.4	16.4
Plume Width	$y\pm$	7.55	7.60
Maximum Plume Height	z_{max}	3.83	3.85
Plume Center of Mass	z^{+}	2.08	2.08
Maximum Concentration	σ_{max}	0.43	0.45
Mixing Efficiency	η_m	0.19	0.18
Total Pressure Loss Parameter	Π	0.41	0.41

The initial oscillations that were present in the transient period were not maintained over time in the unsteady analysis for both the Baseline and aeroramp injectors.

6.5 Shock Impingement Case

This section contains predictions of the interaction of impinging oblique shocks on transverse injection at three downstream locations. The locations are 2, 8 and 16 effective diameters downstream of the Baseline, round injector center designated Case 1, 2 and 3 respectively. Predictions include, mass fraction concentration, mixing, total temperature contours, total pressure contours, Mach number contours, vorticity contours and vorticity analysis across the shock.

6.5.1 Mass Concentration and Mixing

Helium concentration predictions are presented in the form of mass fraction contours plots in Figure 6.54. The plots are slices in the y-z plane at $x/d_{eff} = 16.4$. Comparisons are made between the CFD predictions on the left and the experimental plots on the right. Also, the Baseline case is compared with Case 1, shock surface impact at 2 effective diameters, in Figure 6.55, and the shock impingement cases are compared to each other in Figure 6.56. Some global results are given in Table 6-10.

The CFD analysis was able to predict the trends and mixing of the experiment. Comparing each analytical case to the corresponding experimental case shows that the CFD analysis predicted slightly less mixing for Case 1. However, there was good agreement for Cases 2 and 3 with the experimental results. The predicted mixing efficiency parameter can be found in Table 6-10. The shock impingement cases predicted better mixing than the Baseline case with Case 1 having the most efficient mixing. Although, the mixing efficiency and maximum concentration predicted for Case 3 is similar to the Baseline case, the experiment did not show any improvement in mixing for Case 3 over the Baseline case. Shocks intersecting the jet closer to injection have a greater effect on mixing because the gradients are larger and therefore more vorticity can be created. The increased vorticity enhances mixing by entraining freestream air which increases the surface area of the shear layer, the larger the surface area, the more diffusion between the freestream and injected gas.

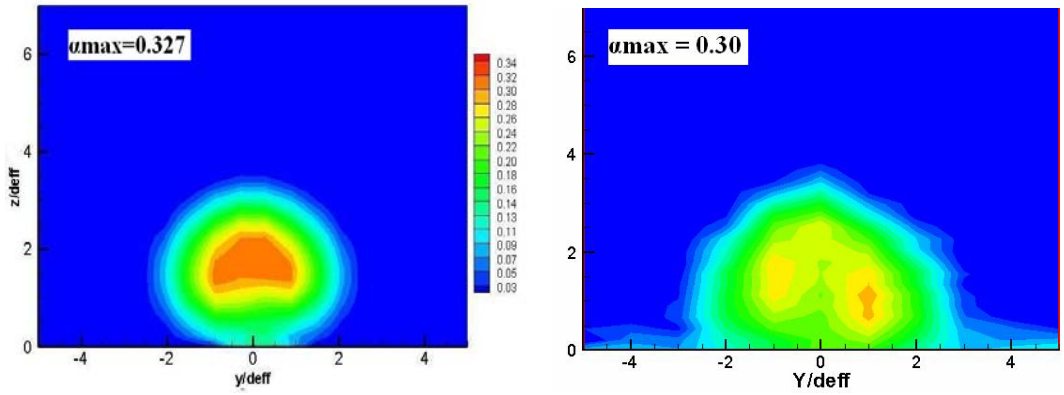

(a) Case 1 (Shock at $x/d_{eff} = 2$)

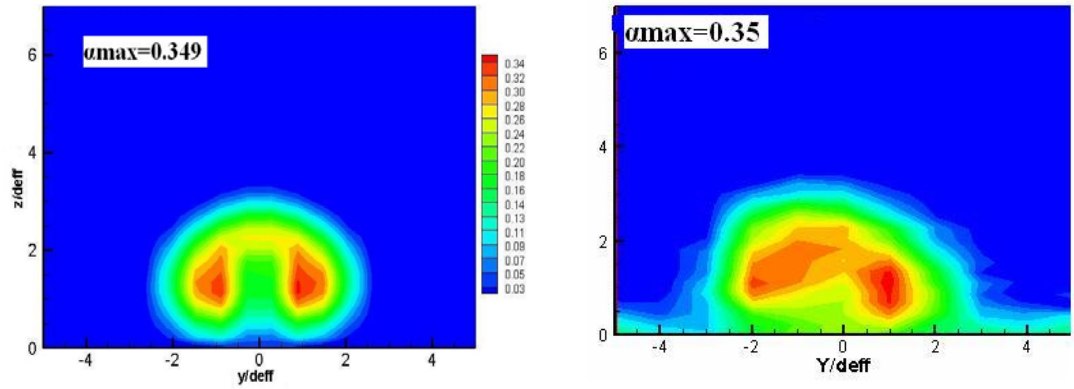

(b) Case 2 (Shock at $x/d_{eff} = 8$)

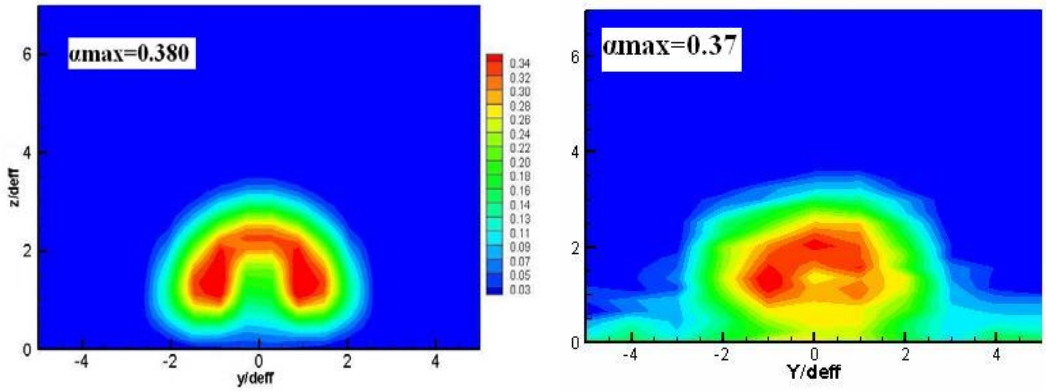

(c) Case 3 (Shock at $x/d_{eff} = 16$)

Figure 6.54. Comparison of mass fraction contours, in the y-z plane at x/d_{eff} = 16.4. CFD prediction (left) vs. experimental results (right)

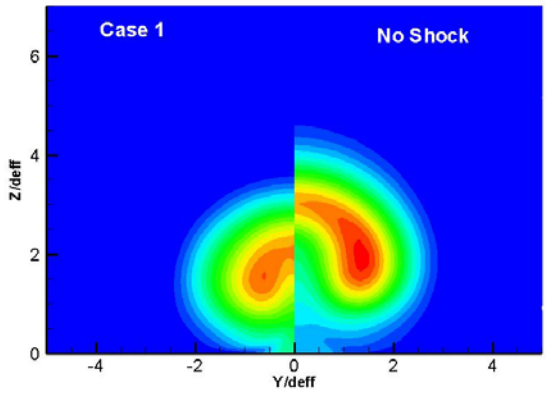

Figure 6.55. Helium mass fraction contours comparison between case 1 (left) and the Baseline case (right) in the y-z plane at $x/d_{eff} = 16.4$.

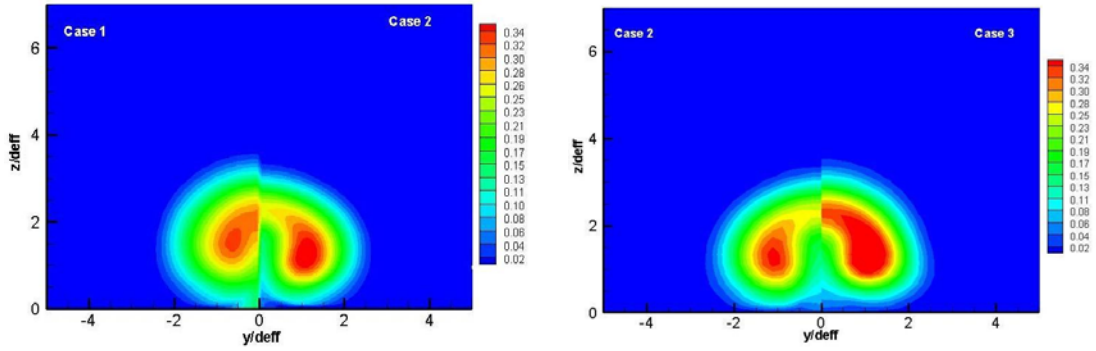

Figure 6.56. Helium Mass Fraction Contour Comparison between the Shock Cases in the y-z plane at $x/d_{eff} = 16.4$

Table 6-10 Integrated quantities performance comparison, shock impingement cases

		Baseline Case (No Shock)		Case 1 (x/d_{eff} =2)		Case 2 (x/d_{eff}=8)		Case 3 (x/d_{eff}=16)	
		Exp	CFD	Exp	CFD	Exp	CFD	Exp	CFD
Maximum Concentration	σ_{max}	0.36	0.35	0.30	0.33	0.35	0.35	0.37	0.38
Mixing Efficiency	η_m	0.20	0.23	0.24	0.32	0.20	0.29	0.19	0.20
Plume Width	y±	6.90	6.40	5.20	4.88	6.30	5.12	6.30	5.05

A downstream progression of the Baseline case compared to each shock Case can be found in Figure 6.57. Initially, Case 1 has a significantly smaller maximum helium concentration than the other Cases and the Baseline case. This confirms better mixing with shock impingement closer to the injection point. However, past 20 effective diameters, better mixing is achieved for Case 2 and Case 3 than the Baseline case. All three cases have better mixing than the Baseline case.

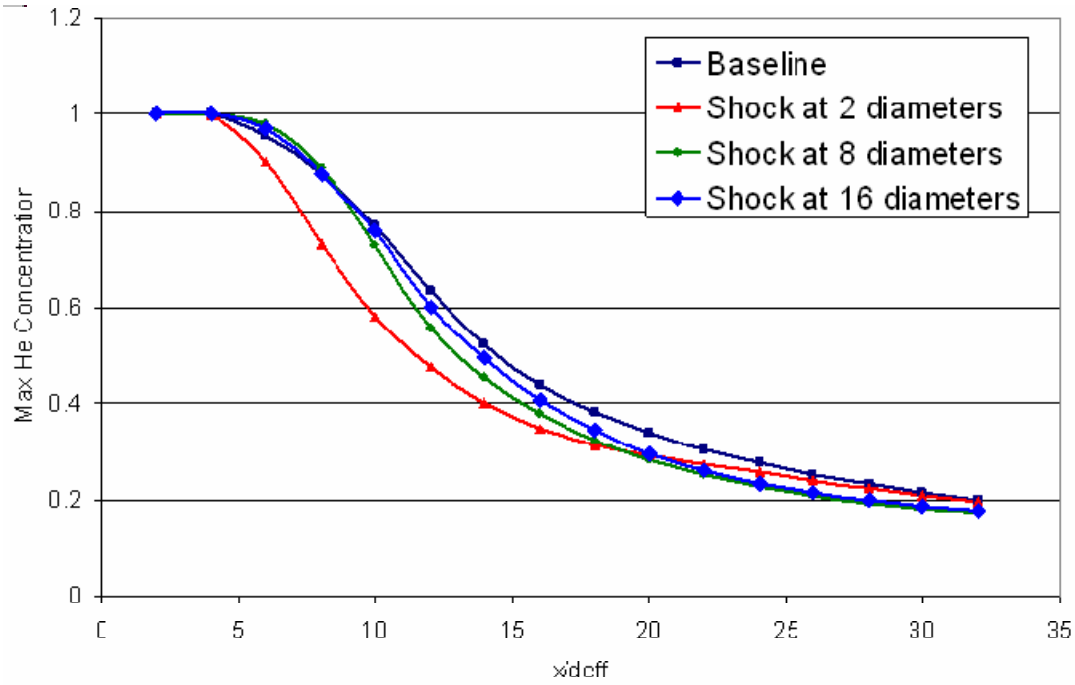

Figure 6.57 Downstream progression of helium concentration comparing each shock Case to the Baseline case.

6.5.2 Total Temperature Contours

The total temperature contours can be found in Figure 6.58. The total temperature is normalized by the freestream total temperature and plotted in the y-z plane at x/d_{eff} = 16.4. The CFD predictions show the same trend as the experimental results, the total temperature distribution for each of the shock cases do not vary significantly. Since the only difference in the flow-fields of the shock impingement cases is the location of intersection with the jet and the properties across the shock are the same, large differences in total temperature are not expected. The contours show that the CVP present in the shock cases creates a stronger total temperature region surrounded by a larger region of low total temperature fluid. Crocco's Theorem Equation [5-4] indicates that gradients in total enthalpy are related to entropy and temperature gradients which can cause the creation or destruction of vorticity.

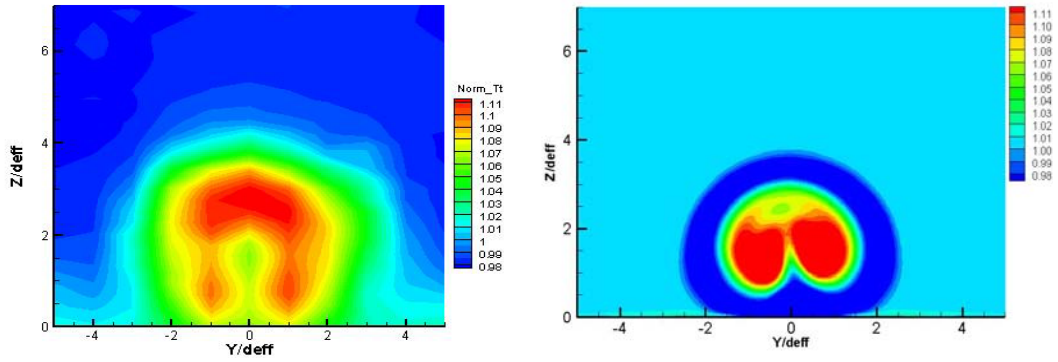

(a) Case 1 (Shock at x/d_{eff} = 2)

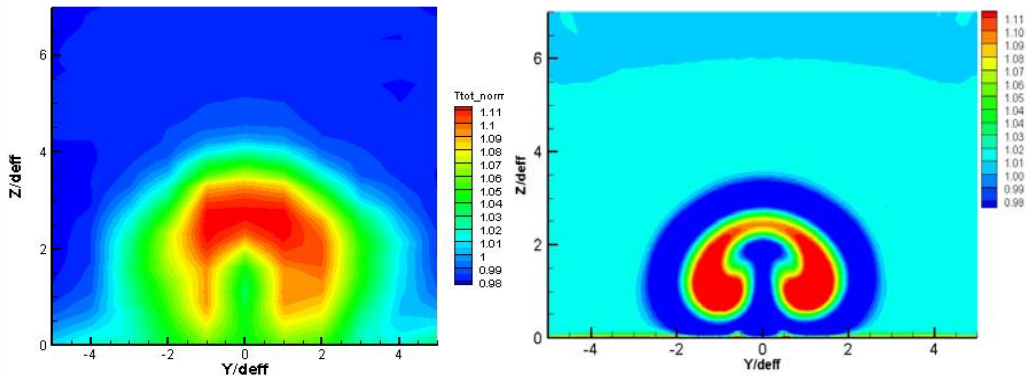

(b) Case 2 (Shock at x/d_{eff} = 8)

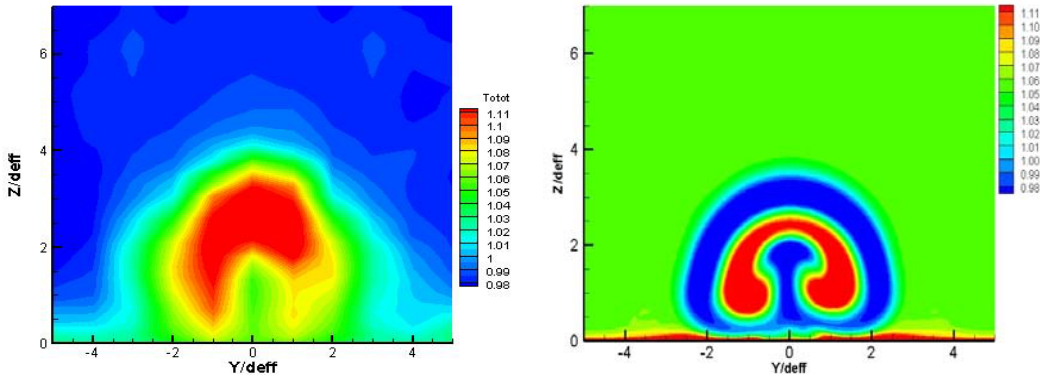

(c) Case 3 (Shock at x/d_{eff} = 16.4)

Figure 6.58. Normalized total temperature contours in the y-z plane at x/d_{eff} = 16.4. The experimental results are on the left and the CFD predictions are on the right.

6.5.3 Mach Number Contours

The Mach number contours can be found in Figure 6.59. The Mach number for the shock cases is less than the Mach number for the Baseline case, since the Mach number decreases across an oblique shock. The three shock impingement cases are very similar to one another. The bow shock created by the injection can be seen above the jet plume. The location and size of the discontinuity is different between the cases as a result of the location of interaction with the oblique shock impinging on the jet and bow shock.

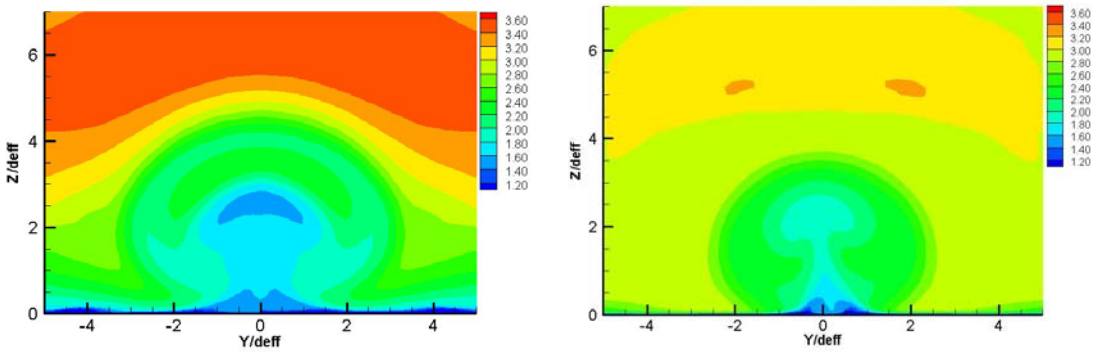

(a) Baseline case (No Shock) **(b) Case 1 (Shock at x/d_{eff} = 2)**

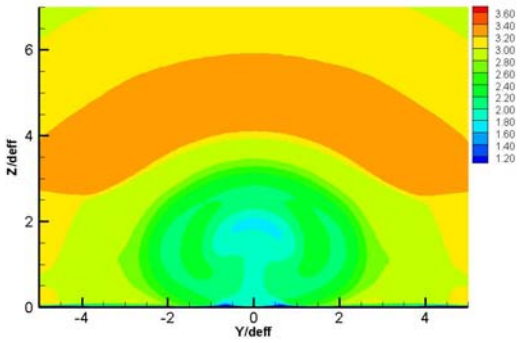

(c) Case 2 (Shock at $x/d_{eff} = 8$)

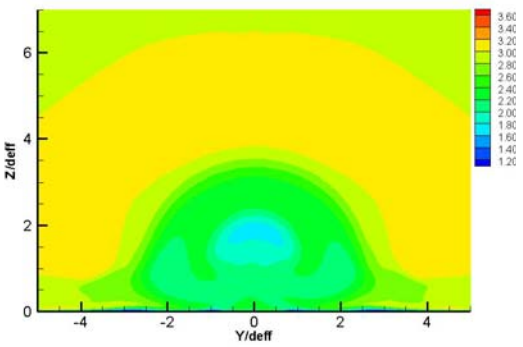

(d) Case 3 (Shock at $x/d_{eff} = 16$)

Figure 6.59 Mach Number Contours in the y-z plane at $x/d_{eff} = 16.4$

6.5.4 Pitot Pressure

The total pressure contours can be found in Figure 6.60. The calculated total-pressure was modified with Equation [5-5] to obtain the Pitot Pressure, P_{t2}. P_{t2} was than normalized by the freesream total pressure. The contour planes are 16.4 effective diameters downstream of the injector. At this location, the flow in Case 1 has passed through both the incident shock and the reflected shock, resulting in a higher total pressure loss. The variation in pressure away from the plume is a result of the bow shock and oblique shock locations for each case. The fluid in the interior of the plumes is at a much lower total pressure ratio than the freestream fluid. The shock cases have larger apparent total pressure losses than the Baseline case because of the total pressure losses through the impinging shock. The total pressure loss parameter used earlier is not relevant for cases with an externally generated impinging shock.

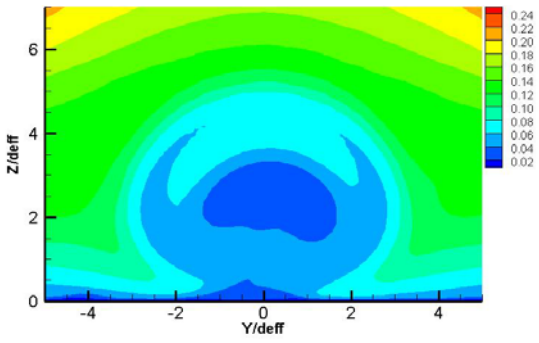

(a) Baseline case (No Shock)

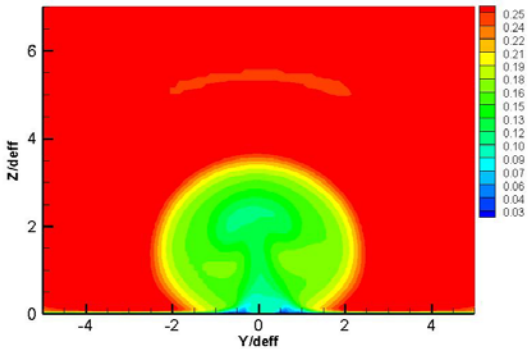

(b) Case 1 (Shock at $x/d_{eff} = 2$)

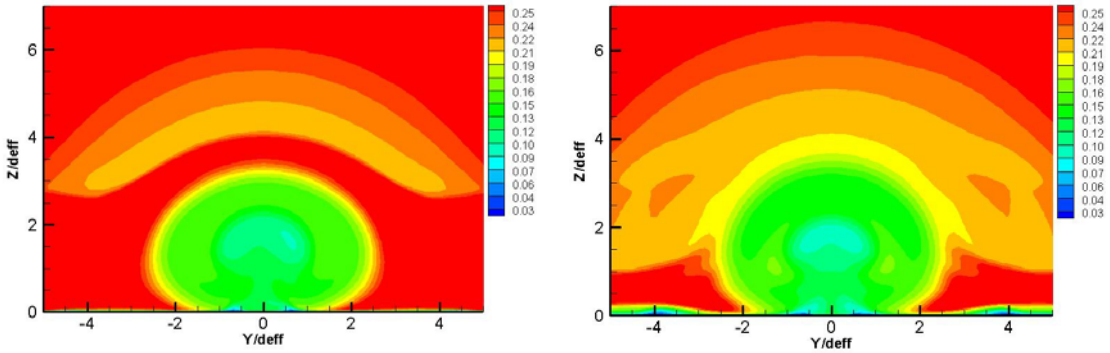

(c) Case 2 (Shock at $x/d_{eff} = 8$) **(d) Case 3 (Shock at $x/d_{eff} = 16$)**

Figure 6.60. Normalized Pitot pressure contours, slices in y-z plane at $x/d_{eff} = 16.4$

6.5.5 Vorticity

6.5.5.1 Changes Across the Shock

To gain a better understanding of how mixing is increased in the presence of shocks, an analysis of the vorticity change across the shocks in the plumes was completed. The analysis utilized two planes parallel to the shock, one just before and one just after. Through a coordinate transformation, the in-plane and normal-to-the-shock vorticity components were calculated from the x, y and z vorticity components. See Equation [6-3] and Equation [6-4] below.

$$\begin{pmatrix} \omega_n \\ \omega_t \end{pmatrix} = \begin{bmatrix} \cos(\theta) & \sin(\theta) \\ -\sin(\theta) & \cos(\theta) \end{bmatrix} \begin{pmatrix} \omega_x \\ \omega_z \end{pmatrix} \quad \textbf{6-3}$$

$$\overline{\omega}_{in-plane} = \sqrt{\omega_t^2 + \omega_y^{\,2}} \quad \textbf{6-4}$$

The vorticity over each plane of equal area was integrated, and then the integrated quantity before the shock was subtracted from the integrated quantity after the shock. The vorticity was normalized by the freestream velocity and injector diameter, u_∞/d_{effj}. The resulting change in vorticity magnitude and in-plane vorticity across the shock for each case can be found in Table 6-11. Case 1 shows the largest increase in both vorticity magnitude and in-plane vorticity. Since the shock impingement is closest to the point of injection for case 1, it encountered the largest density gradients in the plume. Also, at 2 diameters behind the injector, the plume is nearly perpendicular to the shock which gives

the largest cross product of the density and pressure gradients. The larger non-aligned gradients created the largest change in vorticity due to baroclinic effects. For Case 3, with the shock impingement at 16 effective diameters behind the shock, the plume and the shock have a smaller interior angle with respect to each other which makes the cross product of the gradients smaller than Case 1. The density gradients in the plume have also decreased.

Table 6-11. Non-dimensional vorticity jump across shock

	Δ Vorticity Magnitude	Δ In-plane Vorticity (tangential to shock)
Case 1 (shock at x/d_{eff} = 2)	0.0739	0.0680
Case 2 (shock at x/d_{eff} = 8)	0.0527	0.0461
Case 3 (shock at x/d_{eff} 16)	0.0208	0.0135

A pictorial description of the vorticity jump across the shock can be found in Figure 6.61. Note that the contour levels for the three figures are not the same. The left hand contour plot for each figure is of the in-plane vorticity and the right hand plot displays the vorticity normal to the shock. The normal vorticity does not change across an oblique shock because if the fluid is rotating about the normal axis then the corresponding velocity of the fluid is in-plane. The in-plane or tangential velocity does not change across an oblique shock, therefore the normal vorticity is expected to be constant. The contours show minimal changes in normal vorticity. It can be seen from the contour plot on the left that there is an increase in the in-plane vorticity. Each contour shows two slices parallel to the shock less than a diameter apart. Each contour slice shows half of the plume. The slice on the left within each contour is before the shock, and the slice on the right is after the shock. For Case 1, vorticity is increased at the bottom and in the interior of the plume. Case 2 has a slight increase in vorticity near the bottom of the plume, but the largest difference is in the center. Case 3 actually has less vorticity near the bottom after the shock than before, however there is a larger amount of vorticity in the center and top of the plume. Also, a looped area of vorticity is created towards the outside of the plume. When the shock intersects the plume, the edge of the shear layer

curls away from the surface and rotates back towards the plume. This creates a larger surface area and more mixing through diffusion.

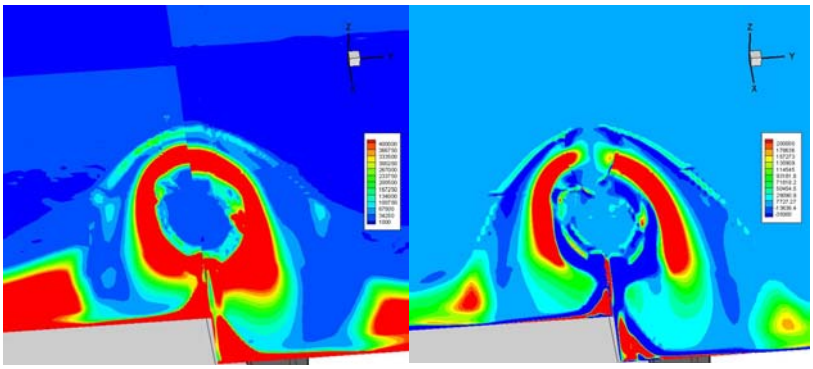

(a) Case 1 (Shock at x/d_{eff} =2)

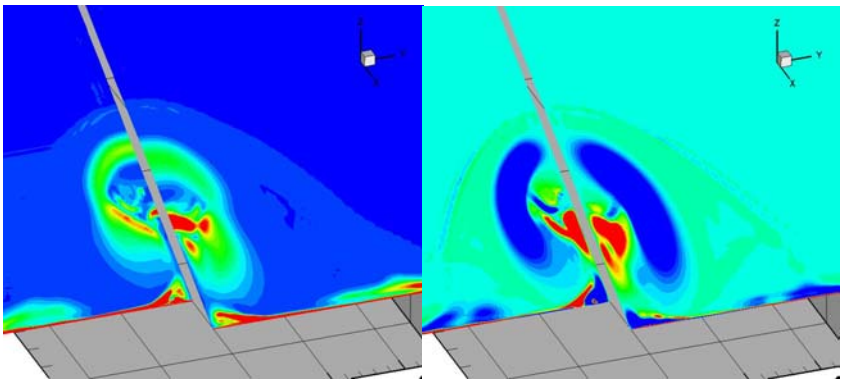

(b) Case 2 (Shock at x/d_{eff} = 8)

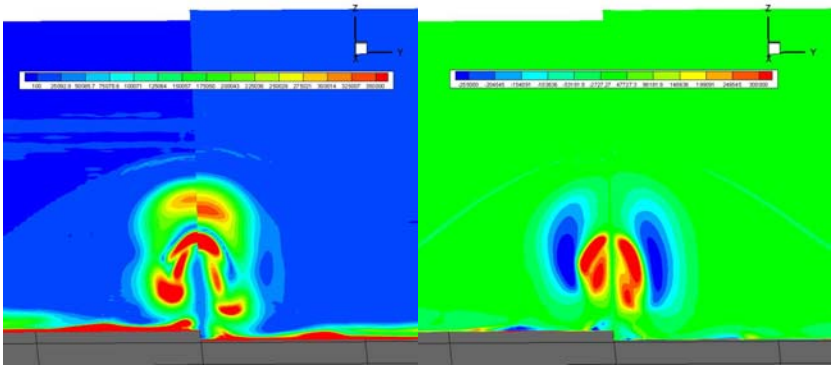

(c) Case 3 (Shock at x/d_{eff} = 16)

Figure 6.61 In-plane vorticity contours (left) and normal vorticity contours (right). Planes are parallel to shock (before and after).

6.5.5.2 Vorticity Progression Downstream

Progressions of the vorticity magnitude downstream can be found in Figure 6.62. The Baseline case, shown on the left-hand side is compared to each shock impingement

case on the right-hand side of each figure. The contours are vertical slices (y-z plane) at various x/d_{eff} locations, and only half of the plume is shown (symmetry). The x/d_{eff} locations are different for each figure corresponding to the area of shock impact. The plume does not penetrate as far vertically with a shock compared to the Baseline case, although the lateral penetration is better for the shock impingement cases. The shock causes a change in rotation of the light gas in the plume. For Cases 1 and 2, the stronger vorticity is located near the bottom and center of the plume. The shock cases maintain a stronger core vorticity as they move downstream. One effect of shock impingement can be seen by looking at Case 3, the bottom lobe of stronger vorticity visible in the Baseline case in Figure 6.62c (left-hand side) is split by the shock (right-hand side) into two areas of rotation. This changes the rotation and surface area of the plume and results in quicker mixing.

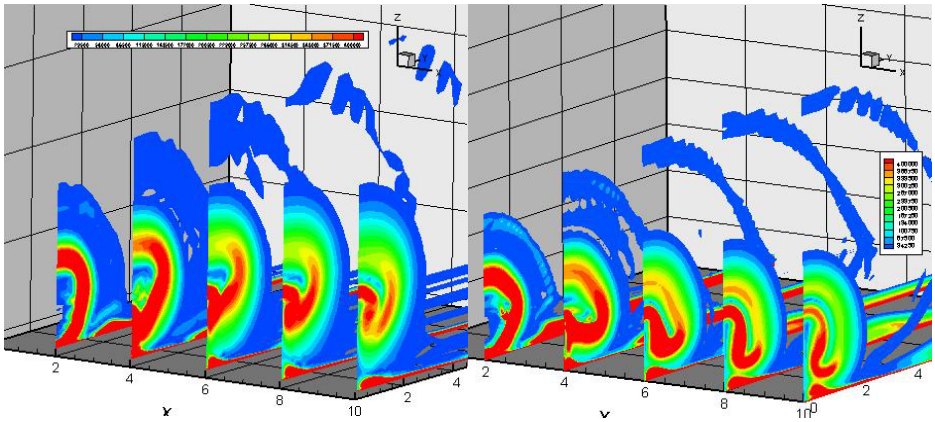

(a) Case 1 (Shock at x/d_{eff} = 2)

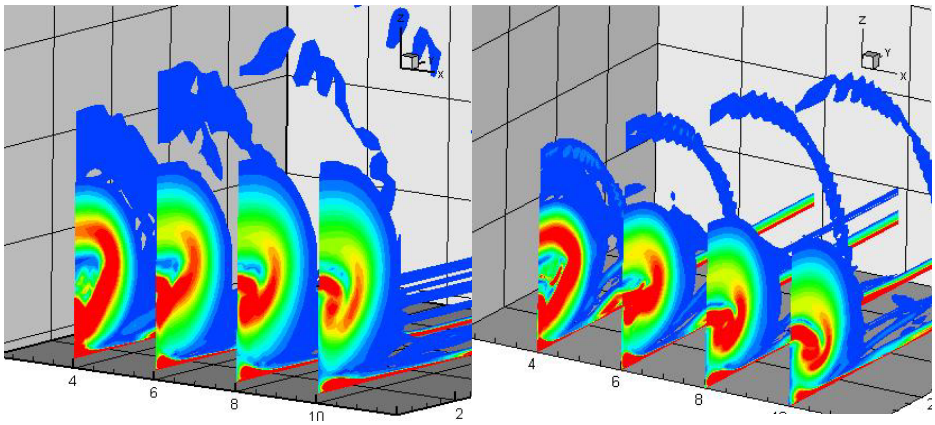

(b) Case 2 (Shock at x/d_{eff} = 8)

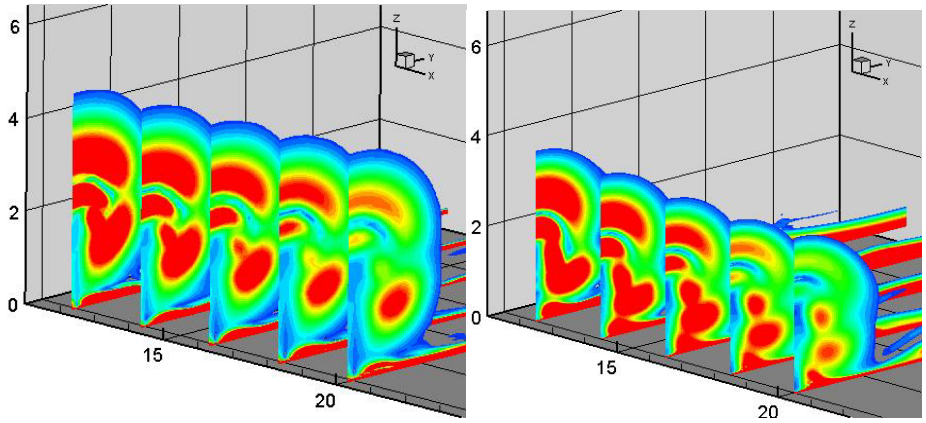

(c) Case 3 (Shock at x/d_{eff} = 16)

Figure 6.62 Vorticity magnitude progression, slices in the y-z plane at various x/d_{eff} locations. The Baseline case is on the left and each shock case is on the right

Figure 6.63 displays vorticity contours overlaid with streamlines for the Baseline case and Case 1. Focusing on half of the vortex pair, the rotation of vorticity is in a clockwise motion for the left-hand side of the Baseline case. This motion induces a strong vortex layer on the wall with counter-clockwise vorticity. The action of the primary vortex makes the layer roll into a secondary vortex which has the core connected to the near wall shear layer by a feeding sheet.

The Baseline case is an example of a jet of light gas with a CVP embedded in a heavy gas. The contours on the right-hand side of Figure 6.63 offer insight to the physical behavior of the jet with impinging shocks. If a shock was intersected with a jet that did not have initial vorticity, the core of the jet would behave like a cylindrical mass of low density gas embedded in a higher molecular weight gas. The radial density gradient between the gases would interact with the pressure gradient from the shock and then deposit a distribution of vorticity over the boundary. This baroclinic effect then varies along the length of the interface as the gradients and their included angles vary. The vorticity deposited on the outer half of the plume is in an upward and outward direction away from the centerline. The jets in a cross flow of this study, Cases 1, 2 and 3, have vorticity present from the CVP before the shocks intersect with the plume. This changes the rotation of the vortex cores slightly. Now, with a shock and initial vorticity, there is an added component of vorticity in the plume. Vorticity produced by the shock is summed with the vorticity produced by injection. This creates the different shape

streamlines seen for Case 1 as compared to the Baseline case. The vortex is comprised of both clockwise and counter-clockwise motion which enhances vortex stretching. Stretching, through gradient intensification, makes diffusive effects become important, which in turn promotes mixing.

Focus on Case 1 of the shock/jet interaction where the developing vortical structure has not yet stabilized into a vortex pair. The shock and jet combination creates the vortex dynamics described above, but now the shock impinges upon an unstable jet vortex pair. The less stable the original vortex pair before shock impingement, the greater the influence and the magnitude of the additional vorticity due to the shock. The expectation of greatly increased stretching for this situation is confirmed by the computations. It is possible to note the similarity between the vorticity contour at x/d_{eff} =8 for the case with a shock and the contour at x/d_{eff} = 16 for the Baseline case. This shows how the dynamics of the shock case at x/d_{eff} = 2 are faster than the Baseline case. The superior stretching is confirmed by the greater dissipation rate at x/d_{eff} = 16.

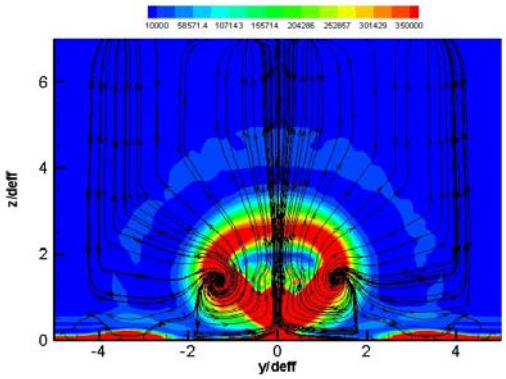

(a) Baseline case at x/d_{eff} = 4

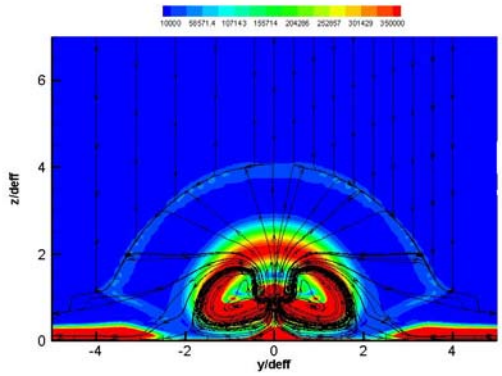

(b) Case 1 at x/d_{eff} = 4

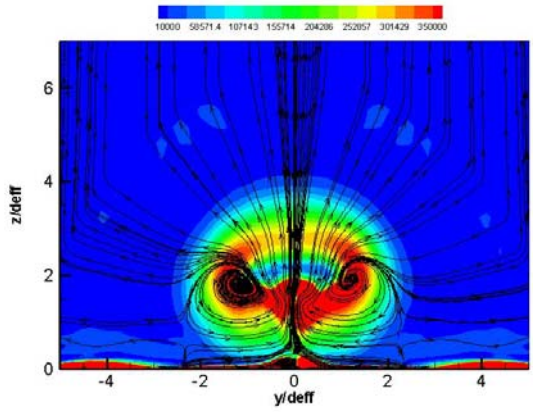

(c) Baseline case at x/d_{eff} =6

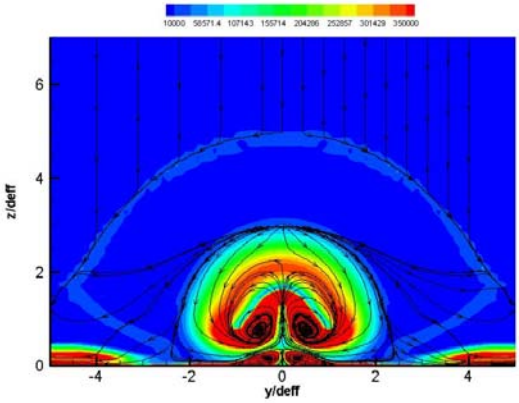

(d) Case 1 at x/d_{eff} = 6

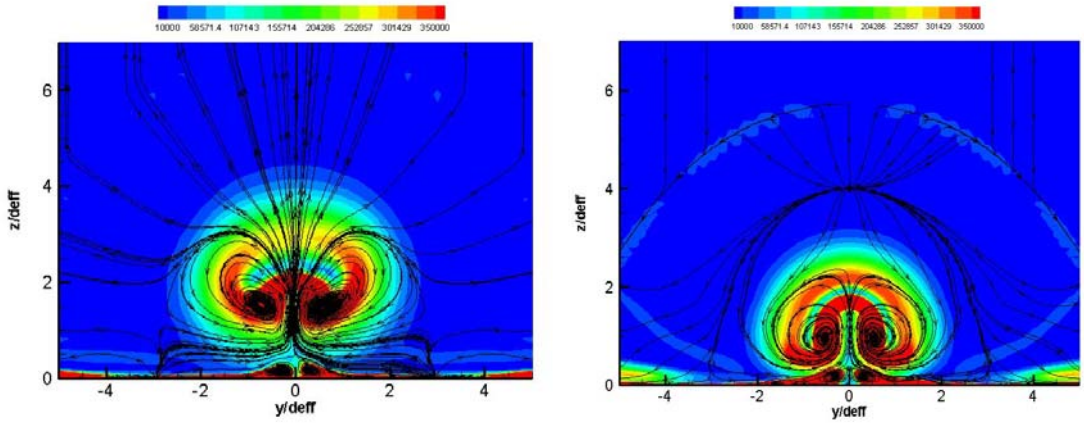

(e) Baseline case at x/d_{eff} =8 **(f) Case 1 at x/d_{eff} = 8**

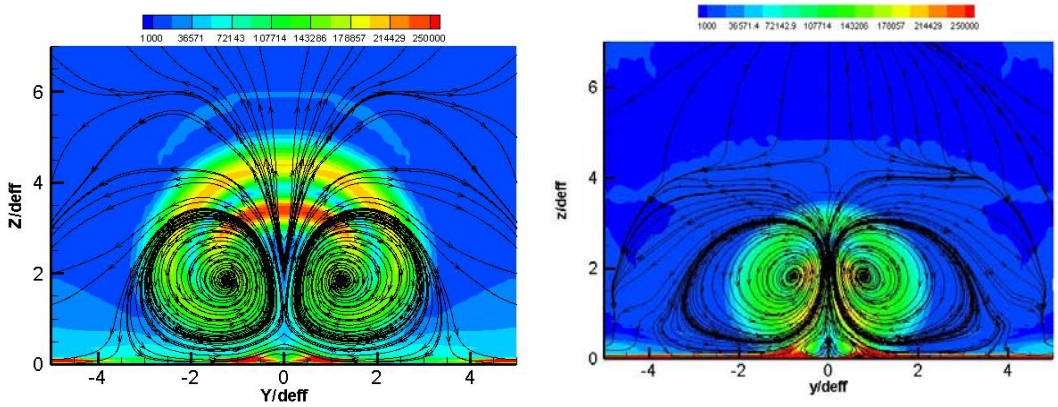

(e) Baseline case at x/d_{eff} = 16 **(f) Case 1 at x/d_{eff} = 16**

Figure 6.63. Vorticity contour Baseline case (No Shock) on the left compared to Case 1 (Shock at x/d_{eff} = 2) on the right overlaid with streamlines in the y-z planes.

6.6 Hydrogen Combustion Case

This section contains predictions and comparisons between a reacting and a non-reacting flow analyses. This study uses the same CFD grid as the Baseline injector study, but all computations were performed using hydrogen fuel as the injectant at different flow conditions. The reaction model used was described in Chapter 2. Predictions include, mass fraction concentration, mixing, total temperature contours, total pressure contours, Mach number contours and vorticity contours. In the figures, the combustion modeling predictions can be found on the right-hand side and the frozen flow predictions on the left-hand side of each figure.

6.6.1 Combustion

To ensure that combustion did occur for the combustion analysis, contour slices at 16 diameters were taken of a few of the products of hydrogen combustion with air. H_2O and OH radicals are plotted in Figure 6.64 and Figure 6.65. Since H_2O and OH are products of hydrogen reacting with air, their presence indicates the presence of chemically reacting flows. The largest concentration of water can be found around the perimeter of the fuel plume. The same trend is found in the OH contour. The majority of the reactions are occurring towards the outside perimeter of the plume, not the interior of the plume.

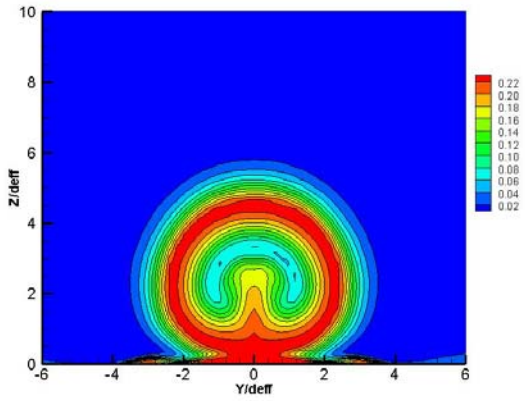

Figure 6.64 Concentration contour of H_2O at 16 diameters

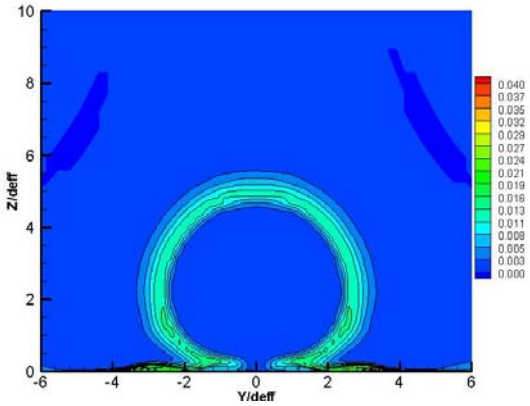

Figure 6.65 Mass fraction contour of OH at 16 diameters

6.6.2 Mass Concentration and Mixing

Predictions show that including the hydrogen–air reactions in numerical modeling of fuel injection slightly reduces the mixing efficiency and decreases the local hydrogen (H atoms in all forms) concentration. More elemental hydrogen is dispersed among more products in the reacting case, therefore there is less molecular H_2 present in the flow-field. The H_2 concentration contours found in Figure 6.66 show that there is a larger region of maximum concentration in the frozen flow prediction at 16 diameters than in the combustion prediction, as expected. The plume shape is very similar between the two analyses at 16 diameters. At 32 diameters, the frozen flow analysis still has a larger region of maximum concentration and it also has a much smaller fuel plume. With the knowledge that the elemental hydrogen is dispersed among more products for the combustion case, the following conclusion can be made: H_2 contours predict similar mixing behavior for the reacting and non-reacting analyses.

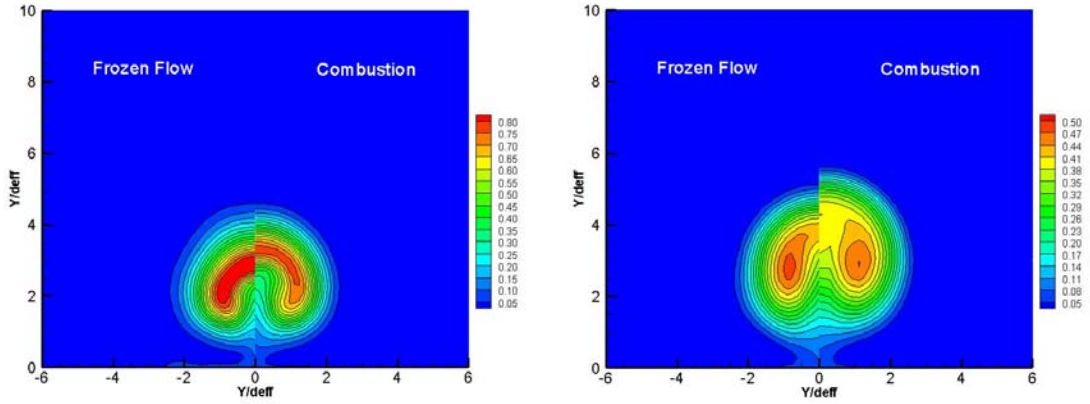

(a) 16 diameters **(b) 32 diameters**

Figure 6.66 H_2 Mass fraction contours at 16 and 32 diameters downstream from injection, y-z plane.

Contours of N_2 are used for a more thorough comparison of the mixing behavior of the two analyses. The combustion model does not include any other forms of nitrogen in the modeled products therefore, N_2 is representative of the amount of the air in the solution and how the air behaves. The mass fraction of nitrogen at planes 16 and 32 diameters downstream of injection can be found in Figure 6.67. The N_2 concentration levels are similar for the two analyses with the combustion analysis predicting slightly higher air concentration in the core at 16 diameters. Adding hydrogen-air reactions to the

numerical equations slightly increases the mixing behavior found in close proximity to the injection point. At 32 diameters, the reacting analysis predicts a larger plume area with similar N_2 concentrations. A larger plume area typically is associated with better mixing because of a larger surface area for molecular diffusion. However, the contour at 32 diameters predicts that the N_2 concentration is similar between the analyses even though the plumes are different sizes.

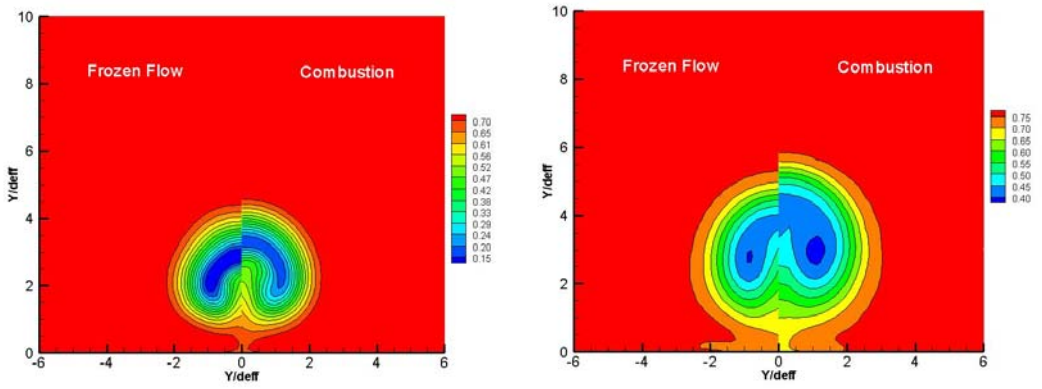

(a) 16 diameters **(b) 32 diameters**

Figure 6.67 N_2 Mass Fraction Contours at 16 and 32 diameters downstream from injection, y-z plane.

Table 6-12 lists integrated parameters for y-z cross-planes at 16 and 32 diameters downstream of injection. The maximum concentration, σ_{max}, of H_2 at each plane is found in the first row of data. At both streamwise locations, the non-reacting simulation predicted a slightly higher concentration of H_2. This is due to dispersion of elemental hydrogen among other products in the reaction. The minimum concentration in the plume for N_2 is found in row 2 of the table. Since the combustion model does not include elemental nitrogen as a product species, the nitrogen concentration provides insight to the mixing behavior of the fuel-air interaction. The minimum concentration of N_2 is very similar for the two cases. The similarities in magnitude indicate similar mixing of the two predictions.

Table 6-12 Integrated quantities at 16 and 32 effective diameters

	$x/d_{eff} = 16$		$x/d_{eff} = 32$	
	Non-Reacting	Reacting	Non-Reacting	Reacting
$\sigma_{max\ (H2)}$	0.857	0.765	0.483	0.471
$\sigma_{min\ (N2)}$	0.098	0.100	0.393	0.347
$y\pm$	4.994	4.977	5.080	5.406
z_{max}	4.770	4.684	5.250	5.74
η_m	0.097	0.083	0.132	0.112

The next two rows define the plume width, y±, and maximum height, z_{max}. The points of maximum height and width are defined as the locations where the hydrogen concentration is equal to the stoichiometric value of hydrogen. The plume width and maximum height are very similar at 16 diameters for the two simulations however, at 32 diameters the reacting simulation has a larger plume area which indicates a faster spreading rate for the reacting simulation. This will lead to better mixing over distance and time. The plume growth is larger in the vertical direction than in the lateral direction.

The remaining integrated parameter is the mixing efficiency parameter, $\eta_{m,,}$ defined earlier. For the reacting simulation, the elemental fuel mass fraction used in the mixing efficiency parameter is estimated by tracking H atoms in the flow. The mass fraction of H_2 and H is used along with mass weight mass fractions of H_2O, HO_2, HO and H_2O_2 to calculate the total mass fraction of H atoms in the evaluated plane. The mass fraction of H atoms is used in Equation [5-2] to calculate a mass weighted mixing efficiency. The mixing efficiency for the reacting case is slightly less than the non-reacting analysis. For a complete scram mode analysis, this is expected however, for dual-mode conditions the opposite trend is often seen[87].

The mixing efficiency takes into account the density and velocity in the plume. Mach contours found below show that the fluid in the core of the plume of the reacting simulation moves slower than the non-reacting simulation. More energy is used in the chemical reaction which slows the reacting flow down. Combine the slower moving core of the reacting analysis with similar fuel mass fraction contours found in Figure 6.66, and the mixing efficiency parameter decreases in the reacting simulation. However, with combustion slowing down the fluid in the plume core, the fuel-air mixture has more time to interact and mix.

6.5.3 Total Pressure

Transverse injection is usually accompanied by total pressure losses. Contours of normalized total pressure can be found in Figure 6.68. The local total pressure is normalized by the freestream total pressure. The frozen flow analysis predicts a lower total pressure loss. Simple 1-D analyses show that large total pressure losses accompany heat release in supersonic flows. With combustion, more energy is produced in the flow and larger changes in temperature and pressure occur. It is not surprising that the addition of combustion produces larger losses in the plume. The total pressure contours are similar in structure and size even though the magnitudes are very different.

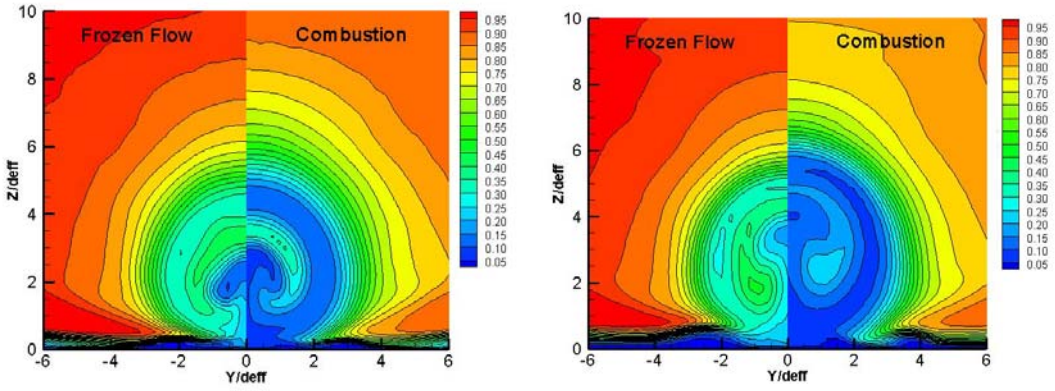

(a) 16 diameters **(b) 32 diameters**

Figure 6.68 Normalized total pressure contours at 16 and 32 diameters downstream from injection, y-z plane

6.5.4 Mach Number

Coupled with the larger total pressure losses found in the plume core of the combustion analysis is a slower moving core seen in the Mach contours found in Figure 6.69. The size and shape of the fuel plume are similar in the Mach contours but the magnitudes are very different. The combustion analysis predicts a core moving approximately at Mach 2.0 where as the non-reacting analysis core is predicted to progress downstream at Mach 3.3. The slower moving fluid corresponds to longer fuel residence times. The longer residence time does come with the trade-off of larger total

pressure losses (as seen with the total pressure contours) to slow the flow down to the local Mach numbers.

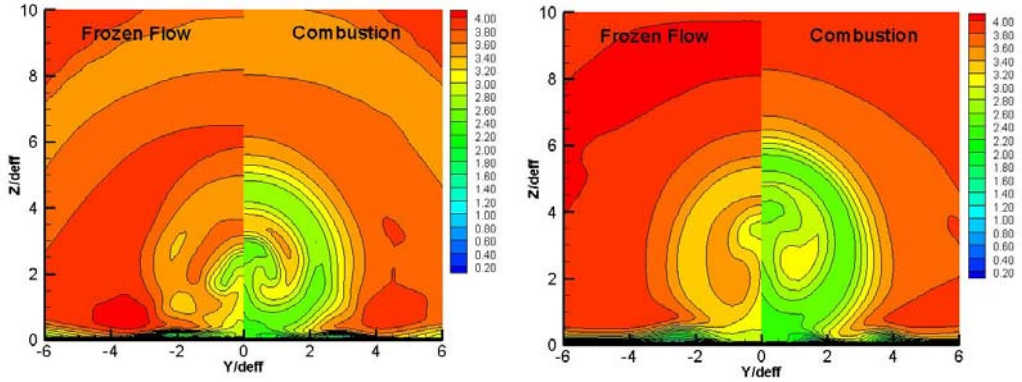

(a) 16 diameters **(b) 32 diameters**

Figure 6.69 Mach number contours at 16 and 32 diameters downstream from injection, y-z plane.

6.5.5 Vorticity

Vorticity contours at 16 and 32 diameters can be found in Figure 6.70. The reacting, combustion analysis produces a larger area of higher vorticity. However, the intensity of the core does not differ largely between the two cases. The larger area found in the combustion prediction indicates a faster spreading rate. There is a steeper gradient from high to low vorticity in the non-reacting prediction than in the reacting prediction. At 32 diameters the reacting simulations shows a larger area of maximum vorticity at the plume center than the non-reacting flow simulation but similar vorticity magnitude in the remainder of the plume. The plume is again larger for the reacting analysis. The addition of chemical kinetics to the numerical solver maintains the same magnitude of vorticity in the plume but creates a larger region of rotation and aids in large-scale mixing or stirring of the flow. At 32 diameters there is a larger region just off-center of low vorticity fluid that is entrained within the higher vorticity region. This interface creates a larger fuel-air shear layer.

The vorticity contours overlaid with momentum streamlines can be found in Figure 6.71. The CVP seen in the prediction with combustion is larger than the frozen flow prediction. The CVP is the primary mechanism for mixing for jets in a crossflow. Adding combustion produces several smaller vortices near the wall surface and on the

perimeter of the fuel plume. These are related to the horseshoe vortex that is created from injection but are stronger in the reacting analysis due to larger changes in pressures. The initial bow shock created from injection can be seen by the arch boundary created by the streamlines in the non-reacting analysis. The reacting prediction has a flat boundary with less restriction of the flow in the vertical direction on the centerline. The streamlines show that more of the flow on the centerline is able to penetrate into the freestream in the reacting prediction.

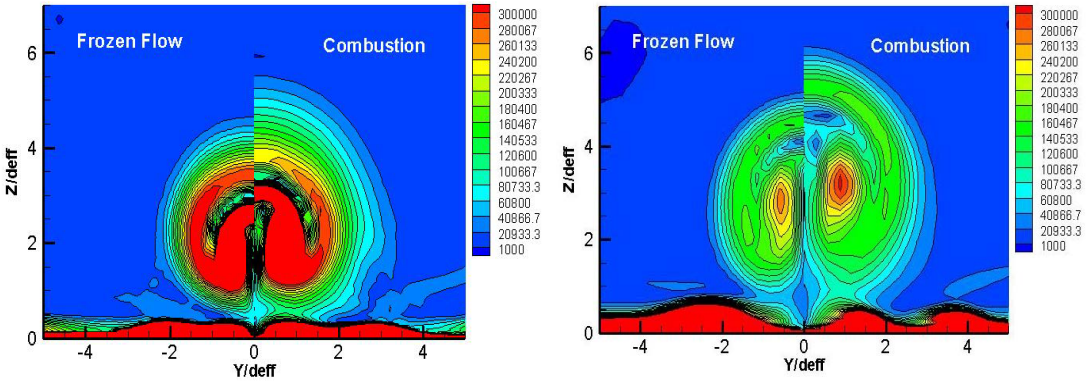

(a) 16 diameters **(b) 32 diameters**

Figure 6.70 Vorticity Contours at 16 and 32 effective diameters downstream from injection, y-z plane.

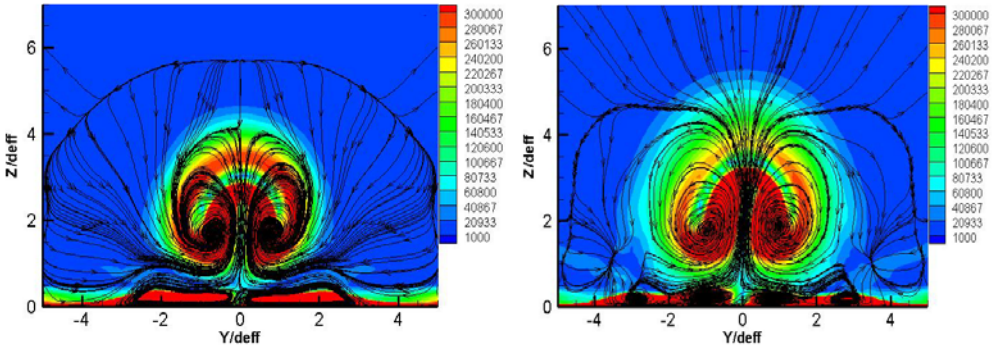

(a)Frozen flow analysis **(b) Combustion analysis**

Figure 6.71 Vorticity contours overlaid with streamlines at 16 diameters.

Chapter 7: Conclusions

Numerical predictions for sonic, light gas, jet injection into a supersonic cross flow were presented. The scope of the numerical analysis encompasses many studies that affect how the flow-field was numerically modeled and the behavior, specifically mixing, of the flow-field itself. The Baseline injector, a single round inclined injector, was used to assess the capabilities of the Reynolds Averaged Navier Stokes equations with a two-equation turbulence model and the sensitivity of the prediction to changes in the numerical model. More complex injector designs were then treated for comparison with the Baseline case. The predictions were compared to available experimental data. The following conclusions about the numerical predictions were made from these analyses:

1. The Menter shear stress transport turbulence model, a steady, two-equation, three-dimensional Reynolds Averaged Navier Stokes model, was able to predict the behavior of jets in a supersonic cross flow. The best results were found for the more complex injector cases.
2. Numerical predictions of mixing which relies on mass diffusion of heated fluids with different densities were sensitive to the choice of turbulent Prandtl number. A decrease in turbulent Prandtl number from 0.9 to 0.7 resulted in predictions with better agreement to the experimental results. The heated helium diffused more rapidly into the freestream with a lower turbulent Prandtl number. Pressures in the plume did not vary.
3. The choice of turbulent Schmidt number also influenced the solution, but to a lesser degree than the turbulent Prandtl number. An increase in turbulent Schmidt number from 0.5 to 0.7 predicted the same initial mixing efficiency at 16 effective diameters, but at 32 effective diameters, a lower mixing efficiency and higher fuel concentration was found. The turbulent Schmidt number influences the small-scale mixing or molecular diffusion in the flow-field. The increase in fuel concentration found farther downstream is a result of an increased Schmidt number and less molecular diffusion.
4. An increase in freestream turbulence intensity decreased the predicted plume penetration and slightly increased the pressure losses. However, the increase did not alter the mixing efficiency and only slightly affected the fuel maximum

concentration. The large boundary layer present in this case (it encompasses the entire jet plume) could be the cause of the insensitivity of the prediction to large increases in freestream turbulence.

5. Changing the CFD software tool from GASP to FLUENT did not significantly alter the predictions. Both tools were able to capture the behavior of the jet plume namely, mixing of the counter rotating vortex pair.

The best Baseline predictions for a Mach 4 cross flow were compared to three different injector designs. The configurations were an aerodynamic ramp of four flush wall injectors in an array, a diamond injector that was aligned with the freestream and the same diamond injector that was yawed 15º to the freestream. Helium mass fraction, Mach number, total temperature and total pressure contours were generated. From these data, penetration of the helium injectant core, total pressure losses and mixing efficiency were calculated. The main conclusions drawn from the injector studies are as follows:

6. Both the CFD and the experiment found that the mixing efficiency value for the aeroramp injector was slightly higher than that of the Baseline injector at these conditions. The aeroramp injector produced a larger amount of lateral mixing than the Baseline injector. This was due to the greater cross-stream distance between the individual injector orifices.
7. The aeroramp injector showed higher local total pressure losses in the plume than the Baseline injector. This is due to the higher angle of injection of the first row of the aeroramp array and the multiple shock structures from the two rows of jets. However, the mass-averaged total pressure loss parameter showed that the aeroramp has very similar overall losses at 16 and 32 effective diameters downstream as the Baseline injector. The CFD predicted the total pressure of the experiment.
8. The diamond injectors, both aligned and yawed, did not predict substantial improvement in vertical penetration over the Baseline injector, which is consistent with the experimental results. This is most likely due to the high momentum flux ratio for these cases.
9. The mixing predicted for the diamond injectors was very similar to the mixing of the Baseline injector. The mixing found in the experiments was under-predicted by the CFD analysis.

10. The diamond injectors had lower total pressure loss parameters than the Baseline injector. The shocks produced by injection through a diamond-shaped orifice were not as strong as the shocks produced by the Baseline, circular orifice. In addition the diamond injector does not have a separation region upstream of the injector.
11. The CFD tools made more accurate predictions of the Baseline and aeroramp injectors than the diamond injectors. The helium concentration was under-predicted by the CFD for the diamond injectors. However, the shape and size of the jet were predicted accurately. The shock strength and structure as well as the separation regions produced by injection changes more from the Baseline-shape to the diamond-shape than they do from the Baseline to the aeroramp. Numerical modeling of a wedge shape is typically hard to predict. The shape of the computational cells and normal direction of gradients across those cell faces make it increasingly difficult for accurate predictions.
12. Time-accurate analyses were performed for the Baseline and aeroramp injectors. The initial oscillations produced in the transient phase of the injection process were damped out and the solution converged onto the steady-state solution. The size of the boundary layer could play a role in the damping of the oscillations.

Computational studies were also performed to investigate the effects of impinging shocks on jet injection of heated helium into a Mach 4 cross flow. Helium mass fraction contours, Mach number, total temperature and total pressure plots were generated. From these data, penetration of the helium injectant core and mixing efficiency were calculated. An investigation of vorticity fields was completed using predictions from the CFD data. The conclusions, unless otherwise stated, were consistent with the conclusions from the experiments. The main conclusions drawn from these studies are as follows:

13. The impingement of a shock upon a light gas jet into a Mach 4 cross flow, near the injection point, enhances mixing.
14. The closer the shock to the injection point, the larger the effect on mixing and vorticity. The original vortex pair is less stable closer to the point of injection, therefore the influence of the shock is greater. In addition, closer to injection, the plume has the largest density gradient and it is also the location where the interior

angle between the density gradient and the pressure gradient is the largest. This leads to the largest change in vorticity due to baroclinic effects.

15. The CFD analysis predicted slightly larger improvements than the experimental results showed for the impinging shock at locations further downstream over the Baseline case.
16. A vorticity jump across the shock was calculated, and the largest change in vorticity occurred with the shock intersecting the jet closest to injection. The vorticity jump across the shock is attributed to the vorticity tangential to the shock. The vorticity normal to the shock does not change.
17. A vortex dynamic analysis showed faster mixing for the cases with shocks. Similarities were found between the contour plots at x/d_{eff}=8 for shock at x/d_{eff} = 2 and the Baseline case (no shock) further downstream at x/d_{eff} =16.
18. CFD analysis was able to provide good simulations of the experimental results for the cases with shock impingement.

A computational comparison study of hydrogen-air reacting flow and non-reacting flow was also conducted. Species mass fraction contours, Mach number, total temperature and total pressure plots were generated. From these data, penetration of the plume core and mixing efficiency were calculated. The main conclusions drawn from these studies are:

19. Modeling combustion of hydrogen with air in a Mach 4 cross flow did not significantly change mixing from the non-reacting analysis. The N_2 concentration levels present in both cases and the mixing efficiencies were very similar. Mixing is not controlled by combustion, but it would be interesting to determine how changes to mixing affect the combustion process.
20. The addition of a reacting model did change the size of the jet plume further downstream from injection. The combustion analysis predicted a larger plume at x/d_{eff} = 32 than the non-reacting analysis. The larger plume size could be attributed to the lower Mach number present in the plume for the reacting analyses, which allowed for more lateral spreading.

21. The reacting analysis predicted a larger counter rotating vortex pair which could also be coupled to the increase in lateral spreading caused by slower moving fluid and a faster spreading rate.

Based upon all these studies some observations can be made. Small discrepancies between analytical predictions and experimental results might possibly be attributed to error within the numerical code and defined boundary conditions. The size of the sampling grid of the experiment could also play a small role in the differences. Possible improvements in the CFD predictions could be found by modeling the injector system farther upstream into the plenum and reservoir to ensure the proper flow profile at the injector inlet and outlet. Other possible studies of the CFD predictions could be the modeling of the actual tunnel walls. The side walls of the tunnel were not modeled, because it was assumed that the injector(s) were displaced far enough from the walls so that the modeled flow would not see the effects of the boundary layer on the side walls.

Possible future studies that could be conducted to better understand and improve mixing would be to combine the best properties of the transverse injectors studied and numerically model an aerodynamic ramp that combines well-designed diamond and round injectors for a Mach 4 cross flow. A lower momentum flux ratio should be used for the diamond injector. Another investigation that would be beneficial is to perform more analyses and experiments with varying mass flow rates and/or pressure through the orifices of various aeroramp injectors. The last recommendation is to conduct a large-eddy simulation (LES) or (DES) analysis to better model the small-scale turbulence and its development. A DES or LES study would require much more computing power and storage than the RANS studies.

Numerical modeling offers a way to study the entire flow more thoroughly and in-depth than experiments. Once the model is calibrated to mimic the experimental data, the CFD prediction can be used to study fine-scale properties at any x, y and z location. The numerical model can also be used to analyze any changes that need to be made to the physical model. Often in industry, the required time and money is not present to perform a plethora of experiments, in this situation numerical modeling is the necessary tool used to arrive at qualitative answers quickly and inexpensively. The procedures and findings documented in theis research can be applied towards future similar analyses. It is

essential that the capabilities of current technologies be tested and understood for future use and further development.

References

[1] Ferri, A., and Fox, H., "Analysis of Fluid Dynamics of Supersonic Combustion Process Controlled by Mixing," 12th International Symposium on Combustion, Combustion Inst., Pittsburg, PA, 1968, pp. 1105-1113.

[2] Ferri, A., "Review of Scramjet Technology," *Journal of Aircraft*, Vol. 5, No. 1, 1968, pp. 3-10.

[3] Andrews, E.H., and Mackley, E.A., "Review of NASA's Hypersonic Research Engine Project," AIAA Paper 93-2323, 1993.

[4] Billig, F.S., "SCRAM: A Supersonic Combustion Ramjet Missile," AIAA Paper 93-2329, June 1993.

[5] Voland, R., and Rock, K., "NASP Concept Demonstration Engine and Subscale Parametric Engine Tests," AIAA Paper 95-6055, April 1995

[6] Fry, R. S., "A century of Ramjet Propulsion Technology Evolution," *Journal of Propulsion and Power*, Vol. 20, No.1, 2004.

[7] Paull, A., Alesi, H. and Anderson, S., "HyShot Flight Program and How it was Developed," AIAA Paper 2002-4939, Oct. 2002.

[8] McClinton, C., "X-43 Scramjet Power Breaks the Hypersonic Barrier: Dryden Lectureship in Research for 2006," AIAA Paper-2006-1, Reno, Nevada, Jan. 9-12, 2006

[9] NASA website http://www.nasa.gov/centers/dryden/news/FactSheets/FS-040-DFRC.html

[10] Anderson, G.Y., "An exampination of injector/combustor design effects on scramjet performance." 1974, Proc. 2nd Int. Symp. Air Breathing Engines, Sheffield England

[11]Kodera, M., Sunami, T, "Numerical study of mixing and combustion process of a scramjet engine model." AIAA-Paper 2001-1868, Kyoto, Japan, Apr. 24-27, 2001

[12] Parent, B., Sislian, J.P., "Turbulent Hypervelocity Fuel/Air Mixing by Cantilevered Ramp Injectors" AIAA Paper 2001-1888, 2001

[13] Roger, R.P., Chan, S.C., "Parameters Affecting Penetration of a Single Jet into a Supersonic Cross flow: A CFD Study –II." AIAA Paper 98-0425, Jan 1998

[14]Riggins, D.W. and Vitt, P.H.,"Vortex Generation and Mixing in Three-Dimensional Supersonic Combustors," *Journal of Propulsion and Power*, Vol. 11, No. 3, 1995, pp. 419-426, May-June

---

[15] Heiser, W.H., Pratt, D.T., Daley, D.H., and Mehta, U.B., "Hypersonic Airbreathing Propulsion," AIAA education series, Przemieniecki, J.S. (Edit.) AIAA, Washington, D.C., 1994.

[16] Hartfield, R.J., Hollo, S.D., and McDaniel, J.C.,"Experimental Investigations of a Supersonic Swept Ramp Injector using Laser Induced Iodine Fluorescence,"*Journal of Propulsion and Power,* Vol.10 No.1,1994, pp. 129-135, January-February.

[17] Sunami, T., Murakami, A., Kudo, K., Kodera, M., "Mixing and Combustion Control Strategies for Efficient Scramjet Operation in Wide Range of Flight Mach Numbers." AIAA Paper 2002-5116, 2002, Orleans, France

[18] Billig, F.S., Orth, R.C., Lasky, M., "A unified analysis of gaseous jet penetration." 1971 *AIAA Journal,* Vol 9, No. 6, pp 1048-58.

[19] Tomioka, S., Murakami, A., Kudo, K., and Mitani, T., "Combustion Tests of a Staged Supersonic Combustor with a Strut," *Journal of Propulsion and Power*, Vol. 17, No. 2, pp. 293-300, March-April 2001.

[20] Schetz, J.A., *Injection and Mixing in a Turbulent Flow*, AIAA, New York, New York, 1980

[21] Fuller, E.J., Mays, R.B., Thomas, R.H., and Schetz, J.A., "Mixing Studies of Helium in Air at Mach 6," AIAA Paper 91-2268, June, 1991.

[22] Barber, M.J., Roe, L.A., and Schetz, J.A., "Simulated Fuel Injection through a Wedge Shaped Orifice in a Supersonic Flow," AIAA Paper 95-2559, July 1995.

[23] Murugappan, S., Gutmark, E., "Control of Transverse Supersonic Jet Injection into a Supersonic Cross-stream." AIAA Paper 2004-1204. 2004

[24] Beresh, S.J., Henfling, J.F., Erven, R.J., Spillers, R.W., "Penetration of a Transverse Supersonic Jet into a Subsonic Compressible Cross flow." *AIAA Journal*, Vol. 43, No. 2, February 2005

[25]Rogers, R.C., "A study of the Mixing of Hydrogen Injected Nomal to a Supersonic Airstream," NASA TN L-7386, Langley Research Center, March 1971.

[26] Schetz, J.A., Billig, F.S., "Studies of Scramjet Flowfields," AIAA Paper 1987-2161 1987.

[27] Curran, E.T., Heiser, W.H., Pratt, D.T., "Fluid Phenomena in Scramjet Combustion Systems." Annual Review of Fluid Mech. 1996. 28:323-60

[28] Hollo, S.D., McDaniel, J.C., Hartfield, R.J., "Characterization of Superonsic Mixing in a Nonreacting Mach 2 Combustor." AIAA Paper 92-0093 1992

[29] Tomioka, S., Jacobsen, L.S., and Schetz, J.A., " Interaction between a Supersonic Airstream and a Sonic Jet Injected throught a Diamond-shaped Orifice," AIAA Paper 2000-0088, January 2000.

[30] Barber, M.J., Roe, L.A. and Schetz, J.A., "Simulated Fuel Injection through a Wedge Shaped Orifice in a Supersonic Flow," AIAA Paper 95-2559, July 1995

[31] Schetz, J.A., Thomas, R.H., and Billig, F.S.,"Miing of Transverse Jets and Wall Jets in Supersonic Flow," IUTAM Symposium on Separated Flows and Jets, Novosibirsk, July 1990.

[32] Fuller R.P., Nejad, A.S., and Schetz, J.A.,"Fuel-Vortex interactions for Enhancing mixing in Supersonic Flow," AIAA Paper 96-2661, July 1996

[33] Jacobsen L.S., Gallimore S.D., Schetz J.A., O'Brien W.F., Goss L.P., "Improved Aerodynamic-Ramp Injector in Supersonic Flow," AIAA Paper 2001-0518, January 2001

[34] Cox, S.K., and Gruber, M.R.," Effects of Spanwise Injector Spacing on Mixing Characteristic of Aerodynamic Ramp Injectors," AIAA Paper 98-3272, July 1998.

[35] Jacobsen L.S., Gallimore S.D., Schetz J.A., O'Brien W.F., Goss L.P., "Improved Aerodynamic-Ramp Injector in Supersonic Flow", *Journal of Propulsion and Power*, Vol. 19, No. 4, July-August 2003

[36] Eklund, D. R., and Gruber, M. R., "Study of a Supersonic Combustor Employing an Aerodynamic Ramp Pilot Injector," AIAA Paper 99-2249, June 1999.

[37] Gruber, M., Donbar, J., Jackson, T., Mathur, T., Eklund, D., and Billig, F., "Performance of an Aerodynamic Ramp Fuel Injector in a Scramjet Combustor," AIAA Paper 2000-3708, July 2000.

[38] Lee, S.H., Jeung, I.S and Yoon, Y., "Computational Investigation of Shock-Enhanced Mixing: Application to Circular Cross Section Combustor," *AIAA Journal*, Vol. 36, No. 11, November 1998.

[39] Gruber, M.R., Nejad, A.S.,Chen, T.H., Dutton,J.C., "Bow Shock/Jet Interaction in Compressible Transverse Injection Flowfields." *AIAA Journal*, Vol 34, No.10, March 1996

[40] Ben-Yakar, A., M. G. Mungal, and R. K. Hanson." Transverse jets in supersonic cross flow, Part 2: The Effect of Compressibility, Velocity Ratio and Density Ratio". *Physics of fluids*, 2005.

---

[41] Krothapalli, Lourenco & Buchlin 1990 Separated flow upstream of a jet in a cross flow *AIAA Journal*, Vol. 28 pp. 414-420

[42] Tam, Chung-Jen, Baurle, R.A., "Numerical Study of Jet Injection into a Supersonic Cross Flow" AIAA Paper 1999-225, 1999

[43] Martens, S., McLaughlin, "Mixing Enhancement Using Mach Wave Interaction in a Confined Supersonic Shear Layer." AIAA-95-2177, June 1995

[44] Green, S.I., *Fluid Vorticies*. 1995 Kluwer Academic Publishers. Netherlands

[45] Agui J.H., "Shock Wave Interactions with Turbulence and Vorties" PhD thesis. City Univ of New York 1998

[46] Lee, S., Lele, S.K., Moin, P., "Interaction of Isotropic Turbulence with a Strong Shock Wave," AIAA 94-0311, January 1994.

[47] Andreopolulos, Y., Agui, J.H., Briassulis, G., "Shock Wave-Turbulence Interactions." *Annual Rev. Fluid Mech*. 2000. 32:309-345

[48] Lele, S.K., "Compressibility effects on Turbulence." 1994,*Annual Review of Fluid Mechanics.* 26:211-54

[49] Briassulis GK, Andreopoulos J. 1996 "High resolution measurements of isotropic turbulence interacting with shock waves." AIAA Paper 96-0042., 1996

[50] Lee L, Lele SK, Moin P. 1993 "Direct Numerical simulation of isotropic turbulence interacting with weak shock wave." *Journal of Fluid Mechanics,* Vol. 251, pp. 533-62.

[51] Hannappel R, Friedrich, R. 1995 "DNS of a Mach 2 Shock interacting with isotropic turbulence." *Applied Science Res,* Vol.54, pp. 205-21.

[52] Jacquid L. Geffroy, P., 1997 "Amplification and Reduction of Turbulence in a Heated Jet/Shock Interaction." Journal L12-17. Free Shear flow Conf.

[53] Hermanson, Cetegen .B.M., "Mixing Enhancement of Non-Uniform Density Turbulent Jets Interacting with Normal Shock Waves," Presented at Symp. Combust., Combustion Institute 27th, Univ Colo. Boulder.

[54] Hermening K., "Experimental Investigation of Shock Wave Interaction with Jets," Tech Univ Berlin, Berlin Germany

[55] Hunt, J.L., and Eiswirth E.A., "NASA's Dual-Fuel Airbreathing Hypersonic Vehicle Study," AIAA Paper 96-4591, November 18-22, 1996.

[56] Huh, H., Driscoll, J.F., "Measured effects of Shock Waves on Supersonic Hydrogen-air Flames," AIAA-96-3035, 1996.

[57] Barakos, G., Drikakis, D., "Investigation of Nonlinear Eddy-Viscosity Turbulence Models in Shock/Boundary –Layer Interaction." *AIAA Journal*, Vol. 38, No.3, March 2000.

[58] Obata, S. and Hermanson, J.C., "Numerical Simulation of Shock-Enhanced Mixing in Non-uniform Density Turbulent Jets," *AIAA Journal*, Vol. 38, No. 11, November 2000.

[59] Maddelena, L., Campioli, T. and Schetz, J.A**. "**Experimental and Computational Investigation of an Aeroramp Injector in a Mach Four Cross Flow**"** AIAA 2005-Hypersonics Conference, Capua, Italy, 2005.

[60] *GASP Version 4 Technical Reference*, AeroSoft Inc. Blacksburg, VA

[61] *Fluent reference User's Guide* Fluent Inc. 1998

[62] Nix, A.C., Smith, A.C., Diller, T.E., Ng, W.F., Thole, K.A., "High Intensity Large Length-Scale Freestream Turbulence Generation in a Transonic Cascade Tunnel." ASME 2001.

[63] Pope, Stephen B., *Turbulent Flows*, Cambridge University Press, 2000

[64] Wilcox, David C., *Turbulence Modeling for CFD 2 ed.* DCW Industries Incorp, 1999

[65] Smagorinsky, J. "General Circulation Experiments with Primitive Equations: I. The basic Equations," *Mon. Weather Review*. Vol. 91, pp. 99-164, 1963

[66] Spalart, P.R., Jou, W.H., Strelets, M. and Allmaras, S.R., "Comments on the Feasibility of LES for Wings, and on a Hybrid RANS/LES Approach," First AFOSR International Conference on DNS/LES, LA 1997.

[67] Forsythe, J.R., Hoffmann, K.A., Squires, K.D., "Detached-Eddy Simulation with Compressibility Corrections Applied to a Supersonic Axisymmetric Base Flow," AIAA 02-0586, January 14-17 2002.

[68] Constantinesu, G.S., Squires, K.D., "LES and DES Investigations of Turbulent Flow over a Sphere," AIAA 2000-0540, Jan 10-13 2000.

[69] Morton, S., "High Reynolds Number DES Simulations of Vortex Breakdown Over a 70 Degree Delta Wing," AIAA 2003-4217, 2003.

[70] Forsythe, J.R., Hoffmann, K.A., Squires, K.D, "Detached-Eddy Simulation of Fighter Aircraft at High Alpha," AIAA 2002-0591, January 14-18 2002.

[71] Squires, K.D., " Detached-Eddy Simulation: Current Status and Perspectives," Proceedings of Direct and Large-Eddy Simulation-5, 2004.

[72] Menter, F.R., "Two-Equation Eddy-Viscosity Turbulence Models for Engineering Applications." *AIAA Journal*, 32, 1994, pp.1598-1605

[73] Drummond, J.P., Rogers, R.C., Hussaini, M.Y., "A Detailed Numerical Model of a Supersonic Reacting Mixing Layer." AIAA-86-1427. June 16-18, 1986.

[74] Drummond, J.P, Mukunda, H.S., "A Numerical Study of Mixing Enhancement in Supersonic Reacting Flow-Fields," AIAA-88-3260, July 11-13, 1986.

[75] Williams, F.A. *Combustion Theory.* Addison-Wesley Publishing Company, Inc., Reading, Mass., 1965, pp. 358-429.

[76] Berman, H.A., Anderson, J.D. and Drummond, J.P., "Supersonic Flow Over a Rearward Facing Step with Transverse Nonreacting Hydrogen Injection," *AIAA Journal*, Vol 21, No. 12, December 1983, pp. 1707-1713

[77] *Gridgen Version 13.3 User Manual*, Pointwise, Inc., PO Box 210698, Bedford, TX 76095. 1999

[78] Tomioka, S., Jacobsen, L.S., and Schetz, J.A., "Sonic Injection from Diamond-Shaped Orifices into a Supersonic Cross flow," *Journal of Propulsion and Power*, Vol. 19, No. 1, 2003, pp. 104-114, January-February.

[79] Peter Grossman's Masters Thesis **"**Experimental Investigation of a Flush-Walled, Diamond-Shaped Fuel Injector for High Mach Number Scramjets" Virginia Polytechnic and State University, December 2006

[80] Holden, M., "Studies of Scramjet Performance in the LENS facility." AIAA 2000-3604, July 17-19, 2000.

[81] Maddelena, L., Campioli, T.L. and Schetz, J.A., "Experimental and Computational Investigation of Light-Gas Injectors in a Mach 4.0 Cross flow," *Journal of Propulsion and Power*. 2006 Vol. 22, No. 5, pp.1027-1038.

[82] Campioli, T.L., Maddelena, L and Schetz, J.A. "Studies of Shock Wave/Transverse Injection Interaction on Supersonic Mixing Processes" AIAA Paper 2006-8135 Canberra, Australia, 2007

[83]W. F. Ng, F. T. Kwok and T.A. Ninnemann, "A Concentration Probe for the Study of Mixing in Supersonic Shear Flows," AIAA Paper 89-2459, July 1989.

[84] Mao, M. Riggins, D. W., and Mc Clinton C.R., "Numerical Simulation of Transverse Fuel Injection, " NASP CR 1089, May 1990.

[85] Steven E. Doerner and Andrew D. Cutler, "Effects of Jet Swirl on Mixing of a Light Gas Jet in a Supersonic Airstream" *Journal of Propulsion and Power* 2001, Vol. 17, No. 6, pp.1327-1332.

[86] Schetz, J.A., *Boundary Layer Analysis*. 1993, Prentince-Hall, Inc. Upper Saddle River, NJ

[87] Baurle, R., "Modeling of High Speed Reacting Flows: Established Practices and Future Challenges," AIAA 2004-267, 42th AIAA Aerospace Sciences Meeting 5-8 January 2004, Reno, NV

[88] B en-Yakar, A., Kamel, M, Morris, C., Hanson, R., "Experimental Investigation of H2 Transverse Jet Combustion in Hypervelocity Flows," AIAA-1997-3019 AIAA/ASME/SAE/ASEE Joint Propulsion Conference and Exhibit, 33rd, Seattle, WA, July 6-9, 1997

[89] Giacomazzi, E., Del Rossi, A., Bruno, C., "Numerical Simulation of a Scramjet Combustion Chamber," IAC-03-S.5.05, 54th IAC of the IAF, 29 Sept – 3 Oct, 2003, Bremen, Germany

[90] Ranuzzi, G., Grasso, F., Bruno, C., "Hydrogen Gas Injection in a Turbulent Supersonic Air fFlow," AIAA 2002-3881 July 2002.

[91] Mack, A., Steelant, J., "Mixing and Combustion Enhancement in a Generic Scramjet Combustion Chamber," AIAA Paper 2006-8134, 2006.

[92] Belanger, J., Hornung, H., "Transverse Jet Mixing and Combustion Experiments in Hypervelocity Flows," *Journal of Propulsion and Power,* Vol. 12., No. 1, Jan-Feb 1996

[93] Baurle, R., "Modeling of High Speed Reacting Flows: Established Practices and Future Challenges," AIAA Paper 2004-267, 2004.

[94] Eklund, D., Baurle, R., "Numerical Study of a Scramjet Combustor Fueled by an Aerodynamic Ramp Injector in Dual-Mode Combustion," AIAA Paper 2001-0379, January 2001.

[95] Muppidi, S., Mahesh, K., "Passive Scalar Mixing in Jets in Crossflow," AIAA 2006-1098, January 2006.

Vita

Theresa Lynn Campioli was born January 16, 1981 in Fairfax, VA, daughter of Carl M. Campioli and Carolyn L. Campioli. She has two sisters, Jennifer Cannan (30) married to Jason Cannan and Mary Campioli (24). Theresa attended Bishop Denis J. O'Connell High School in Arlington, VA, graduating in 1999. Theresa went on to attend Auburn University and received a Bachelors of Science degree in Aerospace Engineering in May 2003. During her time at Auburn she was a member of the NCAA division I soccer team. During her senior year, the soccer team won the SEC conference title. In fall of 2003, Theresa began her graduate education at Virginia Polytechnic Institute and State University working for Dr. Joseph Schetz. She received a Masters of Science in Aerospace Engineering in May 2005. Upon the completion of this dissertation in June 2007, Theresa will receive a Doctor of Philosophy degree in Aerospace Engineering. Since July of 2005 she has also been employed full-time for Aerojet Corporation. Theresa is marrying Daniel Shafer on September 8, 2007.